Control of Crystallinity in Photocatalytic Titanium Dioxide

This thesis is submitted in partial fulfilment of the requirements for the
Degree of Doctor of Philosophy (Chemistry)

Andrew Breeson

UCL

2017

I, Andrew Breeson, confirm that the work presented in this thesis is my own. Where information has been derived from other sources, I confirm that this has been indicated in the thesis

Abstract

Powders and thin films of titanium dioxide (TiO_2) were synthesised via wet chemical methods in two ways: a sol-gel synthesis, and a liquid phase deposition. Crystalline mixed phase powders, highly oriented films, and non-crystalline films of titanium dioxide have all been investigated. Specifically this investigation revealed dramatic differences in the XPS valance band spectra of the crystalline polymorphs of anatase and rutile, and subsequently a novel procedure for extracting quantitative phase information from X-ray photoelectron spectroscopy valence band spectra was developed. A linear relationship between the mixed phase TiO_2 surface structure determined by this novel technique, and the ensuing photocatalytic activities were discovered. Additionally, highly oriented thin films of TiO_2 were synthesised on single crystal substrates. Nitrogen doping of the films was achieved in two ways, and the distribution of the dopant within the films was revealed to be dramatically different for each method. Furthermore, N doping induced a phase transformation from highly aligned rutile to polycrystalline anatase. This result of a rutile to anatase transition at high temperature and not been observed previously. As before, these results were confirmed by X-ray diffraction and X-ray photoelectron spectroscopy valance band analysis. Lastly, non-crystalline, unaligned films of TiO_2 on glass substrates were synthesised. The film structure was revealed to be porous, and successively exhibited superhydrophilic abilities without ultraviolet light irradiation. Further investigation via X-ray absorption spectroscopy techniques revealed the films to have anatase-like short range order with a significant tetrahedral titania component. The films were also shown to be highly photocatalytically active.

Acknowledgements

I would like to thank my supervisor, Dr Robert Palgrave, for his support and advice throughout this project. His guidance was instrumental in the completion of this thesis. I am also grateful to my secondary supervisors Professor Gopinathan Sankar and Dr Gregory Goh for their insights.

I would also like to thank my fellow members of the Palgrave group, and my many colleagues in Singapore. You have all been invaluable to the development of my project.

Additionally, my thanks go to Sanu, my parents, siblings, family, and friends for all of their encouragement.

Table of Contents

List of Abbreviations

a-TiO_2	Anatase titanium dioxide
AHFT	Ammonium hexafluorotitanate
am-TiO_2	Amorphous titanium dioxide
ART	Anatase to rutile transition
BET	Brunauer–Emmett–Teller
CPS	Counts per second
DFT	Density functional theory
DOS	Density of states
FWHM	Full width half maximum
LAO	Lanthanum aluminate ($LaAlO_3$)
LCF	Linear combination fit
LRO	Long-range order
r-TiO_2	Rutile titanium dioxide
RIR	Reference intensity ratio
SEM	Scanning electron microscopy
SRO	Short-range order
STO	Strontium titanate ($SrTiO_3$)
TEM	Transmission electron microscopy
TMEDA	Tetramethylethylenediamine
UPS	Ultraviolet photoelectron spectroscopy
UV	Ultraviolet
VB	Valence band
VBM	Valence band maximum
XRD	X-Ray diffraction
XPS	X-Ray photoelectron spectroscopy

List of Figures

Chapter 1: Introduction

Chapter 2: Experimental Section

Chapter 3: Anatase and Rutile Quantification

Chapter 4: Rutile to Anatase Transformation

Chapter 5: Non-Crystalline TiO_2

List of Tables

Chapter 1: Introduction

Chapter 3: Anatase and Rutile Quantification

Chapter 1: Introduction

1.1 Background

Semiconductor photocatalysts have been of major interest for the materials science community for several decades. Titanium dioxide became the prototypical photocatalytic material shortly after Fujishima and Honda displayed photo-induced decomposition of water into hydrogen and oxygen by TiO_2 electrodes.[1] The paper was published in 1972 when oil prices were at an all-time high, so with its water splitting abilities and low cost, TiO_2 seemed like an ideal candidate to produce cheap, alternative energy. Figure 1.1 shows that the interest in the photocatalytic abilities of TiO_2 continues to grow year on year.

World production of TiO_2 in 2016 exceeded 9 million metric tons,[2] which somewhat illustrates its industrial importance. Most of the TiO_2 produced goes towards non-catalytic applications which can range from white pigments in paints to corrosion resistant coatings.[3] Titanium dioxide is a safe replacement for the lead based paints that were common years ago. It is also used as an additive in food colouring and cosmetics.[4]

The photodegradative properties of TiO_2 have been known ever since it was noticed that exposure to sunlight caused the flaking of paints and the breakdown of fabrics that contained TiO_2.[5] But it was in the 1970s that the photoelectrochemical aspects of TiO_2 started to be explored in-depth. The Fujishima and Honda paper showed that when the surface of a TiO_2 electrode was irradiated with wavelengths of light shorter than its band gap a photocurrent flowed from a (platinum) counter electrode to the TiO_2

electrode through an external circuit.[1] The direction which the current flowed showed that the oxidation reaction was occurring at the TiO_2 electrode and the reduction reaction was at the platinum. Thus, water was split into its constituent hydrogen and oxygen using UV light and without the use of an external power source.

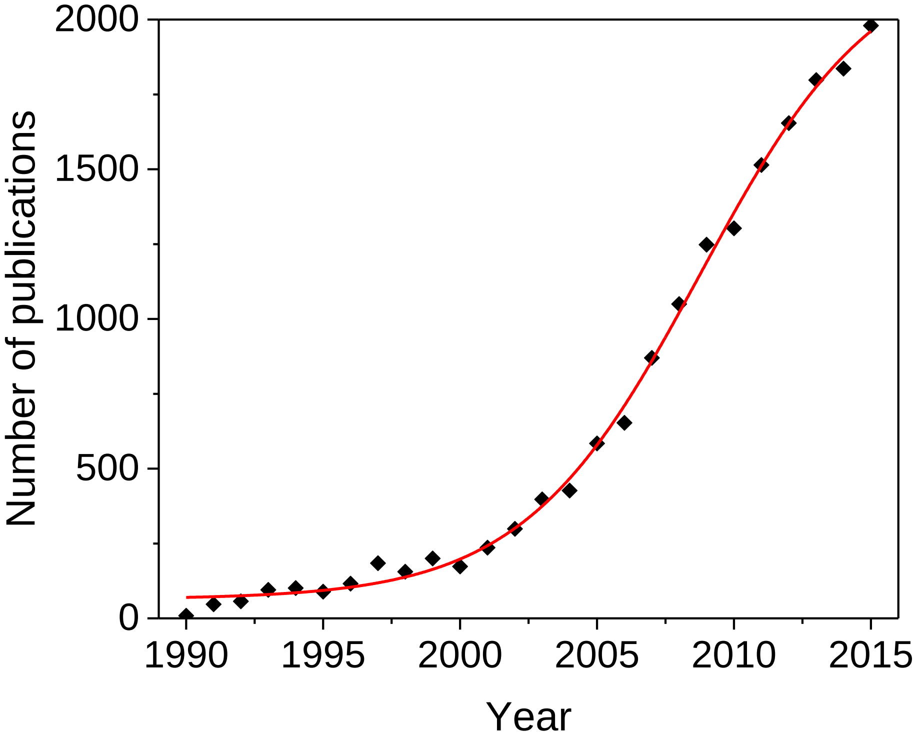

Figure 1.1. Taken from Web of Science, the number of research papers published with the keywords “Titanium Dioxide Photocat*”

If semiconductor electrodes are used for the electrolysis of water, the band gap needs to be at least 1.23 eV (which is equivalent to the equilibrium cell potential for water electrolysis at room temperature and pressure).[6] There have been many investigations into semiconductors with smaller band gaps for visible light photoelectrolysis but few have succeeded due to photodegradation of the semiconductor.

In 1980, Kawai and Sakarta began investigating powdered photocatalysts on their own, rather than photoelectrochemistry with an external circuit. Photocatalytic water-splitting was studied with anatase TiO_2 powders in a suspension and Pt-TiO_2 as a cathodic catalyst.[7] The experiments were semi-successful in that H_2 and O_2 were simultaneously produced; however the overall efficiency of the production was too low to be scaled up industrially.

Despite its reaction efficiency being very high, TiO_2 can only absorb the UV light in the solar spectrum. This equates to about 3% of the total amount of sunlight. Making the prospect of hydrogen production via solar photocatalysis less attractive, and by the mid-1980s research into this field had waned.

Instead, the research focussed on utilising the photo-oxidative power of TiO_2 for pollutant removal. Frank and Bard showed the first case of photocatalytic oxidation using TiO_2 with the decomposition of CN^- and SO_3^{2-} in 1977.[8] So towards the end of the 1980s, harmful compounds in both water and air were shown to be detoxified by using powdered TiO_2 and it was now thought of as being a potential waste water and polluted air purifier.[9] This meant that TiO_2 no longer needed to be doped with platinum and could be used under ambient conditions because the reduction reaction was not hydrogen production any more.

In the 1990s it became more apparent that TiO_2 could not treat large volumes of polluted water or air because ambient light density is too low and TiO_2 utilises only the small UV contribution of sunlight. Using this understanding, applications of TiO_2 that required its use in large three dimensional spaces became less popular. Instead, research shifted towards two-dimensional coating applications of TiO_2. The fact that these coatings are adhered to a substrate means that unlike powders, they don’t need costly and time-consuming recovery procedures, and can be reused repeatedly.

Self-cleaning TiO_2 surfaces first started to be reported in the mid-1990s[10] with one of the first commercial applications being a self-cleaning glass cover for lights in tunnels. The sodium lamps used in tunnels gather a build-up of exhaust fumes and grime which limits their productivity. Providentially, sodium lamps also emit UV light (about 3 mW/cm^2) and this is effective in activating a TiO_2 coating on the glass which in turn leads to the degradation of any dirt.[11] This application of TiO_2 as a self-cleaning coating became widely used in windows.

Soon after, TiO_2 coatings were shown to be antimicrobial and antibacterial. For example E. coli has been shown to be completely eradicated on TiO_2 under outdoor UV light intensity.[12] The problem is that under indoor UV light conditions, the intensity is too weak and takes too long a time, making it less commercially viable as a coating.

Also discovered in the 1990s, was the photo-induced superhydrophilicity that can occur with thin films of TiO_2. Depending on the surface conditions, water is at rest on a TiO_2 thin film with a contact angle in the range of several tens of degrees. But when exposed to UV light, the water spreads out, decreasing the contact angle until it reaches approximately 0°.[13,14] The surface can usually maintain this superhydrophilicity for one or two days, until it returns to its original contact angle. But this effect can be restored again with the irradiation of UV light. This superhydrophilicity aids with the self-cleaning properties of TiO_2 thin films, as water spreads into sheets and doesn't smear.

In general, present day research of TiO_2 is looking to lower its band gap into the visible region of light by various methods, as the limiting factor with the photocatalytic applications is that the absorption edge is in the near UV range at approximately 380 nm.[15] Much research has been undertaken in an attempt to shift this absorption edge into the visible region of the electromagnetic spectrum in order to use more efficiently the available light. If visible light photocatalysis could be achieved with TiO_2 the subsequent beneficial applications would be numerous. As an example, self-cleaning surfaces could function inside using indoor lighting and could therefore dramatically improve the sanitation of healthcare environments.[16] Thin films of TiO_2 have proven themselves capable of many photocatalytic oxidations of potentially harmful organisms such as bacteria[17] and viruses,[18] but as yet, a visible light analogue of this has yet to be developed.

1.2 Properties

1.2.1 Band Structure

It is important to understand the electronic band structure of a solid because it can determine the inherent properties of the material. In particular, the band structure is closely linked to the electronic conductivity, catalytic activity, magnetic properties, structural distortions, and optical properties.

Quantum theory states that individual atoms have discrete energy levels that electrons are permitted to occupy. However, when a large group of atoms are bound together, such as in a solid, the sheer number of electrons that are present result in an essentially continuous band of energy levels. Figure 1.2 represents the how a band is constructed from molecular orbitals.

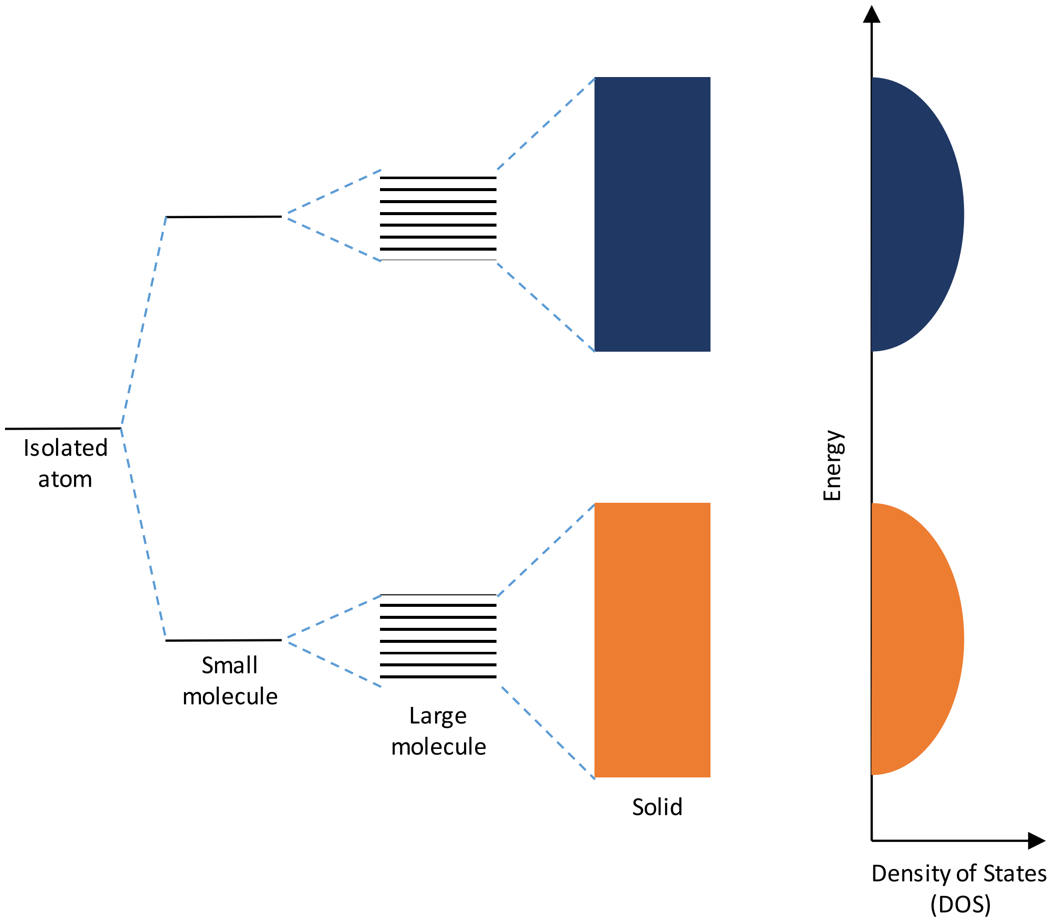

Figure 1.2. The construction of bands from molecular orbitals and a representation of the density of states.

The density of states (DOS) describes the number of states per interval of energy, at each energy level, available to be occupied. It is represented mathematically by a density distribution. A high DOS at a specific energy is indicative of a large number of available states that could be occupied.

A DOS of zero indicates the no states are available to be occupied at that particular energy level.

The bands that are the most important to be concerned with are known as the valence band and conduction band which can be described as analogous to the HOMO and LUMO levels in a molecule.

For any conductivity to occur, the electrons in the valence band need to be able to move into a space. Any material that has the ability to conduct electricity must therefore have electrons in its conduction band (or have holes in its valence band). In order to demonstrate the construction of a band in more detail is it worthwhile to consider a hypothetical linear chain of lithium atoms, figure 1.3 shows this.

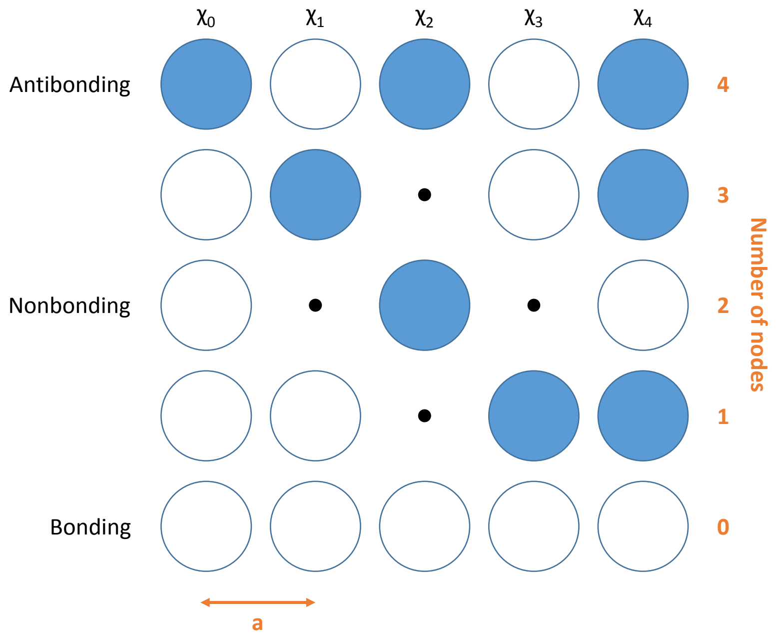

Figure 1.3. The possible phase outcomes of a hypothetical linear chain of five lithium atoms. χ_n represents the atomic orbitals, and a is the lattice spacing between the atoms. The number of nodes can be seen indicated on the right hand side.

Determining the molecular orbital states by the linear combination of atomic orbitals gives more than one solution to the Schrödinger equation. So-called antibonding states can occur in covalent molecules which are in higher energy states than their bonding counterparts and are therefore unoccupied. Considering the hypothetical linear chain of five lithium atoms, each of their valence electron clouds is spherical and hence the central lithium cannot give preference to any of its neighbours.

If the linear chain were to be increased, the number of electronic states into which the 2s state splits would increase, and would be equal to the number of atoms present in the chain. Figure 1.3 represents a chain of 5 lithium atoms but the concept can be extended further. If there are N number of atoms in the chain, there will be N energy levels and N electronic states. If this is the case, the wavefunction for each electronic state can be describe with the equation:

$$\psi_k = \sum e^{ikna} \chi_n \tag{1.1}$$

Where **a** is the lattice constant, **n** identifies the individual atoms with the chain, χ_n represents the atomic orbitals, and **k** is a quantum number that identifies the wavefunction and give information about the phase of the orbitals

For the bonding possibility, **k=0** because the phase does not change when translating through the chain. For the nonbonding possibility, **k=π/2a**, and for the antibonding molecular orbital, **k=π/a**, because the phase reverses when translating by a lattice spacing, **a**.

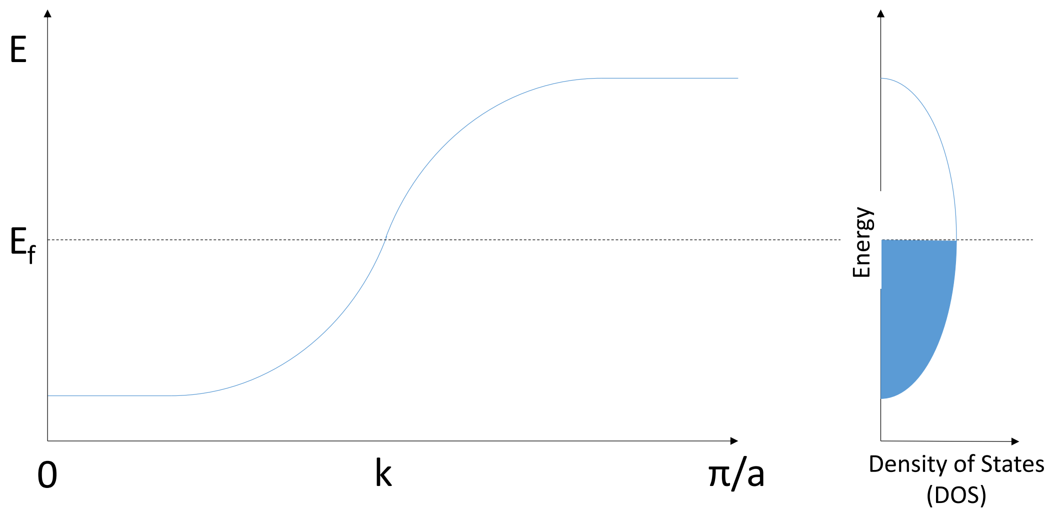

Figure 1.4. The population of the DOS constructed from a plot of energy versus k. The Fermi level can be seen to cut through the centre of the DOS.

Figure 1.4 shows the construction of a hypothetical E-k plot and the subsequent DOS. The DOS is proportional to the inverse of the slope of E(k). The flatter the band structure (i.e. at **k=0** and **k=0.5**), the greater the number of energy levels (DOS) present at that particular energy. As can be seen, the Fermi level cuts through the band to produce a partially filled band. This is indicative of a metal and so in the hypothetical model of a linear chain of lithium atoms, they are expected to be metallic. In reality, solids are not one-dimensional, and so the three-dimensional wavefunction symmetry of TiO_2 is much more complex but obeys the same basic rules.

In metals, this band has only half of the states filled because each state can only accommodate two electrons of opposite spin due to the Pauli exclusion principle. In accordance with the Aufbau principle, the lowest energy states within the band will be filled first, and the upper energy states remain empty. However these upper states can be readily filled with thermally excited electrons or with the application of an electric field. This half-filled band constitutes a conduction band.

In the case of insulators and semiconductors, the difference in their band structure is arbitrary (the one variable being the width of the band gap). In general, insulators are materials with very high resistivity which will not conduct electricity since their valence band is filled, and the energy that would be required to promote an electron to the empty conduction band is impractically high.

Semiconductors occur due to the statistical nature of the thermal energy distribution in the solid matrix; a significant number of electrons will be in the valence band at room temperature because they acquired enough energy to cross the band gap. Therefore, contrary to metallic systems, the conductivity will increase with temperature because more electrons will be promoted up to the conduction band. This will continue until the thermally increased lattice vibration will increase the electron scattering effects and decrease their mobility.

The relationship between E_f and the energy bands gives information about the conductivity properties of the solid. Electrical conduction cannot arise from an empty band, or a band which has completely filled quantum states. Only a partially filled band will be able to conduct.

In the case of an insulator E_f lies within the band gap, and the band gap can be described as ‘large’. In a semiconductor, E_f still lies within the gap, however the gap is narrow enough that the band above the gap has a significant concentration of thermally excited electrons (with a corresponding concentration of positive holes in the band below the gap).

These upper and lower bands are referred to as the conduction band and valence band respectively. The charge concentrations can also be easily modified with the addition of dopants.

The high conductivity of metals can be account for by the partially filled band that does not rely on thermal excitation as with semiconductors and the E_f lies within the band.

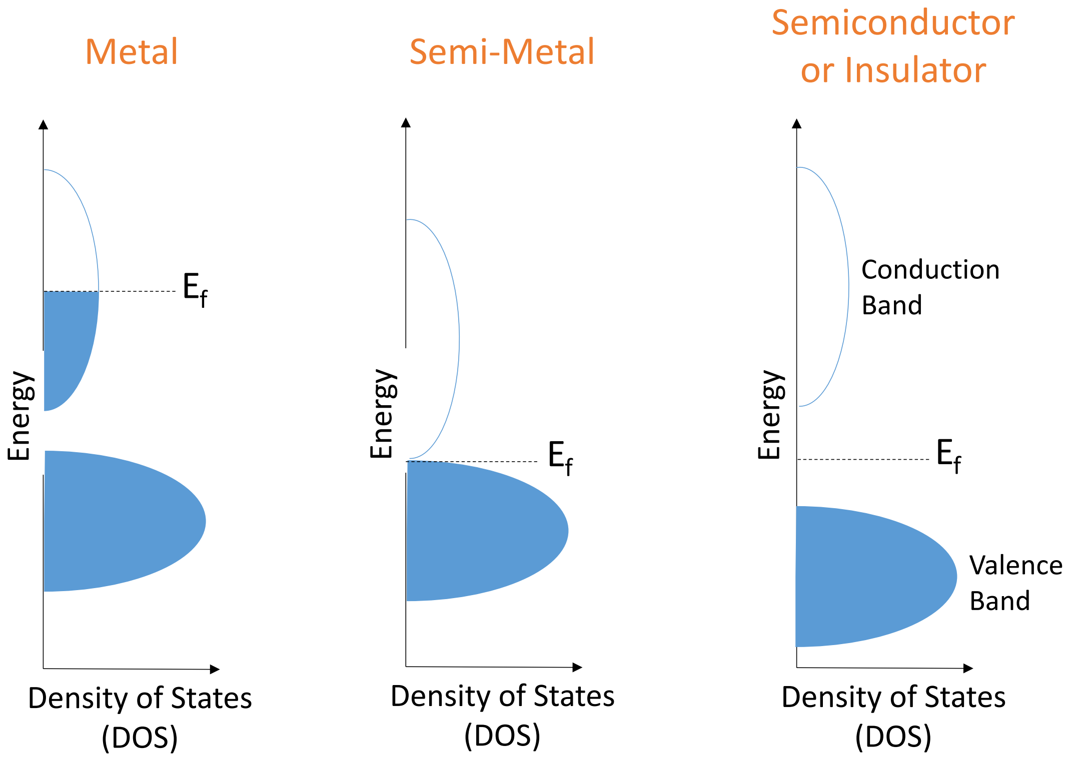

Figure 1.5. A comparison of the density of states in a typical metal, semi-metal, and semiconductor/insulator. E_f represents the Fermi level in each case.

Electrons and holes are classified as fermions, which means that they must obey the Pauli exclusion principle. The Pauli exclusion principle states that no two fermions can occupy the same quantum state. The Fermi-Dirac distribution is the statistical distribution of the fermion energies as a function of temperature. The Fermi-Dirac function gives the fraction of allowed states, **f(E)**, at an energy level **E**, that are populated at a given temperature:

$$f(E) = \frac{1}{1 + e^{(E-E_f)/kT}} \tag{1.2}$$

Where the Fermi Energy, **E_f**, is defined as the energy where **f(E) = ½**. In other words, that half of the available states are occupied. **T** is the temperature and **k** is the Boltzman constant.

This Fermi-Dirac function shows that if a pure semiconductor were to have a band more than several tenths of an electronvolt, it would have a very small concentration of charge carriers. Therefore, conventionally, impurities known as dopants are added to the pure semiconductor to introduce carriers.

1.2.2 Photocatalysis

A catalyst can be described as a substance that accelerates a chemical reaction without being consumed as a reactant, and can be said to lower the free activation enthalpy of the reaction. A photochemical process is any reaction affected by light. Photocatalysis can therefore be described as the acceleration of a photoreaction in the presence of catalyst. This definition encompasses photosensitisation, which is a particular kind of photochemical reaction that occurs when a material known as a photosensitiser absorbs light radiation. When light of the correct wavelength illuminates the sensitiser, an electron from the valance band is promoted to the conduction band. This leaves an electron deficiency or a positive hole, h^+, in the valance band and conversely an excess of negative charge in the conduction band, e^-.

The energy that is required to promote an electron from the valence band to the conduction band depends on the band gap of the material. The band gap is defined as the difference in energy between the highest allowed energy level for electrons in the valence band and the lowest permitted energy level in the conduction band.

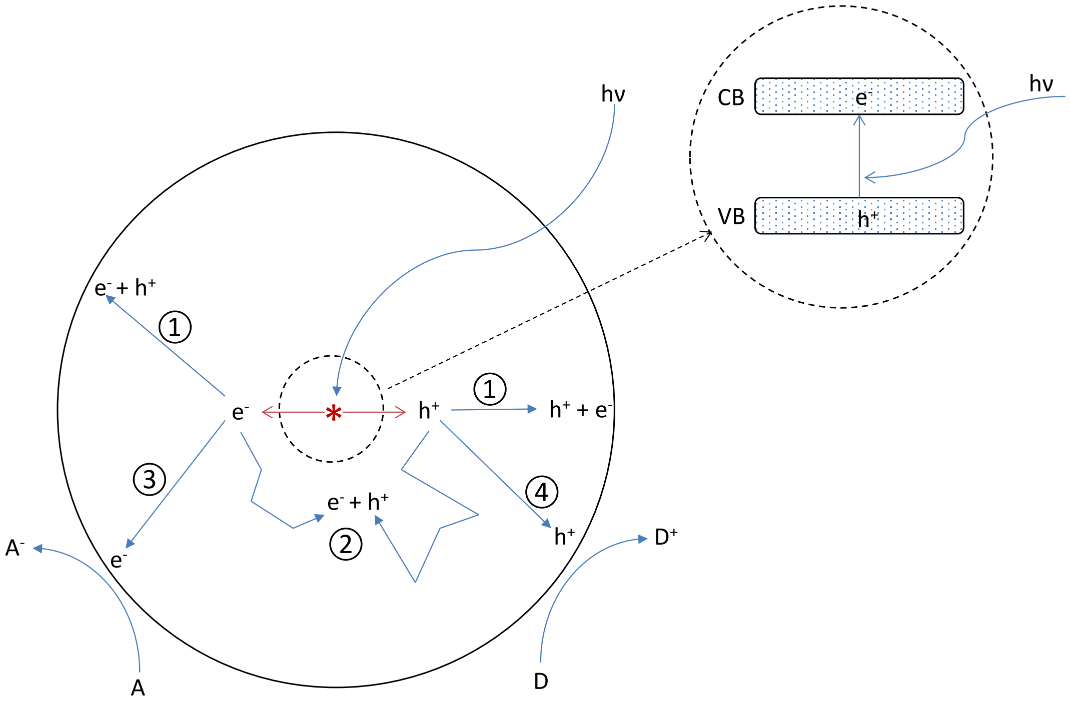

Figure 1.6. The process of electronic excitation in a semiconductor particle. The electron and positive hole can recombine at the surface (1) or in the bulk of the semiconductor (2). Electrons at the surface can reduce electron acceptors A (3) and positive holes can oxidise electron donors D (4). This diagram was adapted from Linsebigler *et al.*[19]

Figure 1.6 shows the photocatalytic reactions proceed via the presence of adsorbed radicals on the titania surface. In turn, these radicals are formed by the absorption of radiation that exceeds the band gap of TiO_2, which generates a species known as an exciton (or an electron-hole pair). These electrons and holes then diffuse through the crystal bulk to the surface and react with the adsorbed molecules, generating radicals.

$$TiO_2 + hv(> 3.2eV) \leftrightarrow \; h^+ + \; e^- \tag{1.3}$$

$$h^+ + H_2O \leftrightarrow \; H^+ + \cdot OH \tag{1.4}$$

$$e^- + O_2 \leftrightarrow O_2^- \tag{1.5}$$

$$O_2^- + H^+ \leftrightarrow \cdot HO_2^- \tag{1.6}$$

$$\cdot HO_2^- + \cdot HO_2^- \leftrightarrow H_2O_2 + O_2 \tag{1.7}$$

$$h^+ + OH^- \leftrightarrow \cdot OH \tag{1.8}$$

$$H_2O_2 + e^- \leftrightarrow \cdot OH + OH^+ \tag{1.9}$$

Equation 1.3 shows the generation of an electron-hole pair. The standard redox potentials of these conduction band electrons (e^-) and the photo-generated holes (h^+) are -0.52V and +2.53V respectively,[20] compared to the standard hydrogen electrode at pH=7. The subsequent equations (1.4-1.9) show the generation of hydroxyl radicals (·OH) whose redox potential is +2.27V versus the standard hydrogen electrode at pH=7.[20] All of these reactions are reversible, but also the electrons and holes have a tendency to recombine after they have been generated. The depending factor on whether a semiconductor can be a viable photocatalyst is this recombination rate of the electron-hole pair.

1.2.3 Crystallinity

TiO_2 exhibits several crystalline polymorphs: the thermodynamically stable rutile phase, the metastable phases anatase and brookite, and several high pressure phases.[21] This thesis will be concerned with the anatase and rutile phases as they are by far the most common polymorphs to be used in photocatalysis.[22] Despite both having a tetragonal crystal structure, the properties and symmetry of these two polymorphs are dissimilar (Table 1.1). In terms of catalysis, anatase is more efficient than rutile because there is less chance of an electron and hole recombination occurring,[23] however it is less stable thermodynamically.[24] The stability of the various TiO_2 phases has been reported as size dependent; rutile is said to be the most stable phase for particles above 35 nm, whereas anatase is stabilised in particles below 11 nm.[25]

	Rutile	**Anatase**
System	Tetragonal	Tetragonal
Space Group	D_{4h}^{14}-$P4_2/mnm$	D_{4h}^{19}-$I4_1/amd$
Lattice constants (nm)	a, b = 0.4584 c = 0.2953	a, b = 0.3733 c = 0.937
Band Gap (eV)	3.05	3.26

Table 1.1. The similarities and differences in the rutile and anatase polymorphs of TiO_2.[26]

The basic building block for both the rutile and anatase polymorphs is a titanium atom surrounded by six oxygen atoms, which are in a distorted octahedron configuration. In anatase, there is a significant deviation from a 90° bond angle (figure 1.7). Rutile's neighbouring octahedral share a corner along (110)-type directions, whereas in anatase the corner sharing octahedra form (001) planes.[24]

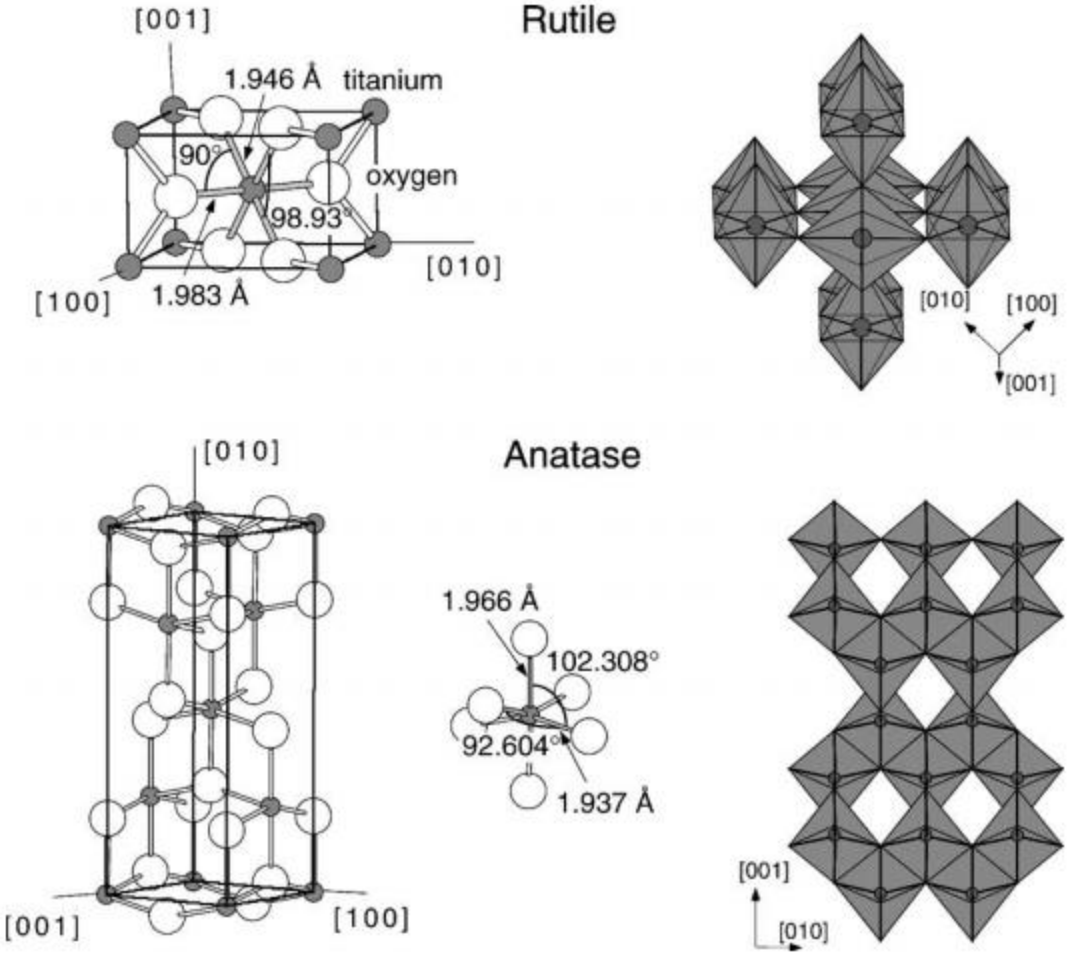

Figure 1.7 Bulk structures of rutile and anatase. Slightly distorted octahedra are the basic building blocks for both structures. Bond lengths and angles of the Ti atoms are indicated. The stacking of the octahedra is indicated on the right. This figure is reproduced from Diebold.[24]

The photocatalytic performance of TiO_2 is highly dependent on its crystallinity and phase ratio.[27,28] By investigating the transition between the phases gives us a better understanding of how the photocatalytic mechanism proceeds.

This thesis will also discuss the non-crystalline / amorphous aspects of the TiO_2 structure. The characteristics of the amorphous TiO_2 local structure has some variance. It has been reported by Chen *et al.* that the titanium coordination number was $Z_{Ti\text{-}O} = 4.8$,[29] whereas Yeung *et al.* claim the coordination number to be $Z_{Ti\text{-}O} = 4.5$.[30] Despite the differences in reported values, it can be concluded that the local structure of amorphous TiO_2 shows a reduction in the coordination number. Zhang *et al.* describe a model for an amorphous TiO_2 nanoparticle as having a distorted surface layer along with a slightly distorted, anatase-like core.[31] It is claimed that the surface layer has reduced coordination of Ti and O atoms and a more porous structure.

1.2.4 Surface Chemistry

Surface chemistry plays a vital part in the efficiency of photocatalysis as it is an interface-based reaction. TiO_2 has a high surface area in both polymorphs of anatase and rutile. High surface areas result in an increased density of unsaturated or terminated bonds on the titania surface, known as “localised states”. These localised states provide electrons that have energies between the conduction band and the valence band as well as forming trapping sites for the electron-hole pairs that are photo-generated.[32]

Compared with other semiconductors, both anatase and rutile have low charge carrier recombination rates which is beneficial for photocatalysis.[33] The general consensus is that a semiconductor needs to have an exciton lifetime of at least 0.1 ns for a chemical reaction to be catalysed.[34] Titania far exceeds this, with lifetimes of pure anatase being $t_{½} \approx 0.5$ ms and pure rutile as $t_{½} \approx 20$ ms.[35]

Another factor contributing to efficient photocatalysis is the density of adsorbed species on the semiconductor surface. If radicals cannot be generated at the rate that the electron-hole pairs reach the surface then photocatalytic efficiency is lost.

Knowledge of amorphous / non-crystalline TiO_2 surface chemistry is less well defined. Previous studies indicate that the concentration of uncoordinated structural units on the amorphous TiO_2 surface is far greater than in the bulk.[36] These can be considered analogous to the oxygen deficiencies that are present in crystalline TiO_2.

1.2.5 Enhanced Photoactivity

Reports of rutile-anatase mixed phase photocatalysts with enhanced photoactivity are numerous.[28,37-42] The consensus is that the increased activity is due to improved charge carrier separation from trapping electrons in rutile, hence lowering the recombination rate of the electron-hole pairs. The most common mixed phase TiO_2-based photocatalyst that is commercially available is Degussa P25. The high performance of Degussa P25 is said to stem from its enhanced photoactivity in conjunction with its large specific surface area.[43]

Relative quantities of rutile and anatase in mixed systems are usually determined by the X-ray diffraction method of Spurr and Myers (equation 1.10).[44] In which, the ratio of the rutile (110) peak at 27.355° 2θ to the anatase (101) peak at 25.176° 2θ is taken. The relative intensities of these peaks is used to give the weight fractions of anatase.and rutile.

$$(A)\% = \frac{I_A}{I_A + 1.26 I_R} \times 100 \tag{1.10}$$

However, as mentioned, photocatalytic performance is not based solely on bulk phase composition. Zhang *et al.* showed discrepancies between the bulk composition determined by XRD and the surface phases determined by Raman spectroscopy.[45] The resultant photocatalytic activity was directly dependent on the surface phase rather than the bulk.

In Chapter 3, a comparison between XRD and XPS for TiO_2 phase quantification is presented. A direct correlation between the surface phase and the photoactivity is important to establish as the surface and bulk phases can vary dramatically, especially when transitioning from anatase to rutile TiO_2.

It has also been shown that the photoactivity of TiO_2 can be enhanced by introducing dopants. A wide variety of dopants have proven to be effective, but one of the most promising enhancements is nitrogen doping. It is possible to lower the band gap into the visible region of light by incorporating a small percentage of nitrogen into the lattice.[46] The exact mechanism via which the catalysis proceeds in tandem with nitrogen still remains uncertain, but if efficient visible light photocatalysis could be achieved with TiO_2 the subsequent beneficial applications would be vast. There are three prevailing theories for how nitrogen doping of titanium dioxide generates visible light photoactivity. It could be due to substitutional nitrogen doping, or interstitial doping, or nitrogen does not play a role and the real reason is that doping (interstitial or substitutional) promotes the formation of oxygen vacancies.[47,48] To maintain electroneutrality, dopants must be compensated by auxiliary charged species such as electrons, holes, oxygen vacancies, or protons. In order to effectively describe the addition of dopants and the subsequent formation of defects, Kröger and Vink devised a notation which relates the charge and position of the point defect to the perfect structure of the compound.

The general formula for a defect is written as: $\mathbf{M_S^C}$

- **M** corresponds to the species (atoms – e.g. Ti, N, Si, etc., vacancies – V or v, interstitials – i, electrons – e, or electron holes – h).
- **S** indicates the specific lattice site the species occupies. For example, when nitrogen occupies an oxygen site, the **M** would be replaced by N, and the **S** would be replaced by O to indicate that the oxygen has been substituted for a nitrogen.
- **C** is indicative of the electronic charge of the species but relative to the site that it occupies. So, the charge of the species is calculated by taking the charge on the current site minus the charge on the original site. × is used to indicate a null charge, • corresponds to a single positive charge, and **'** signifies a single negative charge.

So in the example of nitrogen doping via ammonolysis seen in Chapter 4 of this thesis, the balanced equations for the formation of oxygen vacancies would be:

$$2\mathrm{NH_3(g)} + 3\mathrm{O_O^\times} = 2\mathrm{N_O'} + \mathrm{v_O^{\bullet\bullet}} + 3\mathrm{H_2O(g)} \qquad (1.11)$$

$$2\mathrm{NH_3(g)} + 3\mathrm{O_O^\times} = 2\mathrm{N_i'''} + 3\mathrm{v_O^{\bullet\bullet}} + 3\mathrm{H_2O(g)} \qquad (1.12)$$

Equation 1.11 shows that when the nitrogen doping is substitutional, the oxygens in the lattice are directly replaced with nitrogen. However, to balance the charge, an oxygen vacancy must be created for every two nitride ions incorporated. Hence substitutional nitrogen doping promotes oxygen vacancies in the lattice.[49]

If the nitrogen doping is interstitial, the oxide ions are not directly replaced. Instead, the nitrogen incorporates itself in some form into the lattice on the interstitial sites with the formation of a Ti-O-N bond.[48] Interstitial doping will occur under mild ammonolysis conditions. Equation 1.12 shows that the dopants in the interstitial sites also promote the formation of oxygen vacancies. However, the greater the concentration of interstitial doping that occurs, the more oxygen vacancies are created, meaning that an increase in substitutional doping will occur. It is therefore a delicate balance to achieve a sample that is doped in just one way, and most N-TiO_2 samples are a combination of interstitially and substitutionally doped with oxygen vacancies pervading throughout.

Once nitrogen is incorporated into the TiO_2 lattice it can either alter the band structure or suppress how efficiently the electron-hole pairs recombine.[50] It has been shown in anatase titania that if the concentration of nitrogen in the lattice is relatively low then it promotes a large decrease in the formation energy of oxygen vacancies from 4.2 eV to 0.6 eV.[51] The theory of why this occurs is that the excess electrons that are created in the oxygen vacancies get trapped on the nitrogen sites. These oxygen vacancies have been credited with enhancing the photocatalytic activity of TiO_2, however some authors debate as to whether the presence of the oxygen vacancies actually leads to a poorer performance as they act as recombination sites for the electron-hole pairs.[52]

The type of doping that occurs can be deduced via XPS techniques. It is now generally agreed upon that there will be a peak exhibited at approximately 396 eV if the sample has been doped substitutionally, whereas interstitially doped nitrogen exhibits a peak at 400 eV.

From previous DFT calculations modelling the density of states within N-doped anatase TiO_2,[53] it has been shown that the valance band increased in energy by approximately 0.14 eV when substitutional nitrogen doping occurred. This is due to the mixing of oxygen and nitrogen 2p orbitals. With interstitial N-doping, it has been calculated that a new, narrow band is created approximately 0.74 eV above the valence band.[54]

1.2.6 Interconversion

Controlling the kinetics of the anatase-rutile transformation is understandably desirable, especially for high temperature applications.[55,56] If anatase gives the best performance but is required to operate at high temperatures, then a phase transformation may occur which alters the efficiency and lifetime of the device. This is pertinent to gas sensors or gas separation membranes.

The phase that is generated is highly dependent on the synthesis method used. The main physical variables that can be altered are synthesis time and temperature. The understanding is, that for most cases, anatase will begin its irreversible transformation to rutile at temperatures above 600 °C.[57-59] However, it relevant to note that the transformation is not instantaneous and therefore a number of kinetic parameters need to be taken into account, such as: particle size, surface area, impurities, atmosphere etc. and as such, reports for the anatase to rutile transition (ART) have ranged from 400-1200 °C.[45,58,60,61]

The anatase to rutile transformation is reconstructive, meaning that during the transformation, bonds are broken and subsequently reformed,[62] as opposed to displacive transformations which distort but do not break the bonds. The ART involves a contraction along the *c*-axis and an overall volume contraction of ~8%.[63] This volume decrease during the ART explains the higher density of rutile relative to that of anatase.

1.3 Current Research

Current research that is pertinent to my project is described below. The synthetic approaches to producing photocatalytic TiO_2 will be outlined with specific emphasis on crystal phases produced, along with reference to doping techniques to enhance the photoactivity, and finally the applications of the products formed.

1.3.1 Synthesis Techniques

There are numerous ways that TiO_2 is currently being produced. Each technique has specific advantages and drawbacks. The most common of these synthesis techniques and the phases they achieve are outlined in table 1.2.

In this thesis, one of the wet chemical methods for producing TiO_2 was via a sol-gel technique. The sol-gel synthesis is cheap and performed at ambient temperatures. The chemical composition of the product is easily controlled. The process has the possibility of dopants being added directly into the sol, which will be fully dispersed in the final product.

A newly emerging and therefore less common technique is liquid phase deposition. This differs from a hydrothermal synthesis in that it is performed at much lower temperatures and with no thermal decomposition step being involved. This again advantageous, as no costly reaction conditions are required, and the synthesis can be performed in a single reaction vessel.

Synthesis	**Mechanism**	**Phases formed**				**References**
		Amorphous	**Anatase**	**Rutile**	**Anatase + Rutile**	
Room temperature hydrolysis of $TiCl_4$	Precipitation from room temperature solutions of $TiCl_4$	✓				64,65
Room temperature sol-gel synthesis	Hydrolysis of $TiCl_4$ or an organo-metallic compound	✓				66-69
Flame pyrolysis of $TiCl_4$	Combustion of $TiCl_4$ with oxygen; used in industrial processes		✓		✓	70
Solvothermal / hydrothermal	Precipitation of TiO_2 from aqueous or organic solution at elevated temperatures		✓	✓	✓	58,59,71-74
Chemical vapour deposition	Deposition of Ti-containing volatile precursors under a variety of reaction conditions	✓	✓	✓	✓	75,76
Physical vapour depostion	Deposition of evaporated Ti and its subsequent oxidation	✓	✓	✓	✓	77,78

Table 1.2. Common current synthesis methods and the resultant phases formed. Table adapted from Hanaor and Sorrell.[63]

1.3.2 Doping Techniques

Currently, the attempts made to reliably lower the band gap of TiO_2 can be separated into three areas: Doping with transition metal ions and anions which produces intermediate states in the band gap of TiO_2,[79,80] incorporating a photo-sensitizer such as another semiconductor[81] or an organic compound,[82] or the formation of reduced TiO_x by some method.[83]

Of these approaches, the viability of doping seems to be high. There have been several methods employed in order to dope titania including chemical vapour deposition,[84] hydrothermal synthesis,[85] pulsed laser deposition,[86] various sputtering techniques.[46,87,88] Sol-gel and hydrothermal doping methods are also often used. They have a huge number of advantages because they are cheap, effective, require minimal laboratory equipment and take very little time.

1.3.3 Applications

Products derived from sol-gel and liquid phase deposition processes have wide-ranging applications such as electronics[89,90], sensors[91], medicine[92-94], and optics[95-97]. Potential outcomes of photocatalytic titanium dioxide research can be split up into three categories: Green energy applications (water splitting for hydrogen production[98,99], dye-sensitised solar cells (DSSC's)[100,101]), environmental applications (water treatment[102-104], air purification[105,106]), and thin films and coatings (self-cleaning coatings[107-109], self-sterilising coatings[110-112], anti-fogging coatings[113]).

Theoretically the research conducted in this thesis has far-reaching connotations in all of these areas, but the main focus was in the domain of thin films and the development of self-cleaning coatings.

1.4 Aims

This thesis presents the results of an investigation into various crystallinities of titanium dioxide and the subsequent photocatalytic activities that are revealed. The aim of this investigation was to further the understanding of what role TiO_2 crystallinity plays in the photocatalytic process. Specifically, the aim was to clarify the possible synergic effects of mixed-phase systems, investigate the relationship of surface area vs crystallinity, and to explore the potential of non-crystalline / amorphous TiO_2 photocatalysts. Doped titanium dioxide photocatalysts were also to be examined as a comparison to the pure samples, and to see what possible changes to the crystallinity occur during the synthesis. The surface structure of the systems was to be especially emphasised as photocatalysis occurs at the interfaces between compounds. As such, the surface-sensitive technique of X-ray photoelectron spectroscopy (XPS) was to be the principle method of analysis, with analogies drawn to X-ray diffraction (XRD) techniques, as any discrepancies that may occur between results.

Chapter 2: Experimental Section

2.1 Introduction

This chapter outlines the experimental methods used throughout this research. Both the principles of the syntheses, and the analytical techniques used to characterised samples will be discussed. The TiO_2 films and powders were all synthesised by wet chemical means.

2.2 Syntheses

2.2.1 Sol-Gel Synthesis

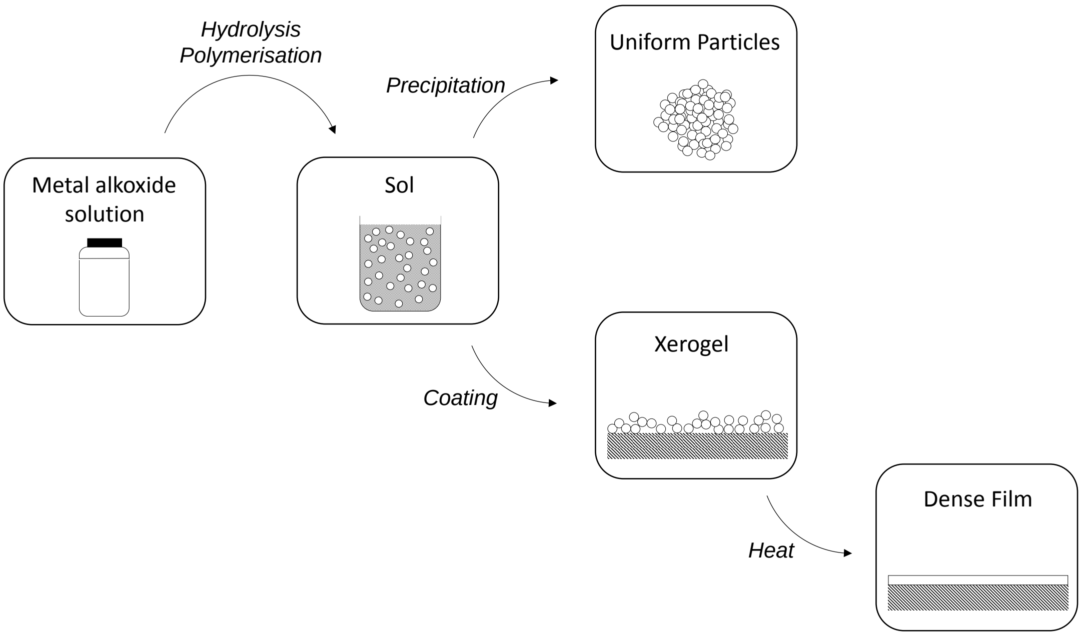

Figure 2.1. A generalised sol-gel synthesis of powders and thin films.

The sol-gel process is a method used to fabricate metal oxides. It involves the conversion of monomers into a colloidal solution known as a sol. This sol then acts as the precursor for an integrated network of uniform particles or polymers known as a gel. In the sol-gel synthesis, typically the precursor is a metal alkoxide.

Figure 2.1 shows a simplified version of the chemical procedure used in this thesis. The sol can either be deposited onto a substrate as it is, to form a thin film, or used to synthesise nanopowders of the metal oxide by a process of precipitation and filtration (usually by adding water to the sol).

The chemical process that occurs in a sol-gel synthesis is a two-step procedure. Equation 2.1 shows the first step which is a hydrolysis reaction.

$$\mathrm{Ti(OBu)}_n + \mathrm{H_2O} \rightarrow \mathrm{Ti(OBu)}_{n-1}\mathrm{(OH)} + \mathrm{BuOH} \tag{2.1}$$

$$2\mathrm{Ti(OBu)}_{n-1}\mathrm{(OH)} \rightarrow \mathrm{Ti_2O(OBu)}_{2n-2} + \mathrm{H_2O} \tag{2.2}$$

$$\mathrm{Ti(OBu)}_n + \mathrm{Ti(OBu)}_{n-1}\mathrm{(OH)} \rightarrow \mathrm{Ti_2O(OBu)}_{2n-2} + \mathrm{BuOH} \tag{2.3}$$

Equation 2.2 shows the dehydration of the metal alkoxide and equation 2.3 show the dealcoholation. This is the standard synthesis for all sol-gel reactions, and the alkoxide used throughout this thesis is titanium n-butoxide.

The hydrolysis step needs to be effectively controlled to ensure the homogeneous formation of titanium oxide networks. Therefore, as well as the metal alkoxide precursor, a chelating reagent (diol, diketonate, carboxylic acid, etc.) is usually added. The condensation step then agglomerates the particles of the sol into larger metal oxide mass.

The specific sol-gel synthesis used in this thesis adds supplementary acetylacetone (acac), isopropanol, and acetonitrile into the sol. In this case, the acetylacetone is the chemical that initiates the bridging of the titanium butoxide, because it acts as a ligand is able to chelate between the titanium centres. This starts the formation of the colloids, containing the Ti-O-Ti bridges.

The isopropanol is added as an aqueous mixture and initiates the hydrolysis of the Ti centres which starts to link the colloids together. If there is too much water added to the solution at this point, the colloids would grow too quickly and a white precipitate of titania would be seen, hence why the water is added mixed with the isopropanol.

Finally, the acetonitrile acts to stop further hydrolysis, as it coordinates to the Ti centres. Although it can be easily displaced, it helps to slow the growth of the colloids.

In the formation of both powders and films, a calcination step is required to remove the organic molecules from the final product. Temperature plays an important part in the product formed, so care must be taken to not induce a phase transformation with very high calcination temperatures.

The sol-gel synthesis is cheap and the chemical composition of the product is easily controlled. The process has the possibility of dopants being added directly into the sol, which will be fully dispersed in the final product.

2.2.2 Spin-Coating

Spin coating is a technique in which a thin film of approximate uniform thickness is produced on a flat substrate by depositing a small amount of liquid and rotating at high velocity. One of the main areas where spin coating techniques are used is the microelectronics industry in which silicon wafers are coated with a photoresist film for the first stages of lithography.[114]

The spin coating process can be divided into four main stages (figure 2.2). The first stage is the deposition of an excess of viscous liquid onto the substrate. The substrate can either be stationary or rotating slowly. An excess of liquid is used so that the fluid front will not dry before reaching the edges of the substrate. The second stage is an acceleration up to the desired rotation speed. The third stage is simply spinning the substrate at the required rpm for several seconds. Film thicknesses are roughly inversely proportional to the square root of the spin speed. The fourth stage is the evaporation stage, and is important for removing excess solvent and reducing the film thickness.[115]

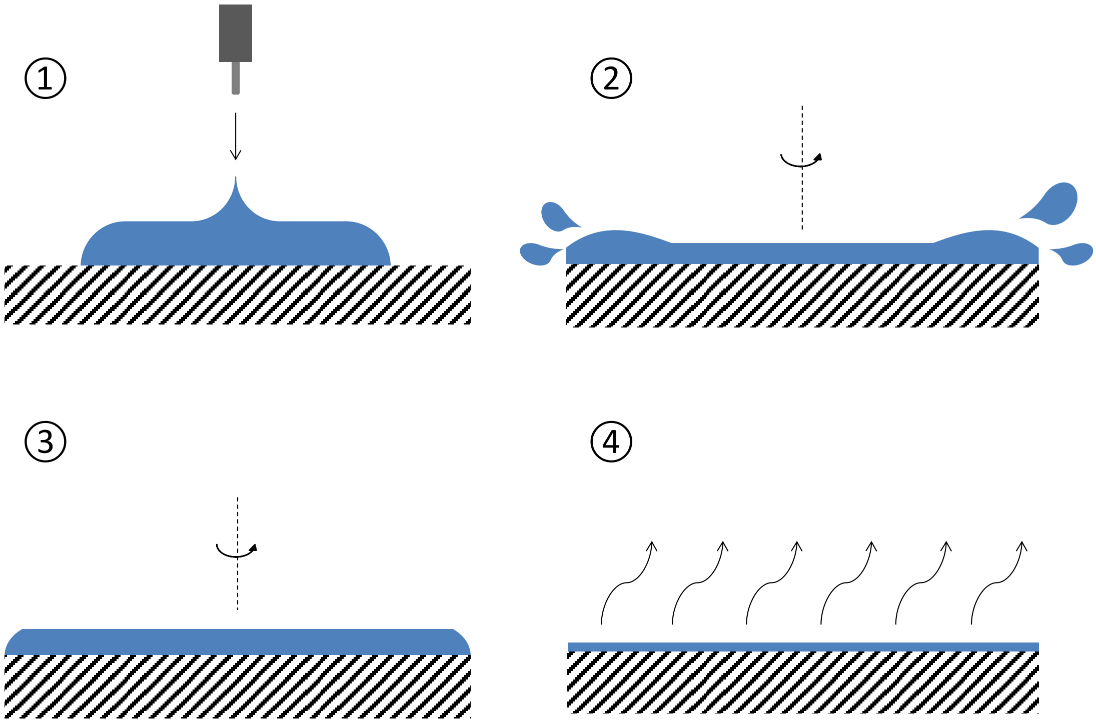

Figure 2.2. The four stages of spin coating. Deposition (1), acceleration (2), spinning (3), and evaporation (4)

2.2.3 Liquid Phase Deposition (LPD)

Liquid phase deposition can be defined as the formation of an oxide thin film from an aqueous solution of a metal-fluoro complex $[MF_n]^{m-n}$ which is slowly hydrolysed by adding water or boric acid. First patented in the 1980s by Kawahara *et al.*,[116] the process is similar to hydrothermal / solvothermal and chemical bath syntheses but allows for much better control of hydrolysis reactions and of the supersaturation of the solution.

Ammonium hexafluorotitanate (AHFT) in aqueous solution forms $[TiF_6]^{2-}$ anions. Equation 2.4 shows the equilibrium proposed by Schmitt *et al.*[117]

$$[\mathrm{TiF_6}]^{2-} + n\mathrm{H_2O} \rightleftharpoons [\mathrm{TiF}_{6-n}(\mathrm{OH})_n]^{2-} + n\mathrm{HF} \qquad (2.4)$$

Equation 2.5 reveals that this equilibrium can be changed by the addition of H_3BO_3 which acts as an F^- scavenger, and thus forms a more stable complex.

$$\mathrm{H_3BO_3} + 4\mathrm{HF} \rightleftharpoons \mathrm{HBF_4} + 3\mathrm{H_2O} \qquad (2.5)$$

This addition of H_3BO_3 means that the F^- ions that are not coordinated get consumed, which in turn accelerates the hydrolysis reaction. So the thin films are formed by the dehydration reaction of $[Ti(OH)_6]^{2-}$, which was originally generated by the hydrolysis reaction of $[TiF_6]^{2-}$. The deposition rate-determining step is the consumption of F^- by H_3BO_3.

2.3 Compositional Analysis

Investigating the atomic and electronic structures of compounds requires interaction with exploratory physical techniques. The basic principles of these techniques will be outlined below.

2.3.1 X-Ray Photoelectron Spectroscopy (XPS)

X-rays of a known wavelength are used to eject a photoelectron from the sample. The kinetic energy of the photoelectron is then determined, which can then be used to infer the binding energy of the electron when it was originally in the atom. Equation 2.6 shows how these energies are related.

$$BE = E - KE - \phi \qquad (2.6)$$

Where *BE* is the binding energy of the electron in the atom, *E* is the energy of the incoming X-ray, and ϕ is the calibrated work function for the XPS instrument.

XPS can elucidate the oxidation state of specific elements, the quantity of specific elements present in a sample, and also the chemical environment that elements are in by analysis of the photoelectron binding energy.[118]

Spectra are created by plotting the binding energy against the intensity measured from the photoelectrons. The core atomic orbitals of different elements can be assigned depending on the binding energy of the photoelectrons. For core *s* orbitals, the spectra will always give a singlet peak, due to the angular momentum number, $l = 0$. For other photoelectrons arising from orbitals where $l > 0$, the spectra reveals a doublet peak due to spin orbit coupling.

As mentioned, the position of the photoelectron peak is determined by the binding energy of the electron in the atom. However, the chemical environment of that element can shift the peak higher or lower. For example if the element is present in a positive (cationic) oxidation state, its photoelectron will have a higher binding energies than if it were uncharged. Peaks of one element in different chemical environments often overlap in the photoelectron spectra, so the peaks need to be fitted in order to determine the quantities. The quantity of elements present and composition of a sample can also be determined by XPS, by comparing the relative intensities of the photoelectron peaks. Sensitivity factors have to be used in this case, as the ionisation cross-section varies between each orbital.

The photoelectron spectra show peaks broadening over an energy range with peak shapes that follow a Gaussian-Lorentzian fit. Broadening occurs due to the uncertainty principle, with the width of the peak being determined by the lifetime of the excited atomic energy level. This explanation only accounts for the Lorentzian shape. The Gaussian shape comes from instrumental factors such as thermal broadening, the width of the X-ray line, and the instrument's resolution.

XPS is a surface specific technique because the inelastic mean free path of (Al k-alpha) photoelectrons is approximately 2 nm in a solid. However, ion gun etching can be used to penetrate deeper into the sample and a depth profile can be created.

XPS was carried out in a two chamber Thermo K-alpha spectrometer using a monochromated Al K-alpha X-ray source (1486.6 eV) in constant analyser energy mode. X-rays were focused to a 400 micron spot at the sample surface, which defined the analysis area. Sample charging was prevented by use of a dual beam flood gun. High resolution spectra, including valence bands, were recorded at 50 eV pass energy, and survey spectra were recorded at 200 eV pass energy.

2.3.2 X-Ray Diffraction (XRD)

The atomic and molecular structure of a material can be determined by X-ray crystallographic techniques, in which an incident beam of X-rays can diffract into many different directions when irradiating the sample, shown in figure 2.3. Diffraction of light from Miller planes in crystalline samples occurs in accordance with the Bragg equation (equation 2.12). Bragg's law can be derived by considering a single monochromatic wave acting upon aligned lattice planes, seperated by distance **d**, at angle **θ**. The points **A** and **C** are on the same plane, and point **B** is on the plane below. Points **ABCC'** form a quadrilateral.

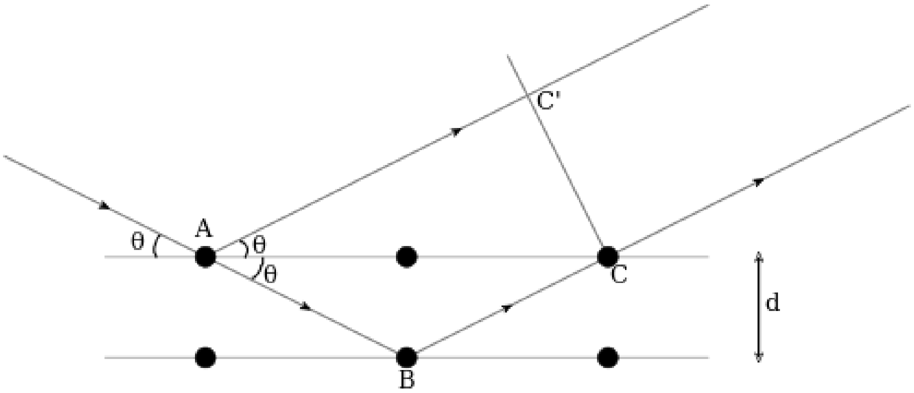

Figure 2.3. An incident beam of monochromated X-rays acting upon aligned lattice planes in a crystalline sample. The planes are separated by distance *d*, and the beam is at angle *θ* to the plane.

Naturally, there will be a path difference between the X-ray that gets reflected along **AC'** and the X-ray that takes the path of **AB** and then **BC**. The path difference can be described as:

$$(AB + BC) - (AC') \tag{2.7}$$

The waves will only undergo constructive interference and remain in the same phase if this path difference is equal to an integer value of the wavelength. Hence:

$$(AB + BC) - (AC') = n\lambda \tag{2.8}$$

Therefore:

$$AB = BC = \frac{d}{\sin\theta} \; and \; AC = \frac{2d}{\tan\theta} \tag{2.9}$$

And accordingly:

$$AC' = AC \cdot \cos\theta = \frac{2d}{\tan\theta}\cos\theta = \left(\frac{2d}{\sin\theta}\cos\theta\right)\cos\theta = \frac{2d}{\sin\theta}\cos^2\theta \tag{2.10}$$

Combining everything:

$$n\lambda = \frac{2d}{\sin\theta}(1 - \cos^2\theta) = \frac{2d}{\sin\theta}\sin^2\theta \tag{2.11}$$

Which simplifies to:

$$n\lambda = 2d\sin\theta \tag{2.12}$$

Where **n** is a positive integer, **λ** is the wavelength of the incident X-ray, **d** is the interplanar distance between the lattice planes, and **θ** is the scattering angle. The variety of light that is used are X-rays because they are of the order 10^{-10} m, which corresponds to the distance between the Miller planes.

Copious amounts of information can be gathered from XRD, including the crystalline phases that are present in a sample, any preferred orientation, determination of the unit cell dimensions, and a measurement of how pure the sample is. Thin film samples can also be characterised with specialised XRD techniques; the lattice mismatch between the film and substrate can be determined to infer the stress and strain, and the thickness, roughness, and density of the film can be revealed with glancing incidence X-ray reflectivity measurements. Deriving further from the Bragg equation, equation 2.19 reveals how the size of the crystallites can be determined and is known as the Scherrer equation.

If both sides of the Bragg equation are multiplied by an integer **m**, such that **md=τ**, where **τ** is the thickness of the crystal, this leads to **n=1**:

$$m\lambda = 2md\sin\theta \tag{2.13}$$

$$\therefore m\lambda = 2\tau\sin\theta \tag{2.14}$$

This can be said to be the **mth** order reflection from a set of lattice planes with an interplanar distance **τ**. If both sides of the equation are differentiated (remembering that **mλ** is a constant), it gives:

$$0 = 2\,\Delta\tau\sin\theta + 2\,\tau\cos\theta\,\Delta\theta \tag{2.15}$$

Considering that **Δθ** can be positive or negative, and that only absolute values are of interest, this equation can be simplified and rearranged to:

$$\tau = \frac{\Delta\tau\sin\theta}{\cos\theta\,\Delta\theta} \tag{2.16}$$

Due to the fact that the smallest increment in **τ** is **d**, using **Δτ=d**, and substituting **λ/2** for **d·sinθ** from Bragg's law, gives:

$$\tau = \frac{\lambda}{2\cos\theta\,\Delta\theta} \tag{2.17}$$

Then substituting **β** for **2·Δθ**, which is the angular width, gives:

$$\tau = \frac{\lambda}{\beta\cos\theta} \tag{2.18}$$

Which is essentially the Scherrer equation, however, most versions that are written for a more sophisticated analysis, contain a dimensionless shape factor (which is typically 0.9 but can vary with actual shape of the crystallite):

$$\tau = \frac{K\lambda}{\beta\cos\theta} \tag{2.19}$$

Where **τ** is the mean size of the crystallites, **K** is the shape factor and **β** is the line broadening at half the intensity of the peak.

XRD was carried out using a Bruker D4 ENDEAVOR with a Cu K-alpha X-ray source of 1.54 Å and a custom Seifert analytical X-ray system with a Mo K-alpha source of 0.71 Å.

2.3.3 Ultraviolet-Visible Spectroscopy (UV-vis)

Ultraviolet-visible spectroscopy is a technique that determines the absorption or reflection spectrum of a sample in the ultraviolet-visible region. Non-bonding electrons or π-electrons in molecules can absorb UV-vis light energy and become excited to higher anti-bonding molecular orbitals. The more easily the electrons can be excited, the longer the wavelength of light it can absorb. Therefore, organic dyes like methyl orange with a high degree of conjugation can absorb UV and visible light and can be used in photocatalytic degradation experiments.

Using the Beer-Lambert law, the concentration of the absorbing species can be determined. The absorbance of a sample is directly proportional to the concentration of the absorbing species and the path length.

The UV-vis spectrophotometer can also be configured to measure reflectance by measuring the intensity of light reflected from a sample (I) and then comparing it to the intensity of light reflected from a reference material (I_o). The ratio I/I_o is the reflectance (%R).

The band gap of materials can be inferred from UV-vis spectra by a simple conversion to a Tauc plot with the linear portion extrapolated to the x-axis to give the band gap value.

UV-vis was carried out using a Shimadzu UV-2600 spectrophotometer.

2.3.4 Brunauer–Emmett–Teller (BET)

Brunauer–Emmett–Teller theory aims to explain the adsorption of gas molecules on a solid surface. This in turn serves as the basis for the measurement of the specific surface area of the material via nitrogen adsorption measured as a function of relative pressure. The surface area is then determined by calculating the amount of gas adsorbed corresponding to a monomolecular layer on the material's surface. BET encorporates external area, and pore area evaluations, to determine the total specific surface area.

BET surface area measurements of the powders were carried out on a Micromeritics ASAP 2420 Accelerated Surface Area and Porosimetry System. Each sample was weighed to approximately 0.2 g, degassed at 150 °C in N_2 for 12 hours, and then analysed.

2.3.5 Scanning Electron Microscopy (SEM)

A scanning electron microscope produces an image of the sample surface by scanning a fine electron beam across it. The electrons interact with atoms in the sample and become scattered in various ways. Secondary and backscattered electrons can be detected which gives information about the surface topography and atomic weight of the sample. The field emission SEM used in this thesis has a resolution of 1 nm at 15 kV and samples were recorded in high vacuum.

2.3.6 Transmission Electron Microscopy (TEM)

A transmission electron microscope can be used to image thin (<100 nm) sections of materials at high resolution. It can also be used to determine crystal structure using bright-field images, dark-field images and diffraction patterns.

The TEM used in this thesis is a 300 kV field-emission microscope capable of resolving atom columns separated by only 0.17 nm.

2.3.7 X-Ray Absorption Spectroscopy (XAS)

X-ray absorption spectroscopy is a technique that is used to determine in detail the electronic structure and local geometric environment of a material. Typically the experiment is performed at synchrotron radiation sources which provide tunable X-rays with suitable intensity. The data is obtained by tuning the photon energy using a crystalline monochromator. Once tuned appropriately, the X-rays are absorbed, and core electrons from the sample can be excited to higher energies.

The absorption edge in XAS depends on which core electron in the sample is excited, and principle quantum numbers determine the absorption edges' name: $n = 1$, 2, and 3 refer to edges K-, L-, and M- respectively, shown in figure 2.4.

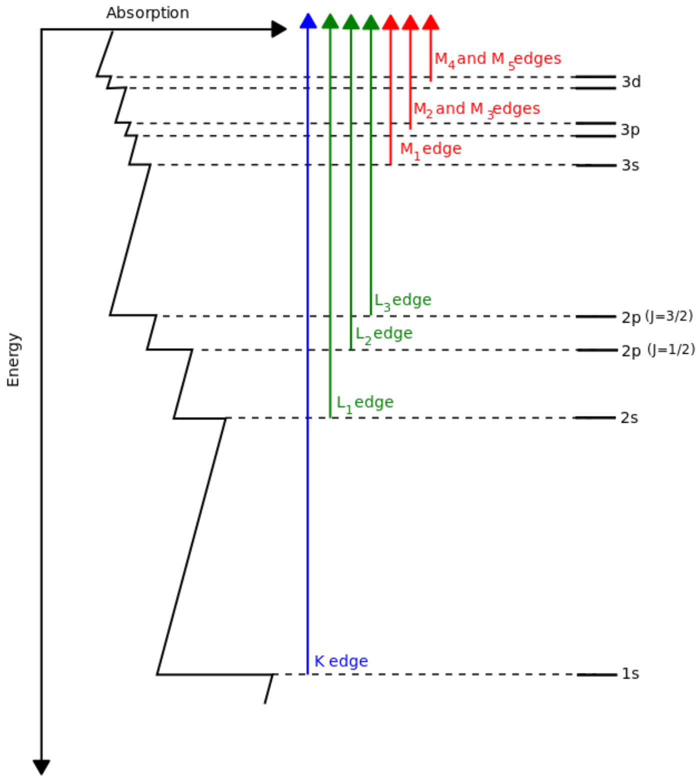

Figure 2.4. The allowed transitions that occur in XAS and the respective names of the edges in accordance with their principle quantum numbers. This diagram was originally produced by Tenderholt.[119]

In XAS data there are the three main regions found within the spectra:

The first is the "absorption threshold", which is determined by the transition to the lowest unoccupied states. The shapes of these transitions is dependent on the material; states at the Fermi energy in metals give what's referred to as a "rising edge" with an arc tangent, whereas, the bound core excitons that are present in insulators impart a Lorentzian shape to the line that is present in the pre-edge region (at energies lower than the transitions to the lowest unoccupied state). This phenomenon of XAS pre-edge peaks will be seen in Chapter 5 of this thesis.

The second region of XAS data that is important to discuss is the X-ray Absorption Near-Edge Structure (XANES). This region is mainly indicative of core transitions to quasi bound states, and generally occur for photoelectrons with kinetic energies ranging from 10-150 eV above the chemical potential.

The third and final region that can be examined is known as the Extended X-ray Absorption Fine Structure (EXAFS) which is dominated by the ejected, high-energy photoelectron being scattered by the neighbouring atoms. An example of an X-ray absorption spectrum and where these regions occur can be seen in figure 2.5.

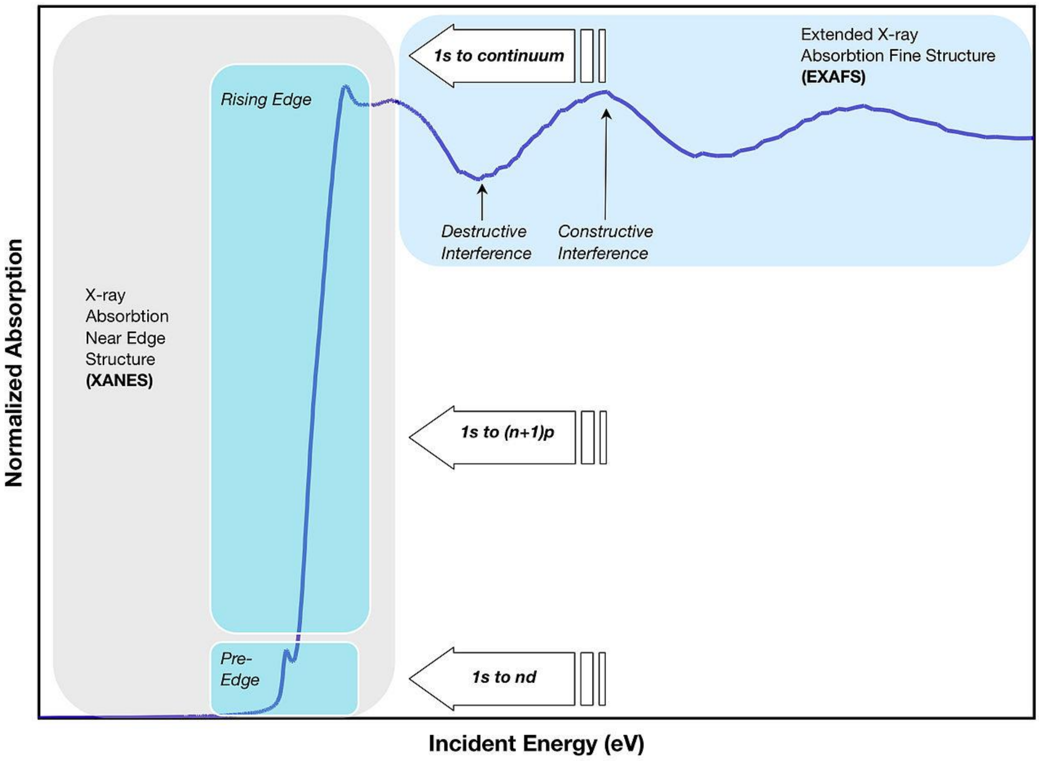

Figure 2.5. An example shape of an X-ray absorption spectrum with the respective regions highlighted. This diagram was originally produced by Qayyam.[120]

The instrument used in this thesis was the X-Ray Absorption Fine Structure for Catalysis (XAFCA) beamline at the Singapore Synchrotron Light Source (SSLS) capable of performing energy ranges of 1.2 – 12.8 KeV at temperatures of 4 – 1000 K. In this case, the titanium K-edge was recorded at ambient conditions.

2.3.8 Photoelectron Spectroscopy in Air (PESA)

Photoelectron spectroscopy refers to energy measurement of electrons emitted from solids, liquids, or gases by the photoelectric effect. Specifically, PESA is this measurement performed in air. This technique allows for the determination of the binding energies of electrons in a substance. The ionisation energy can be provided by X-ray or UV photons.

The instrument used in this thesis was a Riken Keiki Model AC-2 photoelectron spectrometer. The analysis was conducted in air at atmospheric pressure with a UV source.

2.4 Photocatalytic Analysis

In order to compare the effectiveness of newly developed semiconductor photocatalysts, there are several agreed standard methods of assessing the photocatalytic activity of novel thin films and powders. This section will detail the methods used in this thesis.

2.4.1 Methylene Blue

The methylene blue test is one of the most popular methods for assessing the photocatalytic activity of TiO_2 thin films and powders. It proceeds by photobleaching the cationic, thiazine dye, methylene blue. The overall reaction has been summarised in equation 2.20.

$$2C_{16}H_{18}N_3S^+ + 51O_2 \rightarrow \tag{2.20}$$
$$32CO_2 + 6HNO_3 + 2H_2SO_4 + 2H^+ + 12H_2O$$

The initial step in this reaction is the adsorption of the dye onto the surface of the TiO_2, and then subsequently the cleavage of the $\text{R-S}^+\text{=R'}$ bonds in methylene blue by a photogenerated hydroxyl radical (HO·) to form a sulfoxide. This reaction can be seen in equation 2.21.

$$\text{R-S}^+\text{=R'} + \text{HO}\cdot \rightarrow \text{R-}S(=\text{O})\text{-R'} + \text{H}^+ \tag{2.21}$$

Next, a second oxidative attack will occur on the sulfoxide, creating an unstable sulfone, which is then thought to dissociate, forming two separate benzenic rings and leads to a total loss of the blue colour of the original molecule. The complete reaction pathway can be seen in figure 2.6.

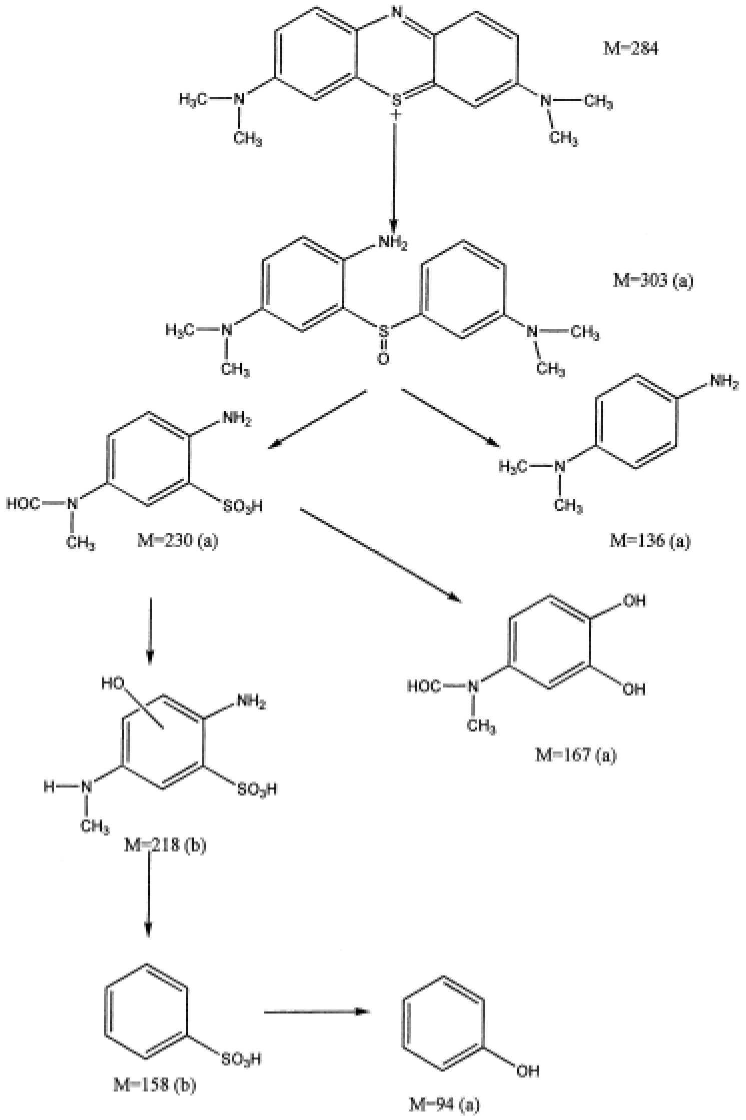

Figure 2.6. The reaction pathway of the photocatalytic degradation of methylene blue in the presence of TiO_2. Originally from Houas *et al.*[121]

Most of the work that assesses the photocatalytic activities of semiconductors using methylene blue, monitors the progress of the reaction via UV-vis absorption spectroscopy. Methylene blue absorbs most strongly at approximately 660 nm, from this a dye degradation study can be developed by irradiating with a light source (UV or solar simulator) and plotting the irradiation time versus the methylene blue absorption. This technique is also used for other dyes such as methyl orange and Resazurin.

2.4.2 Methyl Orange

Methyl orange is another common dye that is used in a similar way to methylene blue for the quantification of semiconductors' photocatalytic activity. The methyl orange molecule is attacked at the azo bond by photogenerated hydroxyl radicals, cleaving it and rendering the subsequent molecules colourless. The reaction pathway has been shown in figure 2.7.

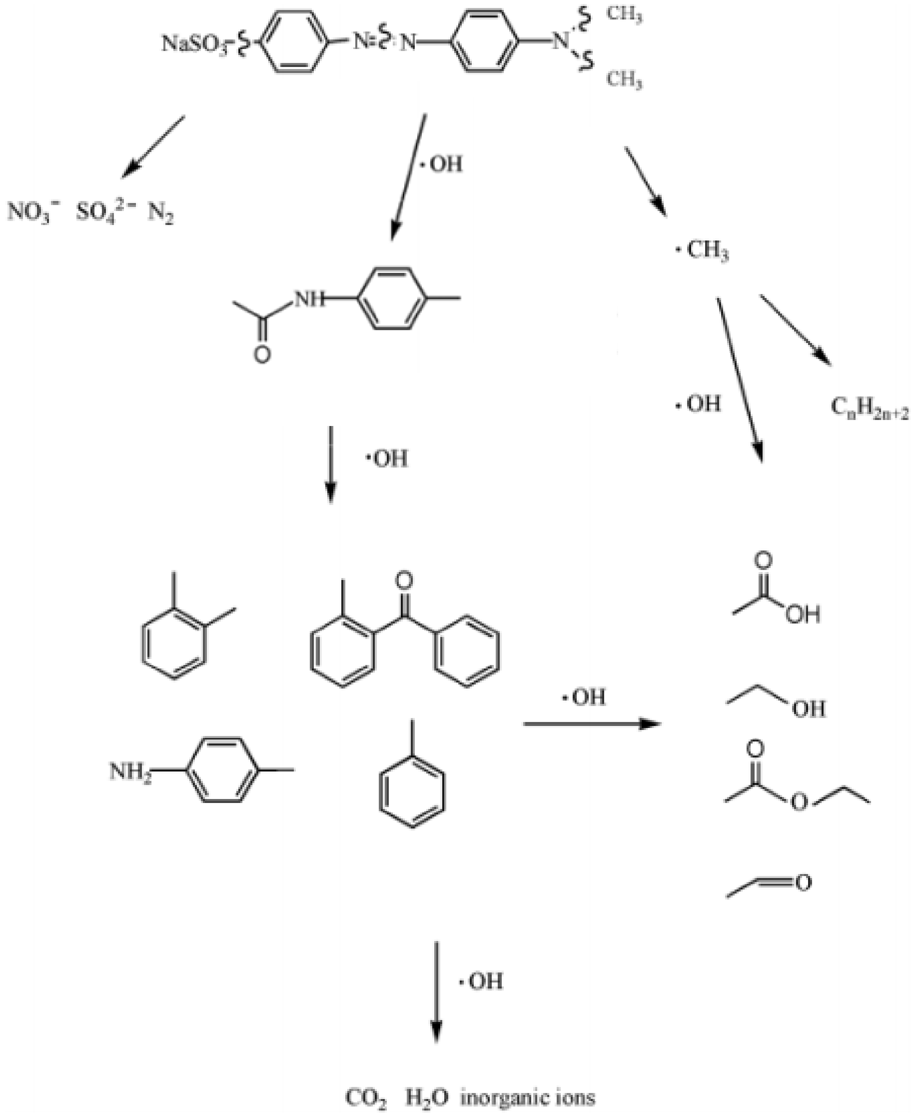

Figure 2.7. The reaction pathway of the photocatalytic degradation of methyl orange in the presence of TiO_2. Adapted from Du *et al.*[122]

2.4.3 Resazurin

Resazurin is a dye developed for the purpose of quick assessment of the photocatalytic activity of films. Whereas the methylene blue and methyl orange tests can take many hours to complete (due to the very thin layer of titania that is present in films), the Resazurin test gives a result in minutes. An aqueous solution of hydroxyethyl cellulose, glycerol, and Resazurin is usually spun or drop-coated onto the film's surface and dried in a low temperature oven or in air. The dye is initially blue in colour, but in the presence of a photocatalyst and UVA radiation, the dye rapidly changes to pink. Further irradiation will turn the Resazurin from pink to colourless.

In contrast to the methylene blue and methyl orange tests described above, the Resazurin test does not proceed via a photo-oxidative mechanism, but works by a photo-reductive mechanism in which photogenerated holes react with the glycerol (which acts as a sacrificial electron donor), and then the photogenerated electrons reduce the Resazurin dye molecules to a differently coloured molecule, known as Resorufin.

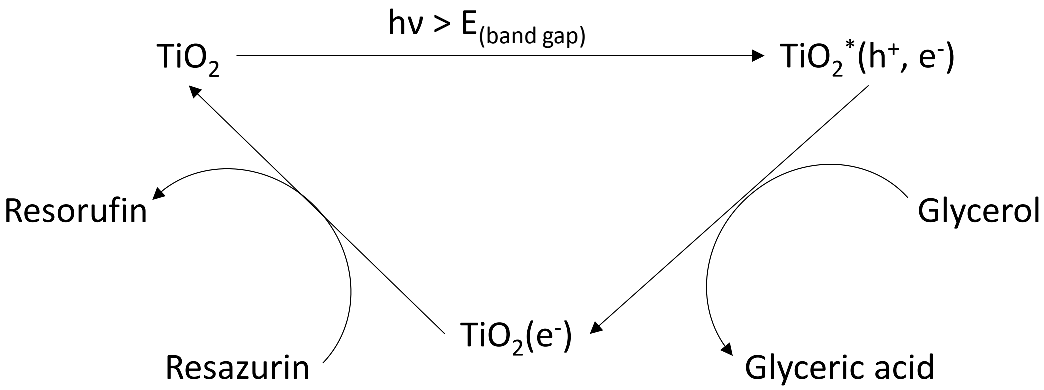

Figure 2.8. The reaction pathway of the photocatalytic degradation of Resazurin in the presence of TiO_2. Adapted from Mills *et al.*[123]

Chapter 3: Anatase and Rutile Quantification

3.1 Introduction

This chapter outlines the development of a novel technique for quantification of mixed phase systems using valence band X-ray photoelectron spectroscopy. The method requires no specialised equipment or data collection above what is standard on lab-based XPS instruments. The phase information obtained is limited to the surface, and is therefore complimentary to established bulk analysis techniques like XRD.

X-ray photoelectron spectroscopy is an analysis technique rooted in surface science but increasingly applied to materials science and solid-state chemistry. XPS using Al Kα incident radiation (E = 1486.6 eV) as is typical in a laboratory setting, is capable of ejecting electrons from the core atomic orbitals of all elements beyond He, and as such is a highly versatile technique for elemental quantification.[124,125] High resolution spectrometers can resolve the small binding energy shifts in peaks from core orbitals (such peaks are known as core lines) that arise due to changes in chemical environment of the element. Due to the low kinetic energy and therefore inelastic mean free path in a condensed phase, XPS interrogates only the near surface region of the sample.

Core line XPS can thus give surface specific information on composition, chemical state, as well as in some cases other properties such as plasma energy,[126] plasmon resonance,[127] heterojunction band offsets.[128,129] However, the energy of core orbitals usually cannot be interpreted in terms of the local and long range structure; core level XPS cannot usually be used to distinguish different structures of the same composition, for example crystalline polymorphs,[130] or amorphous vs crystalline phases, unless, as is the case for diamond and graphite, or carbon based polymers, differences in bonding lead to distinctive energy loss features around the core lines.[131-133] The valence electrons strongly interact with the neighbouring atoms, and their energy distribution will be influenced by the geometrical surroundings of each atom. Valence band spectra have been widely interpreted in terms of chemical modification of semiconductors,[134-136] for example, doping may introduce new filled electronic states at or around the valence band maximum (VBM) which can be detected by XPS or UPS. Alternatively, the offset between the VBM and the Fermi Level, referenced at the zero point on the binding energy scale can be measured to determine changes in n/p type doping or to establish the work function of the surface.[137] The spectral shape of the valence band is a reflection of the energy distribution of the density of filled states, which itself is strongly dependent on the arrangement in space of the constituent atoms, *i.e.* the structure. For this reason, valence band shapes can be obtained from a theoretical partial density of states calculated by, for example, Density Functional Theory (DFT) by applying experimental broadening and cross section weightings to each atomic orbital component.[126,138,139] While the valence band spectral shape contains phase information, this has so far not been exploited in quantitative phase analysis.

3.2 Method

TiO_2 powders were purchased from Sigma Aldrich and used as-received. Both rutile and anatase phases were obtained in different particle sizes:

325 mesh anatase powder, approximately equal to 45 micron particles (referred to as *bulk anatase*), 25 nm particle diameter anatase powder (*nano anatase*), 100 nm diameter rutile powder (*nano rutile*) and rutile powder with no specified particle size (*bulk rutile*).

Mixed phase samples were produced by mixing the desired weight ratio of the commercial powders, followed by thorough mixing by agitation of the powders.

Photocatalytic degradation of 7×10^{-5} M aqueous methyl orange was performed in a UVA light box (365 nm, 0.428 mW/cm^2). For each sample, 0.05 g of the powder was added to 12 mL of methyl orange solution. The powders were left to adsorb the solution overnight, then the UV-vis spectrum of the solution was recorded. The powder with solution was then magnetically stirred under UV conditions for 1 hour, separated by centrifuging at 3000 rpm for 10 minutes, and the UV-vis spectra recorded again.

3.3 Results

3.3.1 Characterisation

X-ray diffraction was carried out using a Cu Kα source on the as-received samples, and it was found that each commercial sample consisted only of the nominal phase within the detection limit of the technique.

The intention in this work is to examine series of samples with different relative surface areas of rutile and anatase. BET techniques were performed on the powders to show the surface area. Table 3.1 shows the results obtained. In both cases, for the bulk and nano powders, anatase had the higher surface area. The surface area of bulk a-TiO_2 is >12 times the surface area of bulk r-TiO_2, and nano a-TiO_2 has approximately 3 times the area of nano r-TiO_2.

TiO_2 Powder	**Surface Area [m^2/g]**
Anatase Bulk	12.29
Anatase Nano	76.94
Rutile Bulk	0.98
Rutile Nano	25.56

Table 3.1. Brunauer-Emmett-Teller (BET) derived surface areas of the bulk and nano powders used.

Mixed phase samples were produced by combining the phase pure TiO_2 powders together in the desired mass ratio, followed by agitation to ensure a homogeneous mixture. Three series of mixed phase TiO_2 samples were produced: bulk a-TiO_2 mixed with bulk r-TiO_2, nano a-TiO_2 mixed with bulk r-TiO_2, and bulk a-TiO_2 mixed with nano r-TiO_2.

Figure 3.1 shows a comparison of the diffraction patterns and the calculated phase fraction of anatase. As expected, the nano powders show broader peaks than the corresponding bulk powders because of their smaller diffracting domains. Phase fractions were determined by the reference intensity ratio (RIR) method using the procedure of Spurr and Myers outlined in the Enhanced Photoactivity section of Chapter 1.[44] Figure 3.1 also shows the XRD calculated phase fraction of a-TiO_2 against the nominal quantity. Whenever powders of differing particle sizes are mixed, there is the risk of a granular convection effect occurring whereby the distinct particle populations separate.[140] There is good agreement for all samples from each of the three series, indicating that the samples are sufficiently homogeneous and significant granular convection has not occurred. The adjusted R^2 values for all data sets were >0.99.

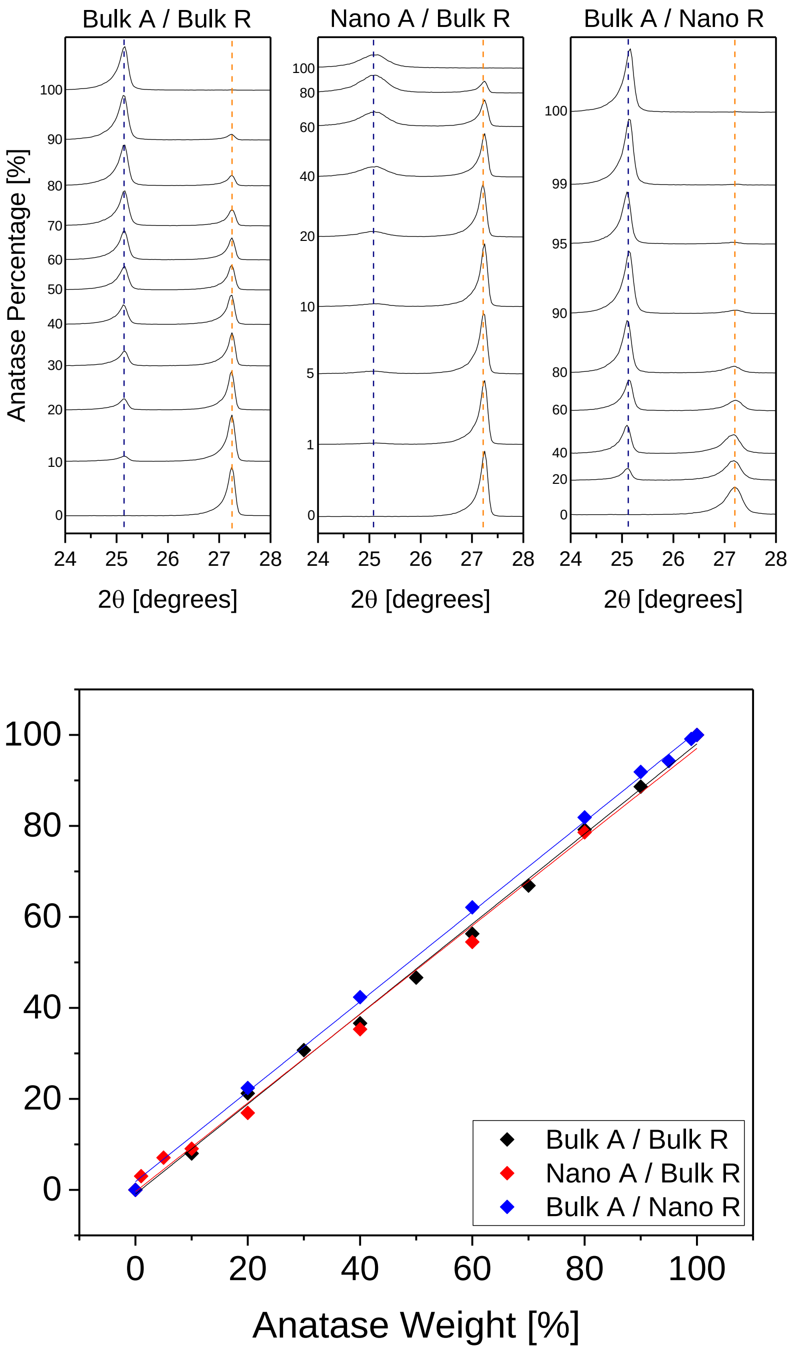

Figure 3.1. Top: X ray diffraction of all mixed TiO_2 bulk and nano powders. The peaks present at 25.10° (blue dash) can be attributed to

a-TiO_2 (101) and the peaks at 27.25° (orange dash) originate from the r-TiO_2 (110) plane. Bottom: Calculated anatase percentage from XRD against the nominal mass ratio of anatase.

3.3.2 Development of Novel VB XPS Technique

The VB spectra of bulk r-TiO_2 and bulk a-TiO_2 are shown in figure 3.2. A Shirley background, defined between binding energies of 0 and 12.0 eV has been subtracted for all spectra presented henceforth. The VB spectra from the two TiO_2 polymorphs have distinctive shapes.[141] In each case the valence band spectrum consists of two distinct maxima separated in binding energy by approximately 2.5 eV. However, in r-TiO_2, the lower binding energy spectral maximum is greater in height, whereas in a-TiO_2 the higher binding energy spectral maximum is considerably greater in height.

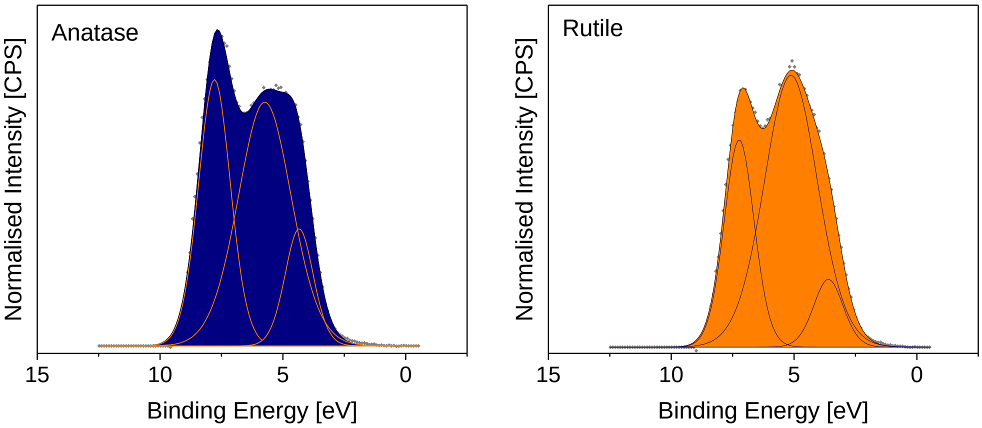

Figure 3.2. X-ray photoelectron valance band spectra of anatase and rutile TiO_2. Spectra have had a Shirley background subtracted, and were fitted with three components each.

The spectral shapes of bulk r-TiO_2 and bulk a-TiO_2 were modelled by fitting with three Gaussian-Lorentzian convolved peaks. No physical meaning is attached to the modelled components, they merely reproduce the VB spectral shape for use in the analysis presented below. The VB spectra from the nano powders were also taken and there was no discernible difference between the models, indicating that for these compounds and for the particle sizes studied, the VB spectral shape is not strongly influenced by the particle size.

Having obtained the VB spectral shapes for the pure phase compounds, the VB shapes for a-TiO_2 and r-TiO_2 were then used to fit the experimental VB spectra taken from mixed phase TiO_2 samples.

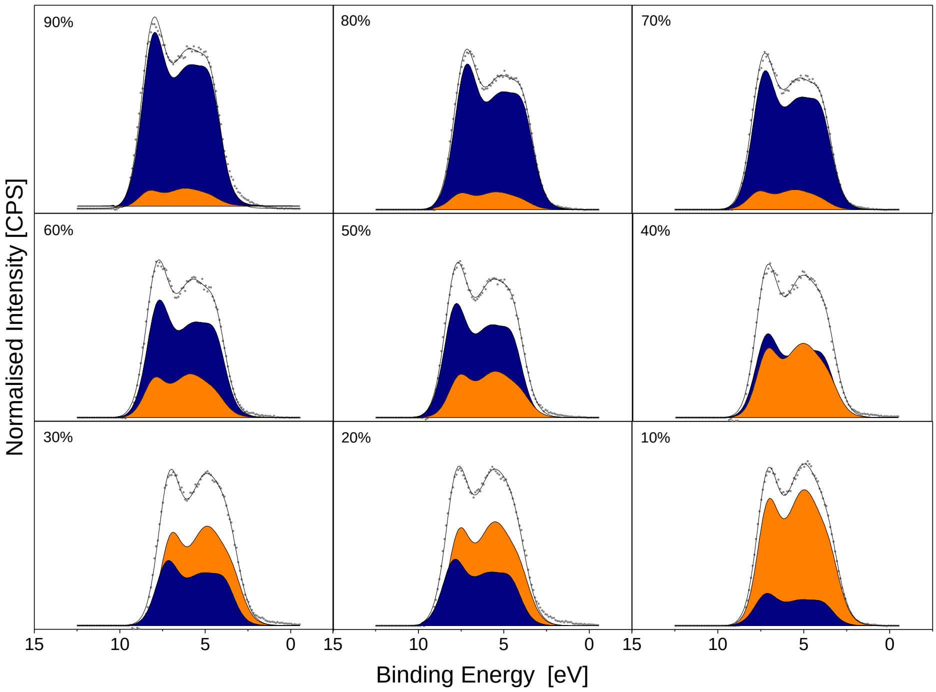

Figure 3.3. XPS valance band analysis of the mixed phase bulk powders using the modelled standards of anatase (blue) and rutile (orange). The grey points show the VB data obtained from XPS and the black line shows the sum of the two fitted models. The percentages shown refer to the anatase weight per sample.

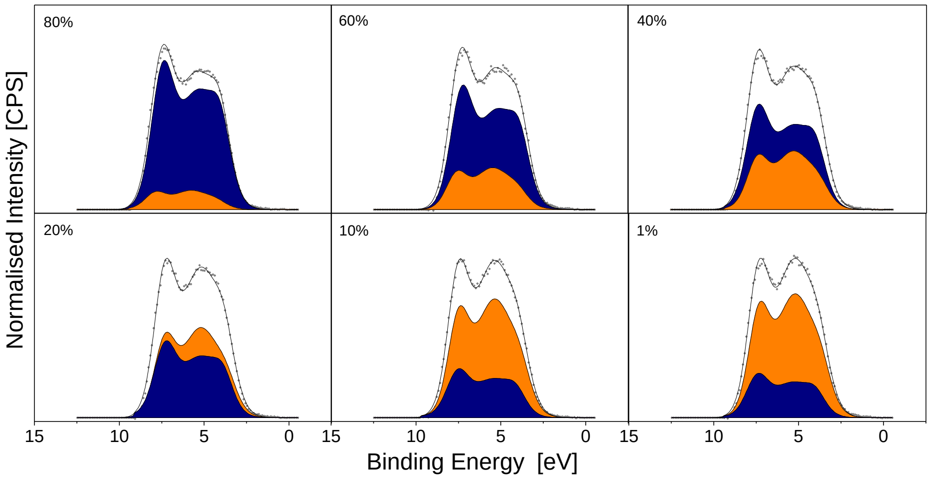

Figure 3.4. XPS valence band analysis of mixed nano a-TiO_2 (blue) and bulk r-TiO_2 (orange). The grey points show the VB data obtained from XPS and the black line shows the sum of the two fitted models. The percentages shown refer to the anatase weight per sample.

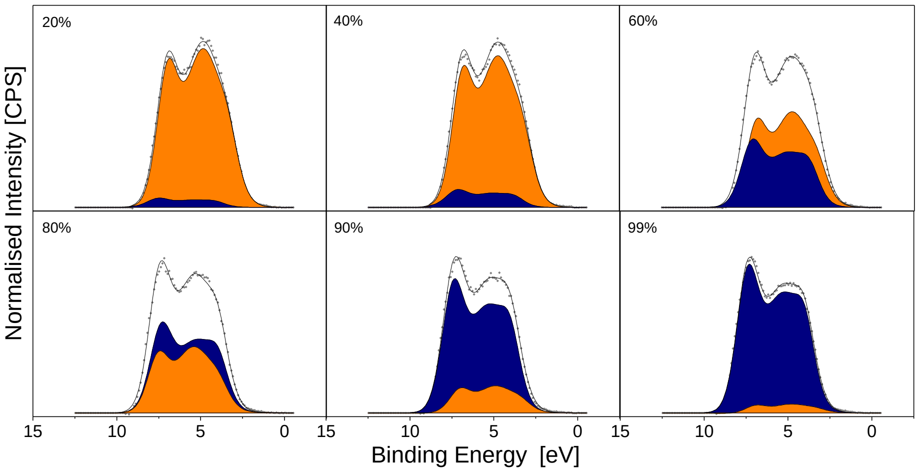

Figure 3.5. XPS valence band analysis of mixed bulk a-TiO_2 (blue) and nano r-TiO_2 (orange). The grey points show the VB data obtained from XPS and the black line shows the sum of the two fitted models. The percentages shown refer to the anatase weight per sample.

Figure 3.3 shows the VB spectra taken from the mixed phase TiO_2 bulk powders. Visually, the height ratio between the two maxima of the VB spectral shape can be seen to change monotonically between the end members. The spectra were fitted with a linear combination of the a-TiO_2 and r-TiO_2 VB spectral shapes determined from the pure compounds. For all fittings, the shape of the two models were constrained, only the relative positions and intensities were allowed to change. The same treatment was also carried out for mixed phase nano and bulk powders (figures 3.4 and 3.5). In each case a good agreement between model and experimental data was found.

The intensity of a photoemission peak is proportional to the concentration of the emitting species, the attenuation of the photoelectron due to the depth of the emitting species, and the photoionisation cross section, itself a function of the orbital and the photon energy. Hence the intensity of a valence band spectrum will depend upon its orbital makeup. Since the TiO_2 phases have the same chemical composition it is assumed here that the valence band spectrum, has essentially the same orbital make-up (in this case consisting primarily of O 2p with some Ti 3d contribution) and thus the same overall photoionisation cross section. Hence the intensity of the fitted anatase component of a VB spectrum can be directly related to the amount of anatase present within the sampling depth of the measurement. In this way, it can be proposed that the XPS VB can be used to extract quantitative phase information.

The amount of anatase determined by fitting the XPS VB spectrum described above was compared with the nominal mass percentage of anatase in the mixed powders (figure 3.6). As can be seen, each of the three series presents a different relationship between XPS VB quantified anatase proportion and the nominal proportion. For the sample series containing nano-scale rutile, *i.e.* with a high surface area of rutile particles, the amount of anatase derived from the XPS VB is lower than the nominal amount. For the other two series, *i.e.* bulk a-TiO_2/bulk r-TiO_2 and nano a-TiO_2/bulk r-TiO_2, the proportion of anatase determined by XPS VB is above the nominal amount. It is noteworthy that for a particular nominal mass ratio, the XPS derived anatase fraction increases with the increasing relative BET surface area of the anatase phase (Table 3.1). For example, for samples with a nominal mass ratio of 40% anatase, in the series with nanoscale anatase and bulk rutile, XPS measures 63% anatase. In the series with bulk anatase and bulk rutile, XPS measures 52% anatase, and in the series with bulk anatase and nano rutile, XPS measures only 10% anatase. The remainder of all three series follow the same pattern. These results suggest that XPS VB spectroscopy affords a surface phase measurement in this TiO_2 system.

Using Al Kα radiation the sampling depth of XPS is typically 5-10 nm. Therefore it is to be expected that the phase fraction determined from XPS VBs will be representative of surface phase rather than the overall or bulk phase which is typically determined by standard XRD geometries. That is, XPS phase quantification will be scaled by the fraction of a phase at the surface of the sample, just as XPS elemental composition is scaled by the proportion of an element at the surface of the sample.

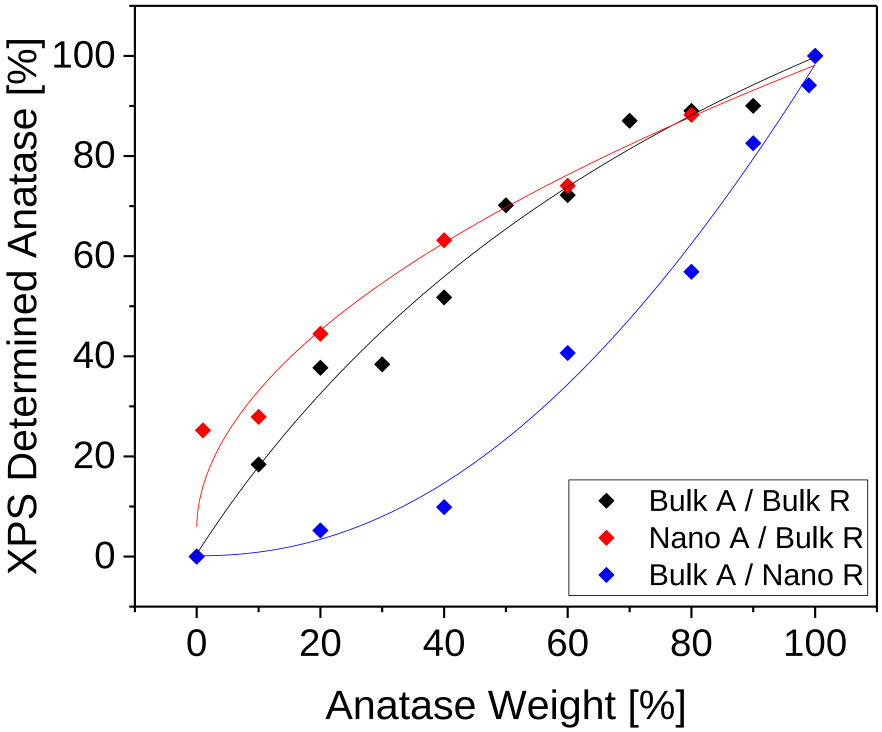

Figure 3.6. The contribution of the anatase standard in the valence band of all mixed powders. All data sets fitted with a logistic regression.

To confirm the practical applications of this technique, an industrial photocatalytic powder known as Degussa (Evonik) P25 was examined using the same VB XPS process. Figure 3.7 shows the XRD is similar to those seen previously. The broadness of the peaks implies a fine (nano) powder, and using the relative intensity ratio (RIR) method as before, the composition can be determined at 90.99% anatase and 9.01% rutile.

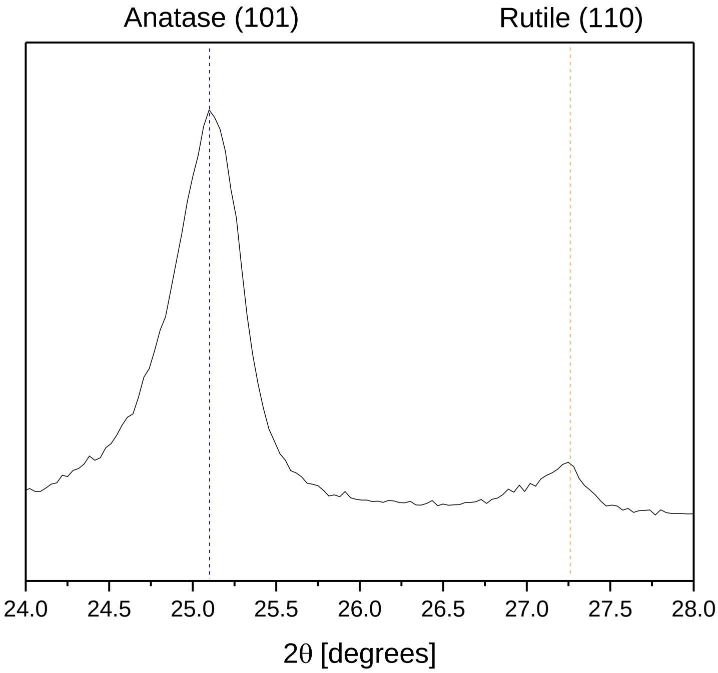

Figure 3.7. X-ray diffraction of P25 TiO_2 powder. The peaks present at 25.10° (blue dash) can be attributed to a-TiO_2 (101) and the peaks at 27.25° (orange dash) originate from the r-TiO_2 (110) plane.[142]

Figure 3.8 shows the valance band shape of the P25 TiO_2. Fitting with the standard models reveals a composition of 84.83% anatase and 15.17% rutile. This implies that the surface phase of the powder contains a higher proportion of rutile than the bulk.

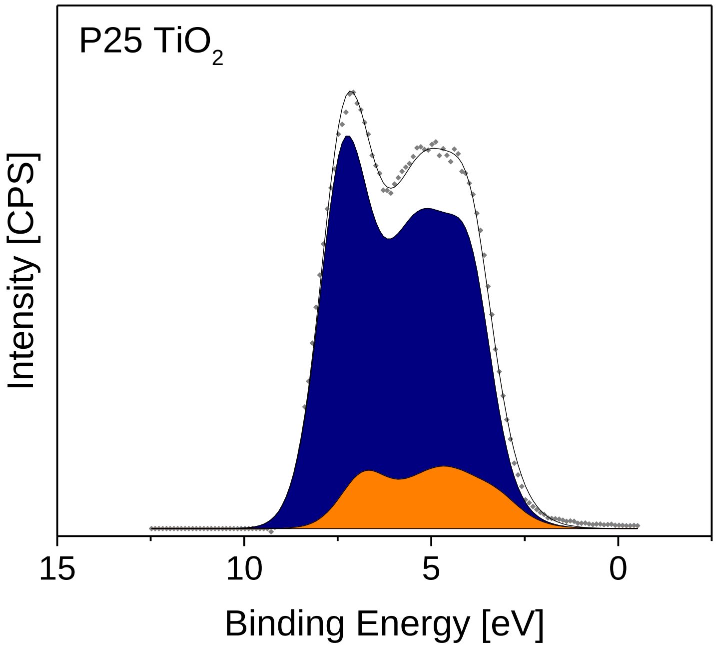

Figure 3.8. The valence band XPS of Degussa P25. a-TiO$_2$ (blue) and r-TiO$_2$ (orange) are compositionally found at 84.83% to 15.17%.

3.3.3 Photocatalysis

To assess whether the surface phase determined by XPS VB analysis is related to functional properties of the materials, photocatalysis experiments were conducted using the mixed phase powders described above. The initial rate of aqueous methyl orange degradation under UV light and in the presence of the catalyst in suspension was measured. The spectra of the dye solutions before and after degradation can be seen in figures 3.9-3.11.

Anatase is known to be the more photoactive phase, and for each series of mixtures, the pure anatase sample gave the greatest photocatalytic activity. It is known that mixed phase anatase-rutile systems can show enhanced photoactivity over either of the end members.[40,143] This was not observed here, but such enhancement is thought to require chemically bonded rutile-anatase heterojunctions rather than physical mixtures of distinct populations of phase pure particles.[144,145]

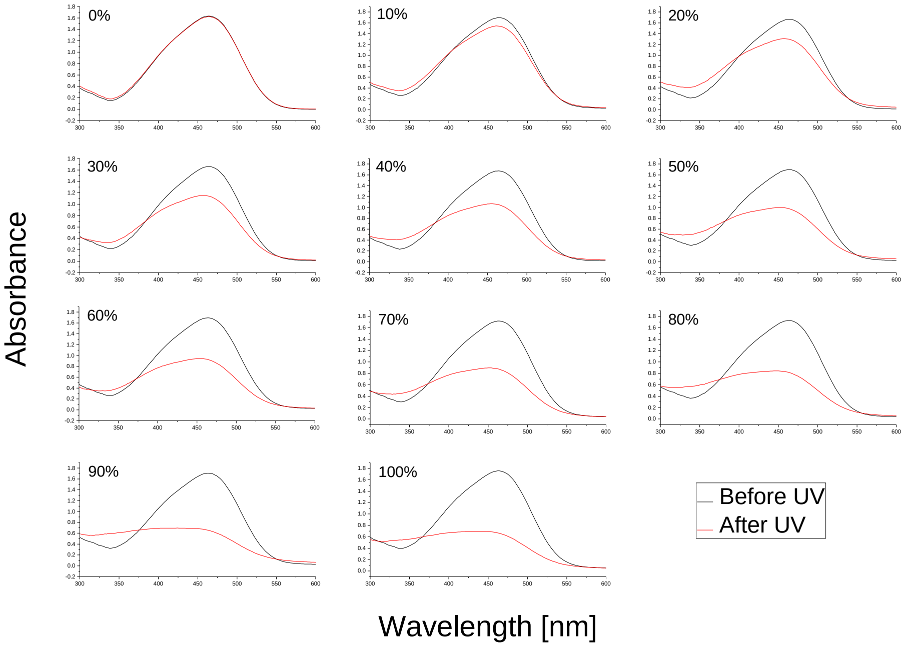

Figure 3.9. The UV-vis spectra of the absorbance of methyl orange by bulk a-TiO_2 and bulk r-TiO_2 mixed powders before and after UV irradiation. The percentage shows the amount (by weight) of anatase present.

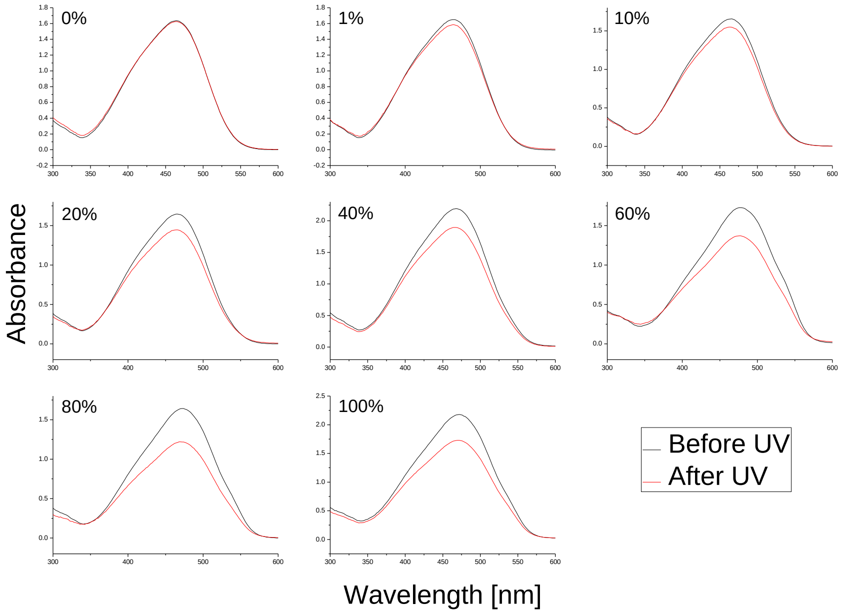

Figure 3.10. The UV-vis spectra of the absorbance of methyl orange by nano a-TiO_2 and bulk r-TiO_2 mixed powders before and after UV irradiation. The percentage shows the amount (by weight) of anatase present.

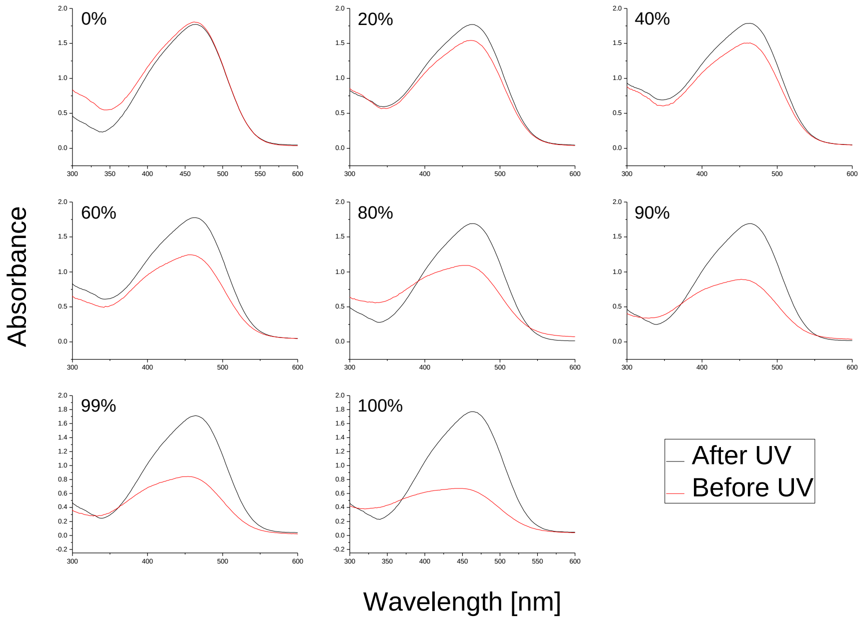

Figure 3.11. The UV-vis spectra of the absorbance of methyl orange by bulk a-TiO_2 and nano r-TiO_2 mixed powders before and after UV irradiation. The percentage shows the amount (by weight) of anatase present.

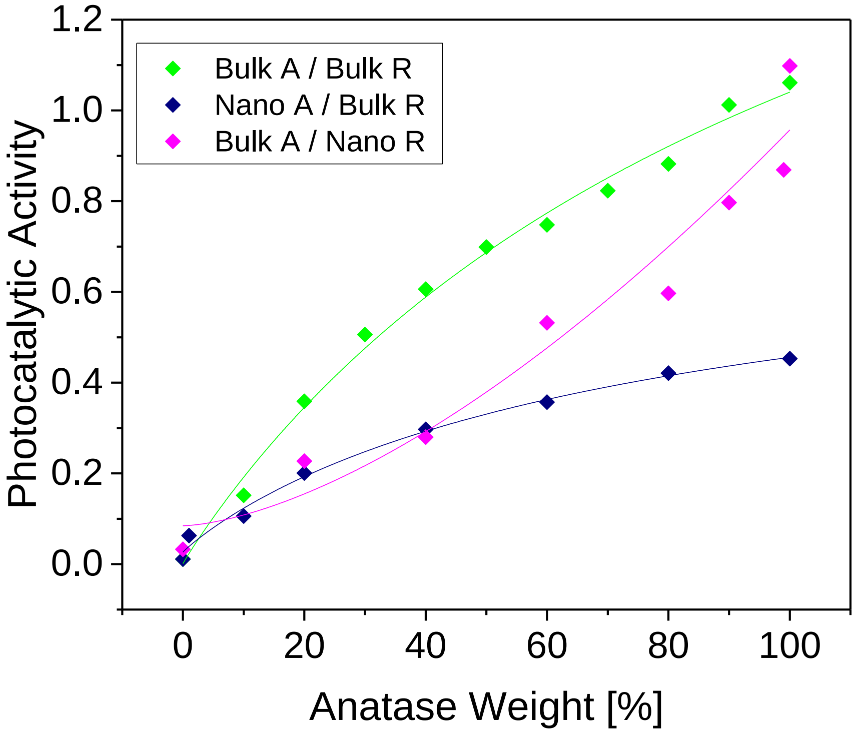

Figure 3.12. The absolute photocatalytic activity of the mixed phase powders determined by the degradation of methyl orange under UV light. All data sets fitted with a logistic regression.

Figure 3.12 shows the differences in in methyl orange absorbance before and after UV irradiation for the mixed phase powders, giving the absolute photocatalytic values. Somewhat surprisingly, the mixed powders that contained nano anatase proved to be less efficient photocatalysts than the bulk anatase powders. A possible explanation could be that the nanoparticles clumped together as when they were added to the dye solution, causing ineffective adsorption on their surface. But as this investigation is concerned with the photocatalytic trend rather than the absolute values of the photocatalytic activity the results can be justifiably normalised.

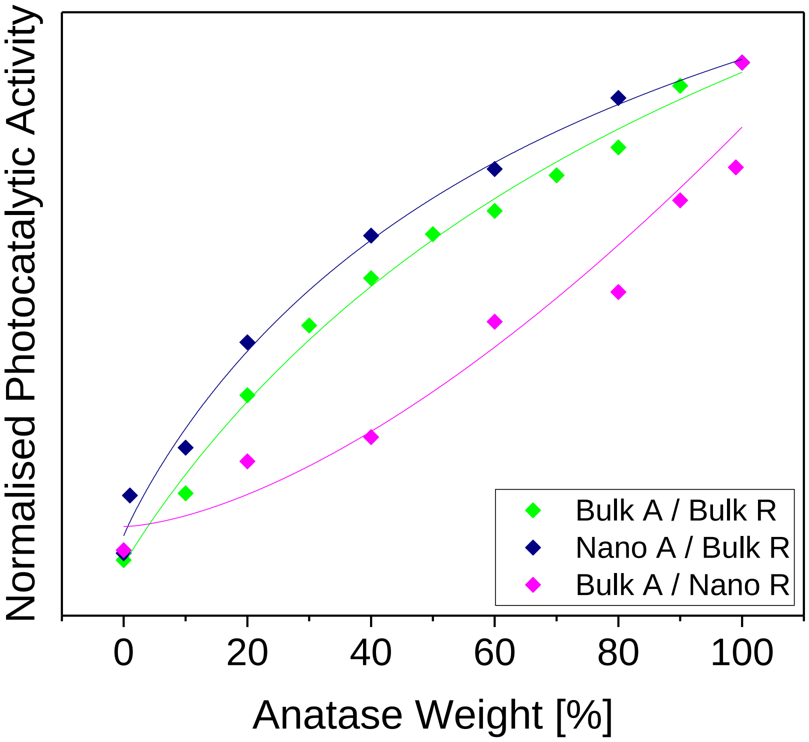

Figure 3.13. The normalised photocatalytic activity of the mixed phase powders determined by the degradation of methyl orange under UV light. Data sets justifiably normalised to represent the photocatalytic trend rather than the absolute photocatalytic activity. All data sets fitted with a logistic regression.

The photocatalytic rate for the remainder of the series were normalised to the value for pure anatase. The results plotted against the nominal phase composition are shown in figure 3.13. There was a significant difference between the photocatalytic activities of the three different series at a given composition. However, the photocatalytic activity has a linear relationship (R^2=0.97) with the surface anatase phase, determined from XPS VB analysis (figure 3.14).

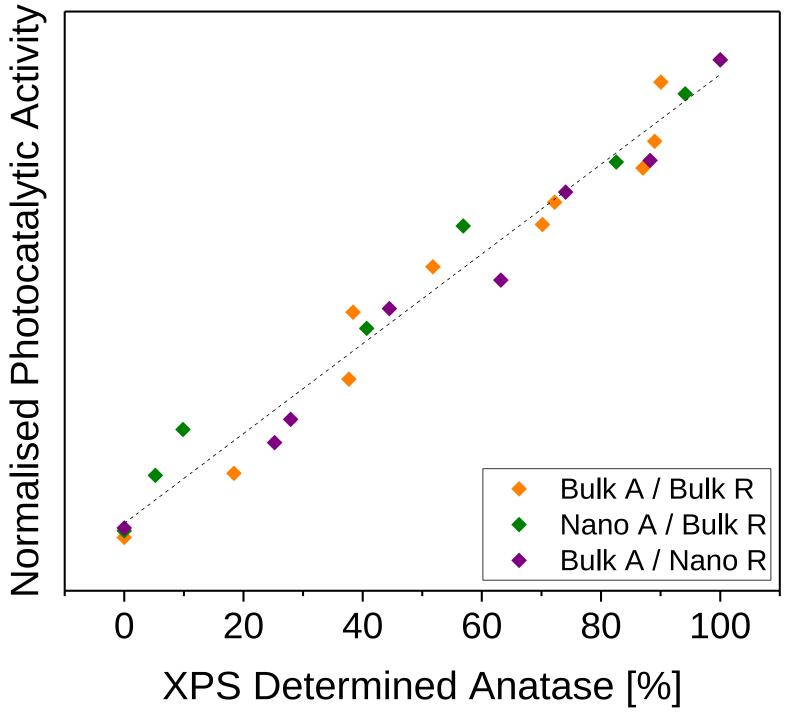

Figure 3.14. The relationship between the XPS calculated amount of anatase and the photocatalytic activity of the mixed-phase powders. Linear regression adjusted R^2 of 0.97.

The results from the BET surface area measurements were analysed as a comparison to the linear relationship of the XPS calculated amount of anatase and the photocatalytic activity. Figure 3.15 shows that each of the three series presents a different relationship between the BET quantified anatase proportion and the nominal proportion. In the same way as with the VB XPS analysis, the sample series containing nano-scale rutile, *i.e.* with a high surface area of rutile particles, the amount of anatase derived from the BET is lower than the nominal amount. Again, for the other two series, i.e. bulk a-TiO_2/bulk r-TiO_2 and nano a-TiO_2/bulk r-TiO_2, the proportion of anatase determined by BET is above the nominal amount to a much greater extent than with VB XPS.

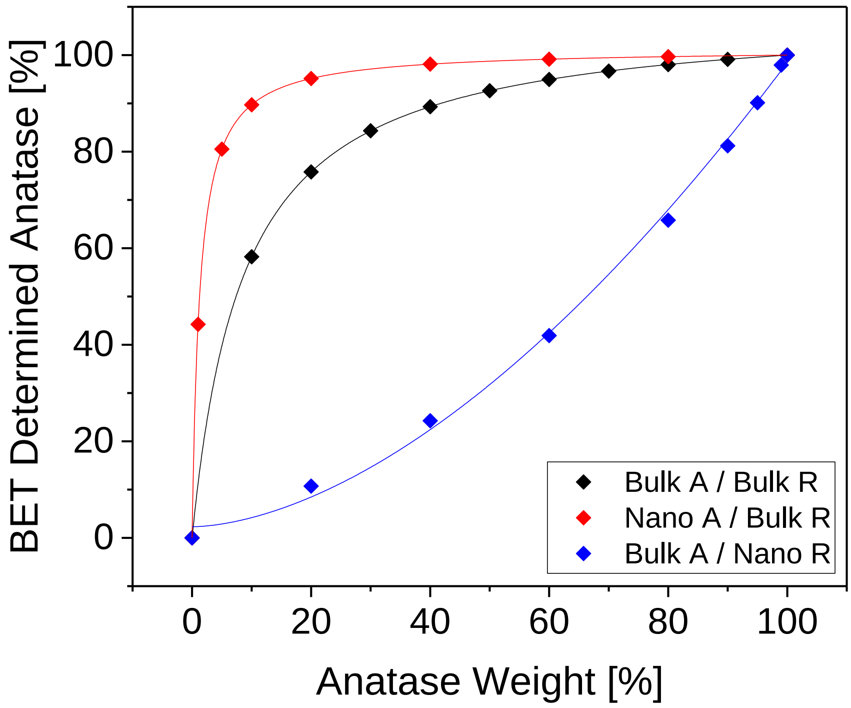

Figure 3.15. Calculated anatase percentage from BET against the nominal mass ratio of anatase.

These BET results plotted against the nominal phase composition are shown in figure 3.16. Like VB XPS, there was a significant difference between the photocatalytic activities of the three different series at a given composition. However, unlike VB XPS, the photocatalytic activity does not have a linear relationship (R^2=0.62) with the surface anatase, determined from BET analysis. These results again suggest that XPS VB spectroscopy affords an accurate surface phase measurement in this TiO_2 system.

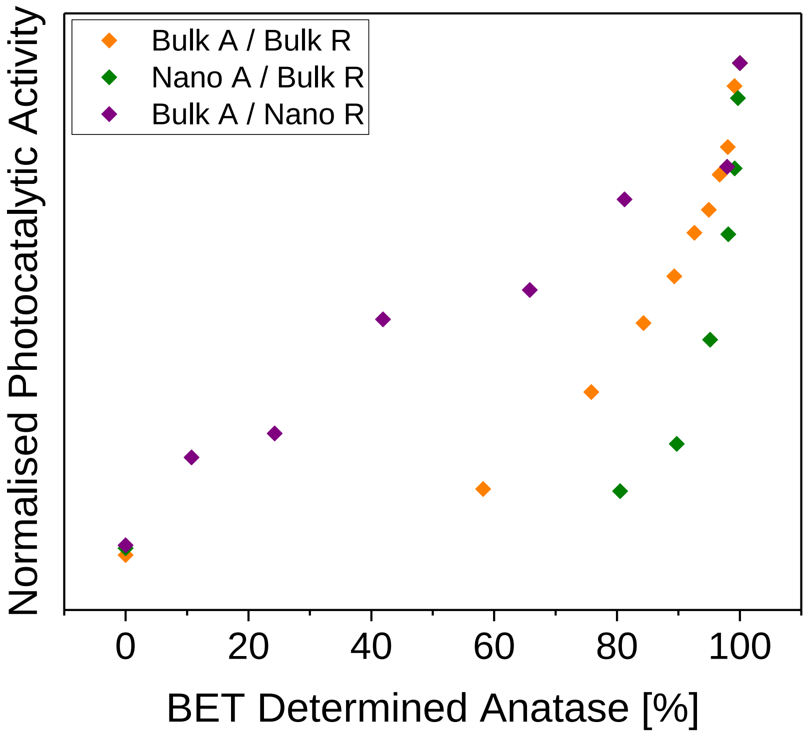

Figure 3.16. The relationship between the BET calculated amount of anatase and the photocatalytic activity of the mixed-phase powders. Linear regression adjusted R^2 of 0.62163.

3.4 Conclusion

This chapter presented a method to quantitatively determine surface phase composition by valence band XPS analysis. For the TiO_2 rutile/anatase system, the measured surface phase correlates linearly to photocatalytic performance, whereas XRD phase quantification does not, since XRD measures the bulk or total phase composition rather than the surface phase. This method has the potential to work with any mixed or multi-phase system, including amorphous or poorly crystalline phases which are challenging to quantify with traditional methods. The phase information that can be obtained in this way is surface limited, and significant differences are seen when anatase and rutile samples with different relative surface areas are used.

Chapter 4: Rutile to Anatase Transformation

4.1 Introduction

As has been described in Chapter 1, there has been considerable effort to understand the effect of the microscopic arrangement of nitrogen dopants – i.e. whether they are substitutional or interstitial. However, a factor far less commonly investigated is the macroscopic arrangement of the dopants, or the location of the nitrogen dopants whether homogeneously distributed throughout the sample, segregated to the surface or to the bulk. It is largely unknown how synthesis and processing methods affect the macroscopic dopant distribution. The physical location of the dopants may play an important role in photocatalysis, not least in affecting the transport of photoexcited charge carriers. To understand how the nitrogen is distributed when incorporated into the TiO_2 lattice will give a clearer indication of how photocatalysis occurs and what role nitrogen plays, as solid state catalysis is dependent on interfaces between compounds.

This chapter is a study of the nitrogen dopant distribution in epitaxial thin films of anatase and rutile in order to ascertain the effect of synthesis and processing conditions on dopant distribution. It will show that sample processing strongly affects the macroscopic dopant distribution in the materials studied. Furthermore, it will show that in rutile (110) oriented films, the incorporation of nitrogen induces a reverse rutile-to-anatase phase transition at high temperature, which is believed to have not been observed previously. This reverse phase transition occurs through two different methods of nitrogen doping, and may explain some of the enhanced photoactivity seen in nitrogen doped materials by phase transformation rather than direct visible light absorption.

4.2 Method

Single crystal substrates, Al_2O_3 (0001), $SrTiO_3$ (001) and $LaAlO_3$ (001) crystals were purchased from PI-KEM Ltd. Substrates were 10x10x1 mm^3 in size and were epi-polished on both sides by the manufacturer. Prior to use, substrates were cleaned by ultrasonication in acetone followed by isopropanol, and were dried under a stream of nitrogen gas.

The solution phase route to TiO_2 films is adapted from Powell *et al.*[146] Acetylacetone (0.025 mol: 2.52 g) was added to butan-1-ol (32 cm^3), followed by addition of titanium *n*-butoxide (0.05 mol: 17.50 g) and left to stir vigorously for 1 hour at room temperature. Isopropanol (0.15 mol: 9.05 g) dissolved in distilled water (3.64 cm^3) was added and the solution left to stir for 1 hour at room temperature. Finally acetonitrile (0.04 mol: 1.66 g) was added and the solution was left to stir for a further 1 hour at room temperature.

This solution was used to deposit nominally undoped TiO_2 films. To deposit nitrogen doped films, tetramethylethylenediamine (TMEDA, 0.0129 mol: 1.5g) was added to the sol and left to stir for 1 hour at room temperature. In both cases (undoped TiO_2 sol or nitrogen doped TiO_2 sol) the solution was then sealed and left overnight to age.

After aging, the solution was deposited onto the desired single crystal substrate via dynamic dispense at 1000 rpm, then spun at 3000 rpm for 30 seconds. These depositions steps were repeated 5 times without interlayer annealing for each film. After deposition, the thin film samples were annealed in air at 800 °C for 2 hours to effect crystallisation. For post-annealing nitrogen doping, nominally undoped TiO_2 epitaxial thin films on single crystal substrates were heated in a tube furnace under ammonolysis conditions (675 °C, flowing anhydrous ammonia gas) for 3 hours. The flow rate of the ammonia was 600 sccm and the samples were heated up and down under flowing nitrogen with a ramp rate of 10 °C / minute. Once cooled to room temperature, samples were handled and stored in air.

4.3 Results

4.3.1 Characterisation

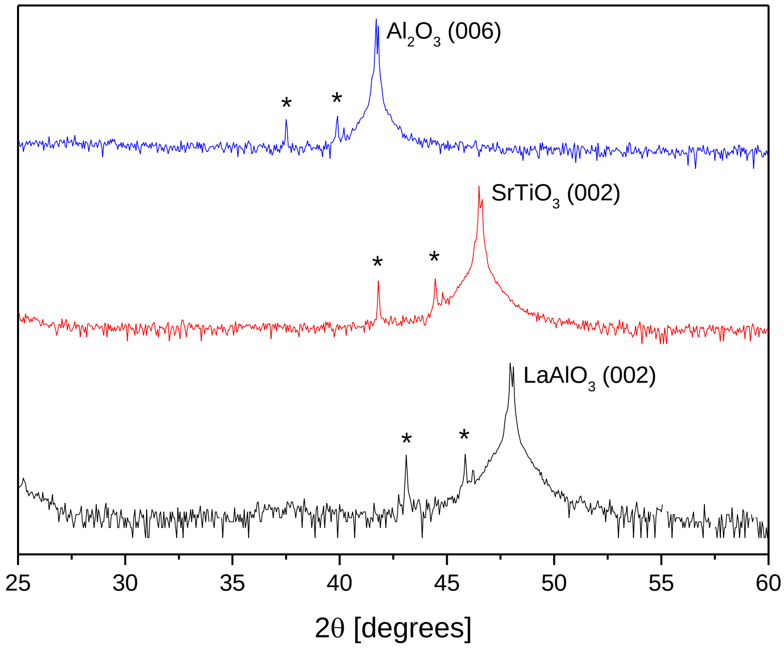

Figure 4.1. XRD of Al_2O_3 (0001), $SrTiO_3$ (001), and $LaAlO_3$ (001) substrates. The intensity ordinate is on a log scale, with separate scans offset for clarity. Peaks marked with an asterisk originate from the

substrate and are an instrumental artefact due to additional wavelengths present in the X-ray radiation.

Figure 4.1 shows the XRD of the blank single crystal substrates Al_2O_3 (0001), $SrTiO_3$ (STO) (001), and $LaAlO_3$ (LAO) (001). The intensity ordinate has been plotted on a log scale. Cu k-alpha radiation gave the (006) peak of Al_2O_3 at 2θ=41.75°, the (001) peak of STO at 2θ=46.60°, and the peak of LAO at 2θ=48.00°. These positions for all substrates are in good agreement with the results observed by others.[147-149] The peaks marked with an asterisk can be attributed to the fact that the diffractometer is not completely monochromated and arise from other wavelengths (Cu Kβ etc.).

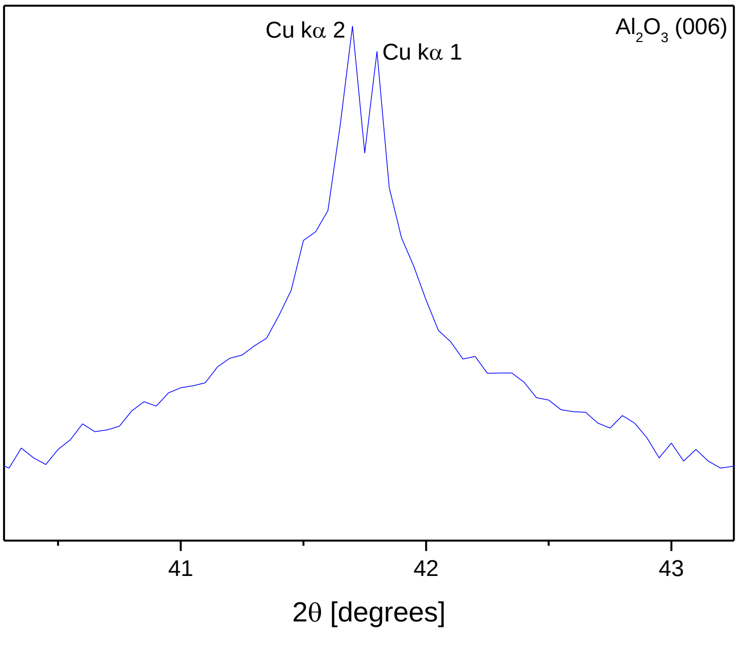

Figure 4.2. XRD of Al_2O_3 (0001) showing splitting due to $K\alpha_1$ and $K\alpha_2$ wavelengths.

On closer inspection the substrate peaks appear to be split (figure 4.2). This can again be attributed to additional wavelengths in the X-ray beam and with a logarithmic scale, it is possible to see the presence of these Kα$_2$ wavelengths.

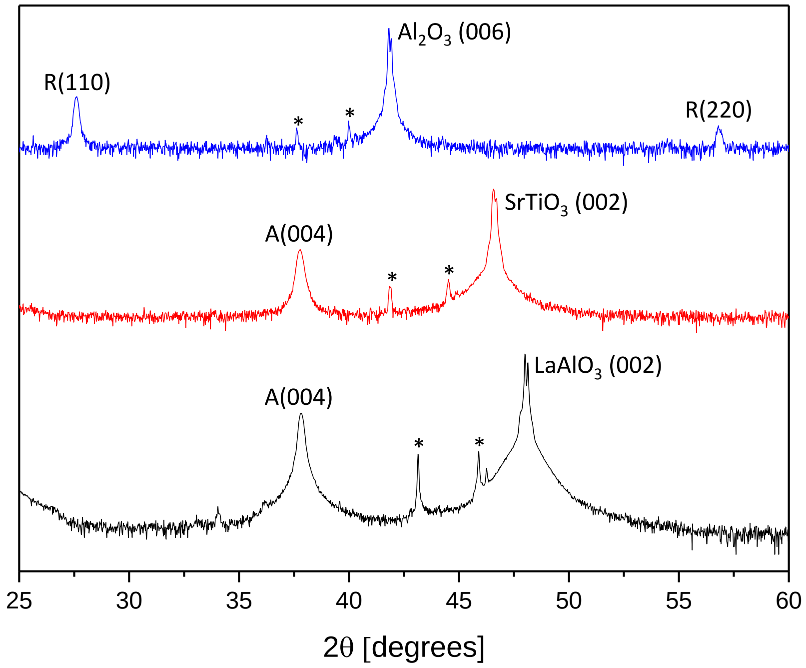

Figure 4.3. XRD of epitaxial rutile (110) and (220) TiO$_2$ grown on Al$_2$O$_3$ (0001) and anatase (004) TiO$_2$ grown on SrTiO$_3$ (001) and LaAlO$_3$ (001). The intensity ordinate is on a log scale, with separate scans offset for clarity. Peaks marked with an asterisk originate from the substrate and are an instrumental artefact due to additional wavelengths present in the X-ray radiation.

Epitaxial films of undoped TiO$_2$ were produced on Al$_2$O$_3$ (0001), SrTiO$_3$ (STO) (001), and LaAlO$_3$ (LAO) (001) oriented substrates (figure 4.3). The perovskite structured substrates STO and LAO were found to template a-TiO$_2$ as observed by others.[150-152] Films grown on STO and LAO showed only one diffraction peak from the film, assigned as a-TiO$_2$ (004), consistent with (001) orientated growth of the anatase phase. The peaks originating from the single crystal substrates were used as internal references to calibrate the 2θ range for calculation of the thin film lattice parameters. The a-TiO_2 (004) peak from the film grown on LAO was measured at 2θ=37.90°, giving d_{004} = 2.374 Å corresponding to c = 9.496 Å, very close to the c parameter expected in bulk a-TiO_2 of 9.515 Å. The coincidence of the epitaxial film out-of-plane lattice parameter with the bulk lattice parameter indicates that there is little epitaxial strain in this film. For a-TiO_2 films deposited on STO, the a-TiO_2 (004) diffraction peak appeared at 2θ=37.64° giving d_{004} = 2.390 Å corresponding to c = 9.560 Å, slightly larger than the bulk parameter. This is unexpected, as previously a-TiO_2 films on STO (001) have shown slightly reduced *c* parameters compared to the bulk, due to tensile strain.[153]

Growth of TiO_2 on Al_2O_3 (0001) crystals was found to template r-TiO_2 growth; only the r-TiO_2 (110) and (220) diffraction peaks were present in the angular range measured, indicating a (110) orientation of the deposited film. The r-TiO_2 (110) peak appeared at 2θ=27.47°, giving d_{110} = 3.247 Å corresponding to a = 4.592 Å, matching the reported bulk r-TiO_2 lattice parameter of a = 4.594 Å. Thus the rutile phase appears unstrained, although the absence of any other r-TiO_2 peaks indicates that the film is templated by the substrate; for example the r-TiO_2 (211) peak, expected at 2θ=54.4° with intensity 51% of the (110) peak, is absent in the XRD pattern from the film. The stabilisation of the r-TiO_2 (110) orientation by Al_2O_3 (0001) is unexpected, however. Several studies of TiO_2 grown using physical vapour deposition techniques report rutile (001) being produced epitaxially on Al_2O_3 (0001),[154-157] to the best of our knowledge this is the first reported case of epitaxial r-TiO_2 (110) on this Al_2O_3 surface.

X-ray photoelectron spectroscopy of the TiO_2 films on different substrates confirmed the expected surface composition of Ti, O and carbon contamination. Valence band (VB) scans were carried out and are shown in figure 4.4. As seen in the previous chapter, the VB spectrum of r-TiO_2 and a-TiO_2 have distinctive shapes, where VB spectra from commercial powders of each phase are shown. Both phases consist of a VB spectrum with two distinct maxima separated in binding energy by approximately 2.5 eV. However, in r-TiO_2, the two maxima are approximately equal in height, whereas in a-TiO_2 the larger binding energy maximum is considerably greater in height. Thus these two polymorphs of TiO_2 can be distinguished by comparing the VB spectra. The VB spectra from the epitaxial films on LAO, STO and Al_2O_3 can be seen to follow the expected pattern. The films on LAO and STO have VB spectra closely resembling the a-TiO_2 standard, whilst the film on Al_2O_3 has a VB spectrum closely resembling r-TiO_2. This supports the XRD analysis, and further confirms that the surface of these materials has the same crystal structure as the bulk.

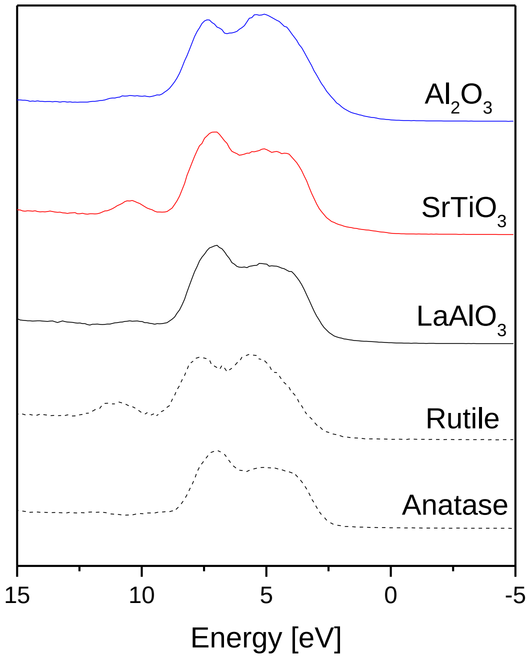

Figure 4.4. Valence band spectrum of epitaxial rutile (110) TiO_2 films grown on Al_2O_3 (0001) and anatase (004) TiO_2 grown on $SrTiO_3$ (001) and $LaAlO_3$ (001) compared with the standard valance bands of rutile and anatase.

Figure 4.5 reveals the approximate thicknesses of the films. For the substrates Al_2O_3 and $LaAlO_3$, the Al 2p region was used as the indicator for reaching the substrate, whereas for $SrTiO_3$, the Sr 3d region was used. The Ar ion gun of the XPS has an etching rate of approximately 1 nm s^{-1} and heat maps show bright spots of the substrate can be seen to appear after 500 seconds at approximately 75 eV for Al_2O_3 and LAO and 135 eV for STO. This gives an estimation of the thickness as 500 nm for all films.

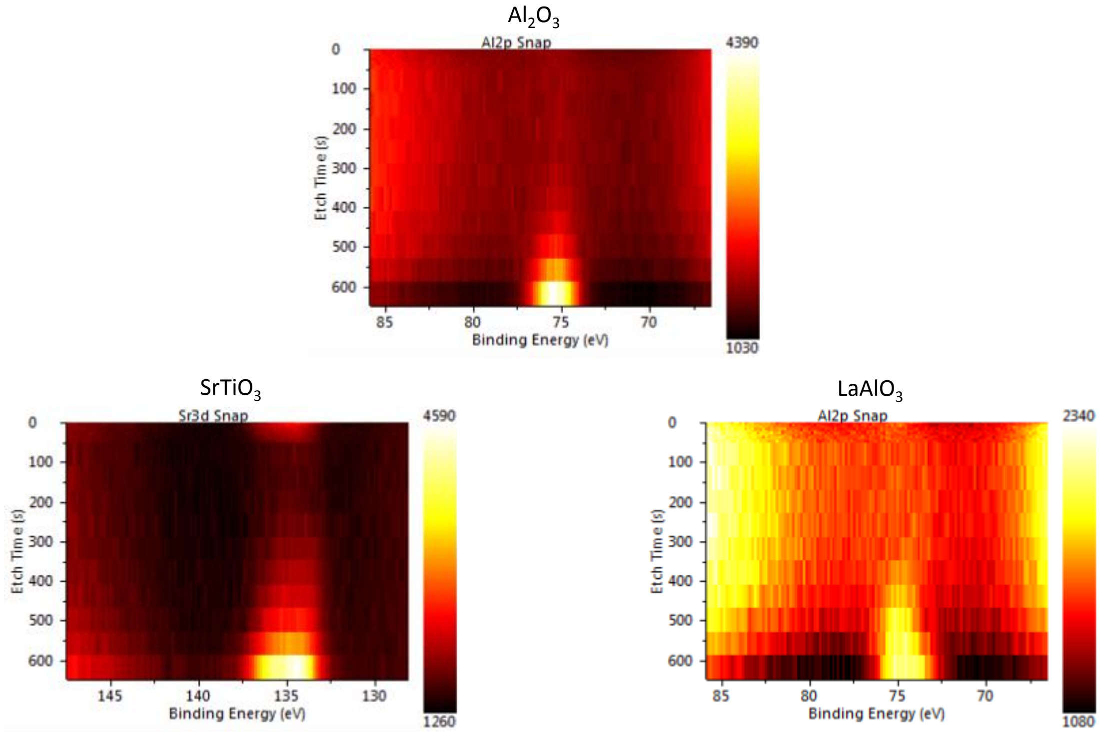

Figure 4.5. XPS depth profiles of TiO_2 films on Al_2O_3, $SrTiO_3$, and $LaAlO_3$ displayed as a heat map. For films grown on Al_2O_3 the Al 2p region is shown, for $SrTiO_3$ the Sr 3d region is shown, and for $LaAlO_3$ the Al 2p region is shown. These regions are used to identify the depth of the film-substrate interface and hence the thickness of the films.

4.3.2 Nitrogen Doping by Ammonolysis

After deposition, each epitaxial TiO_2 film described in the previous section was heated under flowing ammonia at 1 sccm at 675°C for 1.5 and 3.0 hours to induce nitrogen doping. XRD showed the epitaxial nature of the anatase films on STO and LAO remained unchanged, with lattice parameters identical before and after ammonolysis. After exposure to these ammonolysis conditions for 1.5 hours, the r-TiO_2 film on Al_2O_3 (0001) also showed unchanged XRD patterns (figure 4.6). However, after 3 hours the diffraction peaks corresponding to a-TiO_2 emerged at

2θ=25.30° and 2θ=48.05° corresponding to a-TiO_2 (101) and (200) reflections respectively. There are examples of nitrogen doping TiO_2 promoting anatase formation or raising the anatase to rutile transition temperature,[158-160] but to our knowledge no previous report of interconversion of rutile to anatase at high temperature exists.

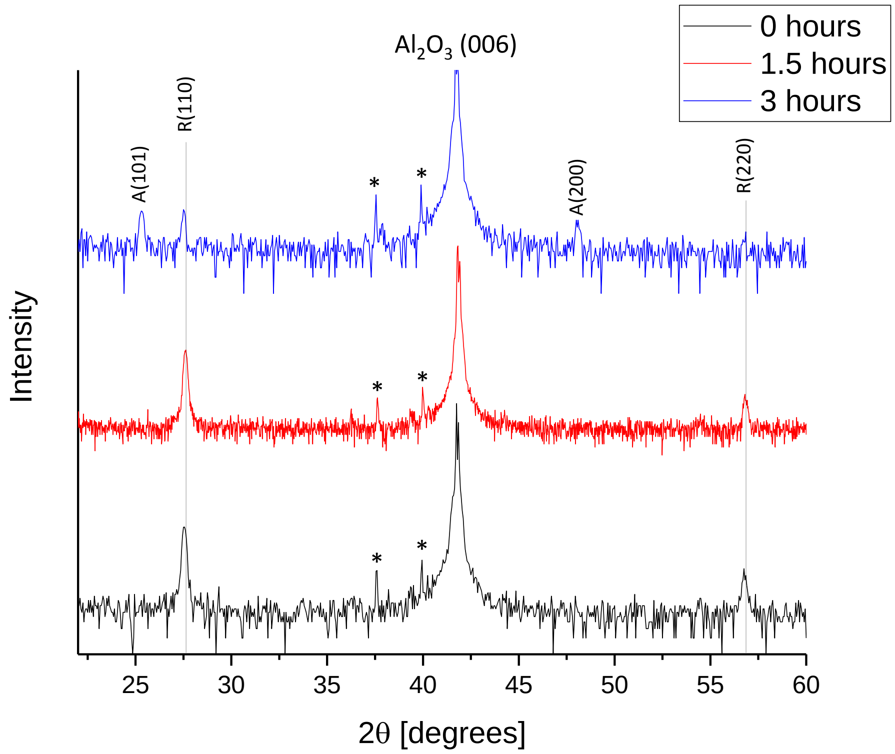

Figure 4.6. XRD of epitaxial rutile (110) and (220) TiO_2 grown on Al_2O_3 (0001). After 1.5 hours of nitrogen doping there is no change. After 3 hours there has been a rutile to anatase conversion. Peaks marked with asterisks originate from the substrate and are an instrumental artefact due to additional wavelengths present in the X-ray radiation.

To further study this interconversion, the XPS valence bands were measured. Figure 4.7 shows a comparison between the valence bands of the pure and doped epitaxial films. Care must be taken as it is known that nitrogen doping itself can cause changes to the valence band of TiO_2 (for both substitutional and interstitial doping), especially introduction of spectral intensity within the band gap (at the low binding energy side of the valence band spectrum), either as localised states close to the Fermi level due to reduction of Ti and filling of the Ti 3d level, or a tailing of the valence band edge due to incorporation of N 2p states.[136,161-164] However, both of these changes tend to be relatively minor compared with the differences between rutile and anatase valence band structures already discussed.[165,166] Therefore we propose that the valence band shape can still be used to differentiate anatase and rutile in these nitrogen doped systems. It is clear that a change occurs in the appearance of the VB spectrum in the r-TiO_2 film deposited on Al_2O_3 after ammonolysis. Whereas before nitrogen doping, the VB spectrum resembled that of a standard sample of r-TiO_2, after 1.5 hours of ammonolysis the relative heights of the VB maxima have changed, and by 3 hours of ammonolysis the VB resembles closely that of a-TiO_2 standard. That the XPS valence band begins to change in shape (after 1.5 hours) before a change in crystal structure can be detected in XRD suggests that the phase transformation begins at the surface of the material (as XPS is highly surface sensitive). This is consistent with the rutile to anatase phase transformation being caused by incorporation of nitrogen from the ammonolysis process.

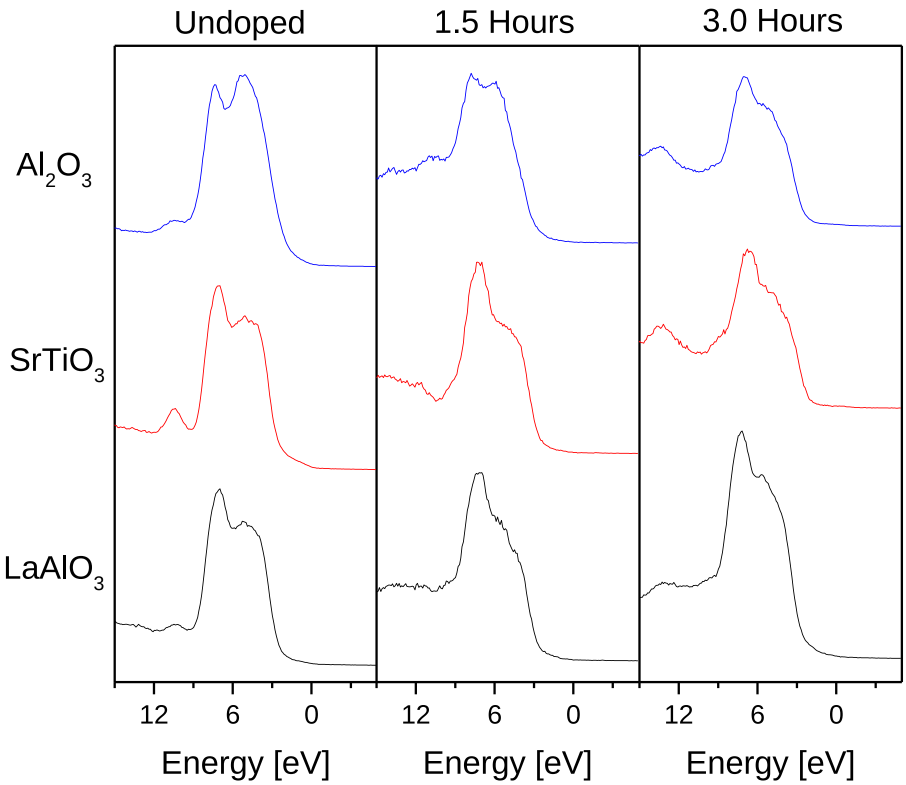

Figure 4.7. A comparison of the valence bands of pure TiO_2 epitaxial thin films and TiO_2 doped via the ammonolysis method.

Figure 4.8 shows the N 1s XP spectra from the epitaxial films as presented after 3 hours of ammonolysis treatment. The binding energy scale was calibrated to adventitious C 1s at 284.8 eV. All films exhibit N 1s peaks at a binding energy between 395-7 eV, which has been assigned to substitutional nitride anions on oxide sites within TiO_2. In all cases there is also a broader, higher binding energy peak centred between 398-400 eV. This environment is associated with interstitially doped nitrogen. There is no indication of a peak above 400 eV in any sample: peaks above 400 eV correspond to oxidised nitrogen species such as nitrates.

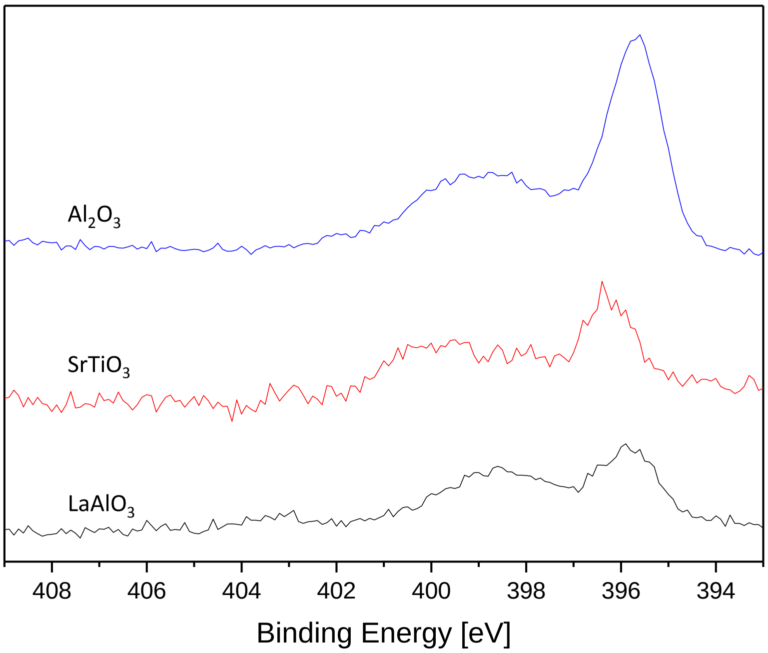

Figure 4.8. Photoemission spectra of the N 1s core lines in the films of epitaxial TiO$_2$ on various substrates doped via ammonolysis. Intensities of peaks are concordant with depth profile results (figure 4.9).

The films were sputtered in-situ with a monoatomic Ar ion gun to determine the distribution of the nitrogen within the films after 3 hours doping. Figure 4.9 shows the depth profile of nitrogen incorporated into the thin films as a percentage. All films show a maximum nitrogen level at the surface which decreases with etching.

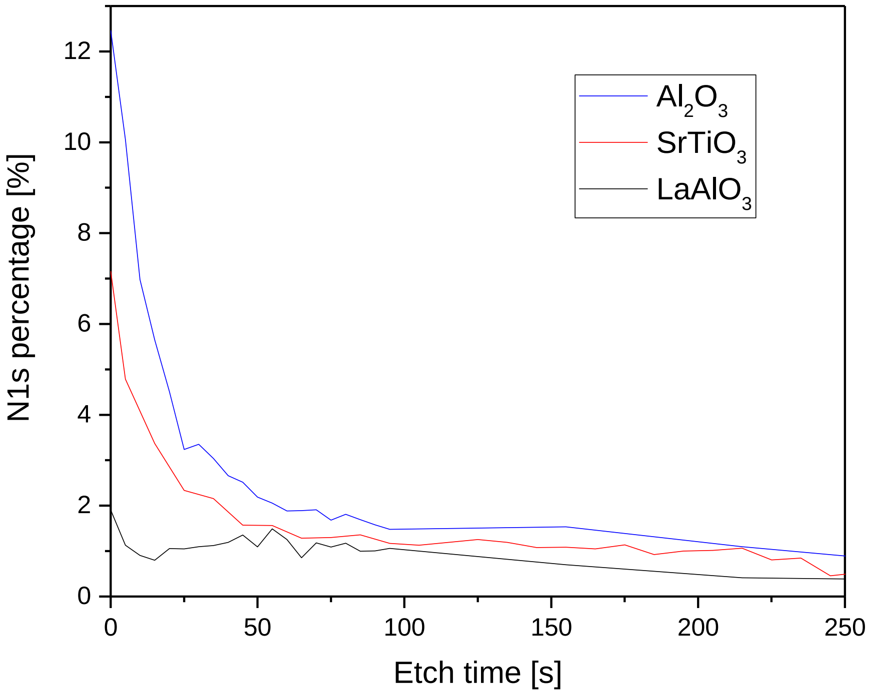

Figure 4.9. XPS depth profile of N-TiO_2 thin films doped via ammonolysis on differing substrates (Al_2O_3, $SrTiO_3$, $LaAlO_3$).

The film epitaxially produced on the Al_2O_3 substrate showed the highest level of surface nitrogen with a value of 12 % calculated from the scanned elements O, N, C, and Ti. The film on STO showed 7% nitrogen after ammonolysis, whilst the film on LAO showed only 2% nitrogen. It is surprising that such a large difference is seen in nitrogen doping levels between the two anatase films, on STO and LAO. This may be due to differing surface morphologies which were not measured, or by the difference in strain: the larger strain in the STO supported film may lead to greater nitrogen incorporation.

4.3.3 Nitrogen Doping by Tetramethylethylenediamine (TMEDA)

A second doping method was investigated. Nitrogen doped TiO_2 films were deposited in a single step by adding TMEDA (0.0129 mol, 1.5g) to the TiO_2 sol prior to coating onto the STO, LAO, and Al_2O_3 single crystal substrates. XRD showed that the presence of the TMEDA did not affect the crystallisation of the films produced on the STO and LAO single crystal substrates which were still oriented with a-TiO_2 (001) as in the undoped films. The film on LAO showed a c-parameter of 9.546 Å, somewhat larger than the undoped LAO film (c = 9.522 Å). In contrast the nitrogen doped a-TiO_2 film on STO showed a c parameter almost identical to the undoped counterpart.

However, the crystallisation of the film produced on Al_2O_3 (0001) was dramatically affected by the presence of TMEDA. Figure 4.10 shows a comparison between the undoped epitaxial rutile film and the two nitrogen doping strategies. It can be seen that doping with the nitrogen source in the sol results in a film showing a-TiO_2 (101) and (200) peaks, and only a very weak r-TiO_2 (110) peak. The film can thus be described as a polycrystalline anatase film which grows despite the rutile templating effect of Al_2O_3 (0001) seen in the undoped materials.

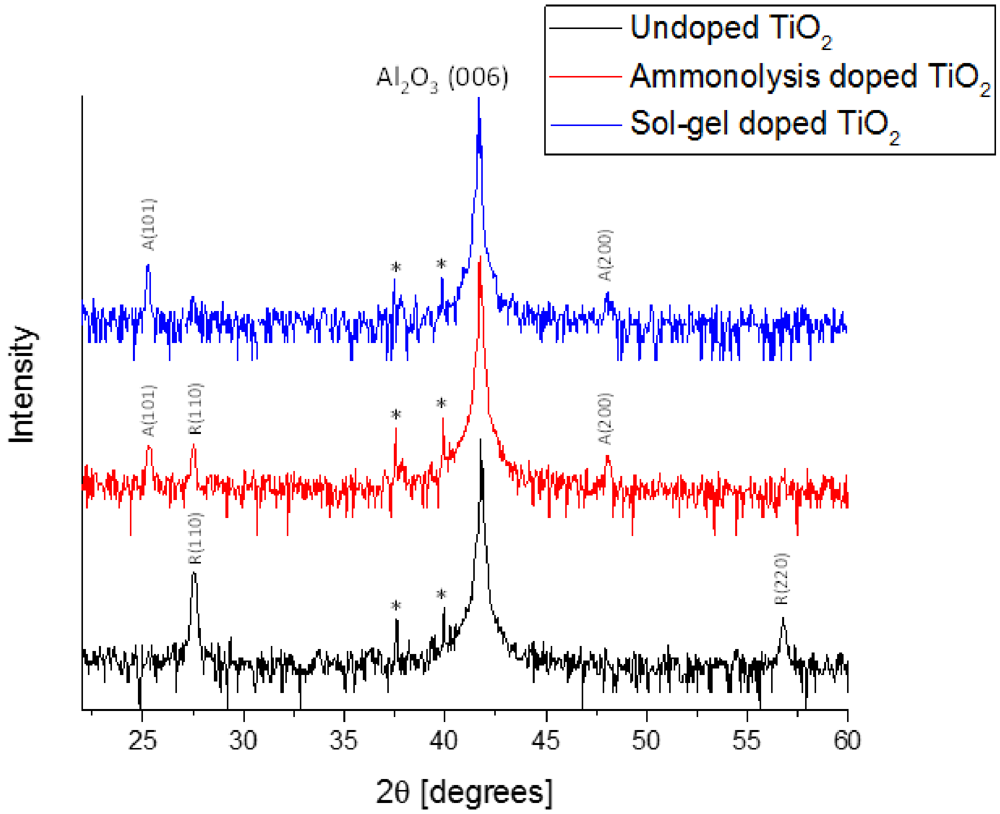

Figure 4.10. An XRD comparison between the undoped epitaxial r-TiO_2 (110) film and the two nitrogen doping strategies. The intensity is on a log scale and offset for clarity.

XPS of the surface nitrogen for the unannealed films in figure 4.11 shows a binding energy of 400-401 eV corresponding to interstitially doped nitrogen in the TiO_2 lattice. There is also the presence of a peak at approximately 403 eV which does not tally with interstitially or substitutionally doped N 1s. This peak is indicative of the unreacted dopant left on the surface of the film. Further evidence for this being unreacted dopant is that after annealing it disappears. Figure 4.12 shows the annealed films to have an N 1s binding energy of approximately 399-402 eV. Again, this is evidence for nitrogen being interstitially doped in the TiO_2 lattice, or possibly oxides of nitrogen at the higher end of the binding energy range observed.

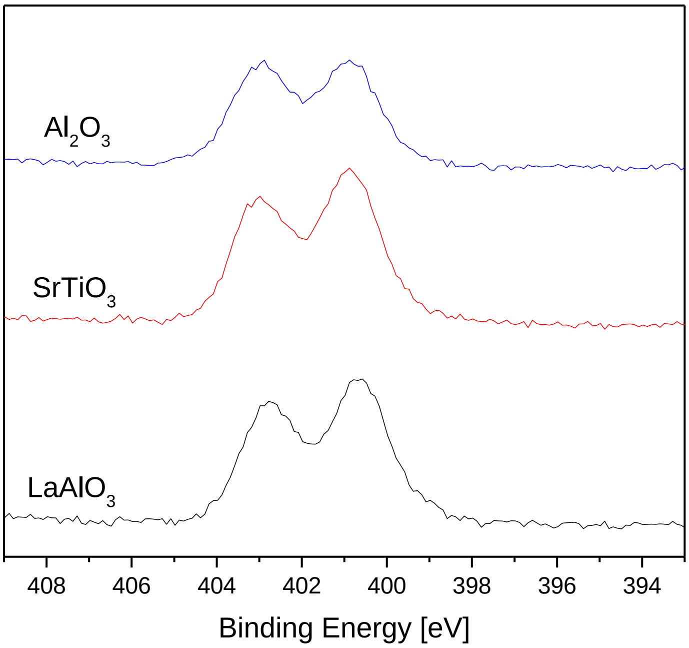

Figure 4.11 Spectra of the binding energies of N 1s in the unannealed films of TiO_2 doped via TMEDA in the TiO_2 sol.

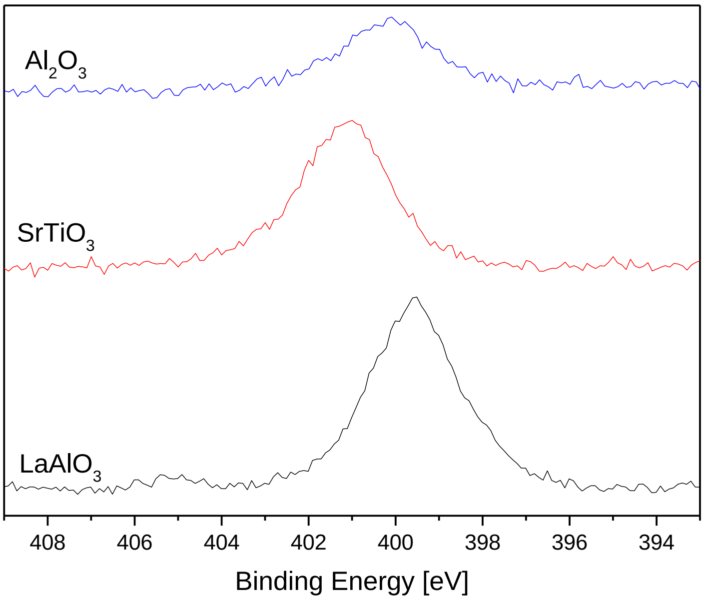

Figure 4.12 Spectra of the binding energies of N 1s in the annealed films of TiO_2 doped via TMEDA in the TiO_2 sol.

In figure 4.13, XPS depth profile analysis of the films before and after annealing shows that for all substrates the nitrogen was initially distributed evenly throughout, although the surface appeared nitrogen depleted compared with the bulk. Upon annealing however, the nitrogen distribution shows a heavy migration to the films surface. Despite being concentrated at the surface post annealing, there is still trace amounts of nitrogen throughout the films. Calculating the area under the two differing curves shows an approximate loss of 90 %, 88 %, and 84 % nitrogen within the depth measured for Al_2O_3, STO, and LAO films respectively. This migration and loss of nitrogen dopant may be an important process in nitrogen doping of TiO_2 that is likely to impact on the functionality.

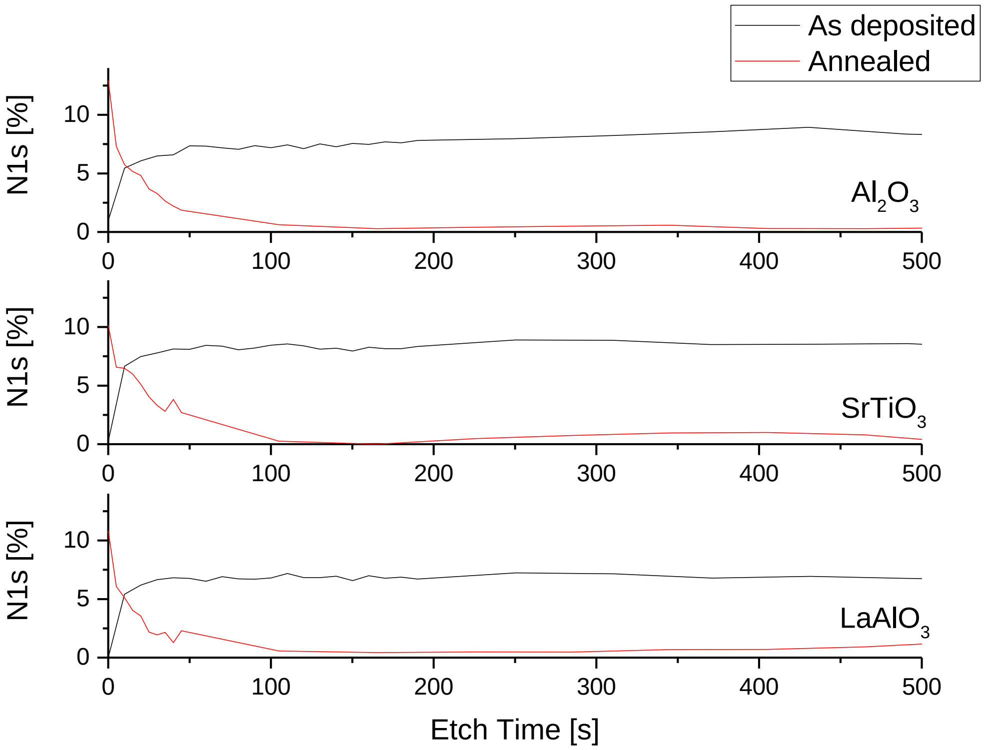

Figure 4.13. XPS sol-doped depth profiles of N 1s before and after annealing.

Figure 4.14 shows a comparison of the XPS valence bands of the films produced on the varying substrates and their sol-doped counterparts both as-deposited and annealed. As discussed previously, in the undoped epitaxial films the valence band spectra closely resemble the model compounds (a-TiO_2 and r-TiO_2) according to the templating substrate. TMEDA doped samples before annealing show a broad and featureless valence band spectra which can be expected to include contributions from the molecular nitrogen precursor and titanium alkoxide gel film. Post annealing, all samples show valance band spectra that closely resemble the a-TiO_2 standard. This confirms the phase assignment by XRD, and further supports the hypothesis that nitrogen doping stabilises anatase over rutile in these epitaxial systems.

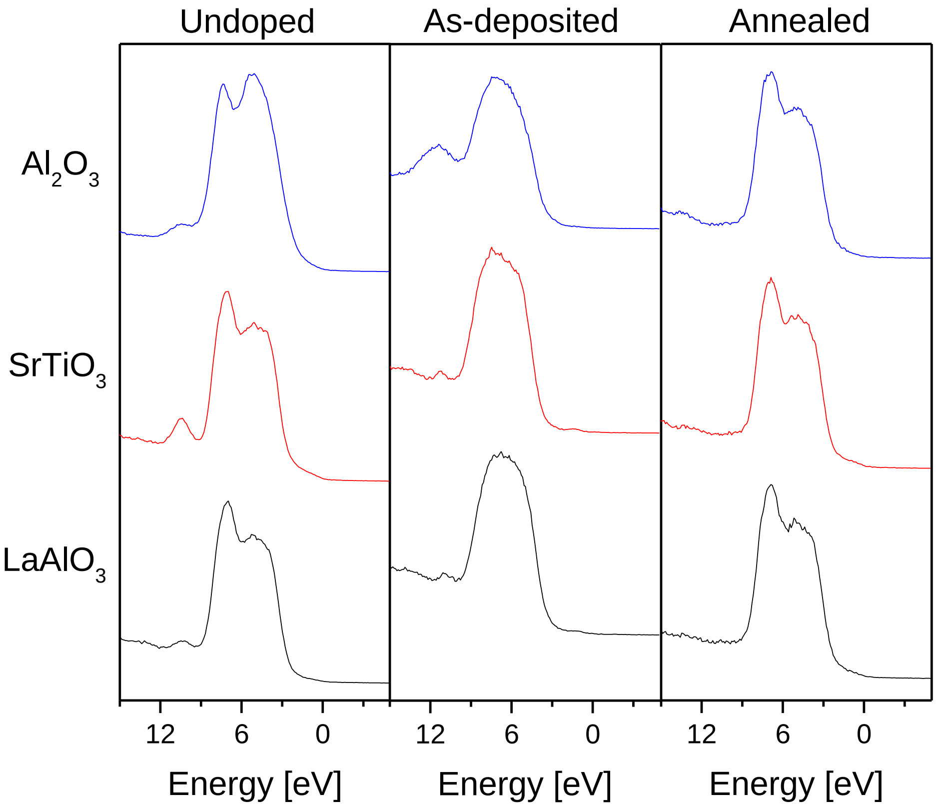

Figure 4.14. A comparison of the valence bands of thin films of pure TiO_2 (left) and TiO_2 doped via TMEDA in the sol (middle – with no heat treatment and right – after heat treatment to effect crystallisation).

Figure 4.15 shows SEM images of the films after doping. Films produced on the perovskite substrates STO and LAO show aligned crystallites of similar sizes in accordance with and epitaxial film, and in agreement with previous XRD and XPS results. Films produced on the Al_2O_3 substrate look polycrystalline and disordered which again confirms the rutile-anatase conversion induced by nitrogen doping.

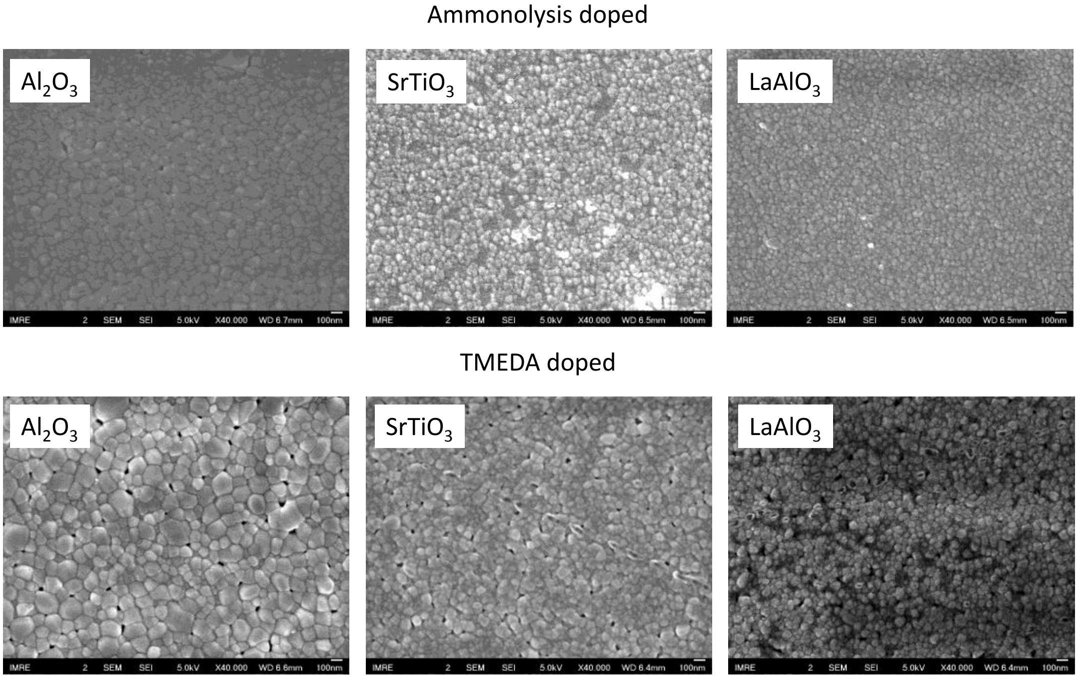

Figure 4.15. SEM images of nitrogen doped TiO_2 films (ammonolysis top, TMEDA bottom).

4.3.4 Photocatalysis

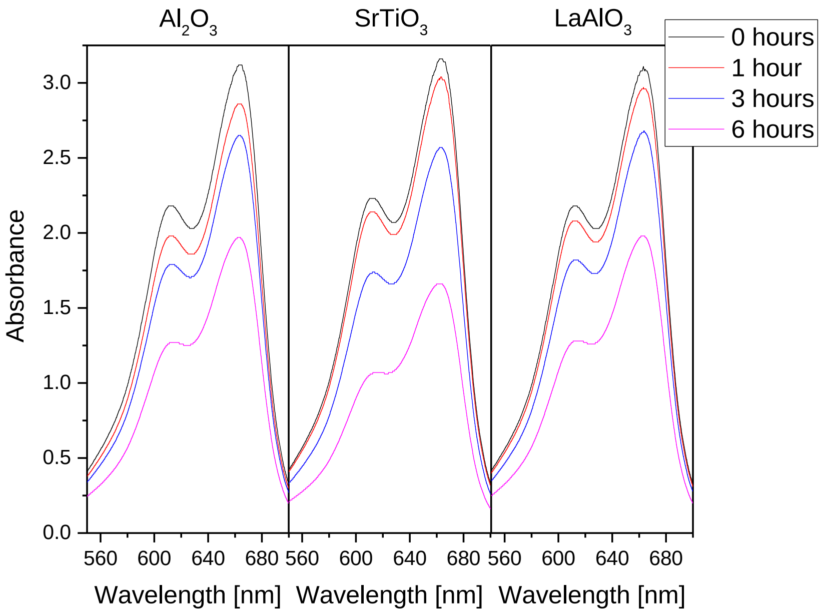

Figure 4.16. The photocatalytic degradation of methylene blue in the presence of the ammonolysis doped TiO_2 thin films and an AM 1.5 solar simulator.

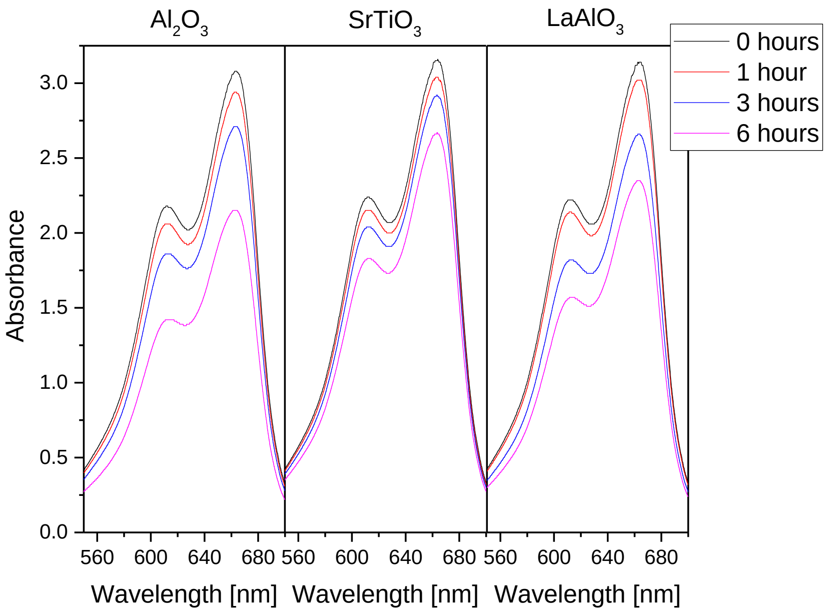

Figure 4.17. The photocatalytic degradation of methylene blue in the presence of the TMEDA doped TiO_2 thin films and an AM 1.5 solar simulator.

Figures 4.16 and 4.17 show the decrease in the absorbance of methylene blue for both methods of doping in all films. The characteristic peaks at 668 nm and 609 nm degraded at the same rate. The rates of the degradation compared to a blank glass substrate can be seen in figures 4.18 and 4.19. Figure 4.18 shows a slight photocatalytic effect from films on all substrates in comparison to the blank glass substrate. However, the rate of the degradation is slow, possibly due to the sample size. Figure 4.19 shows the rate of degradation as approximately equal to the blank glass substrate revealing little or no photoactivity. Any existing photoactivity may be revealed with larger sample sizes.

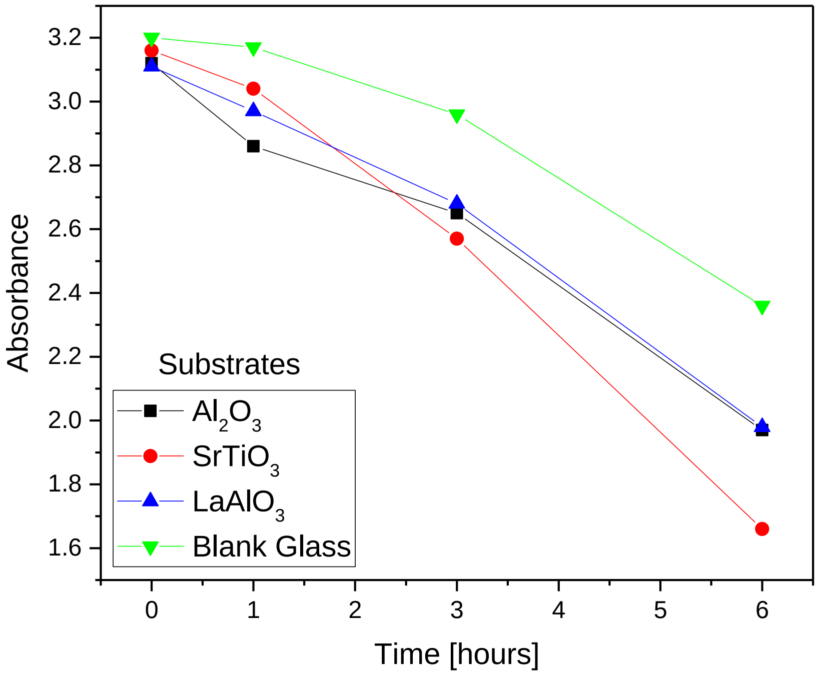

Figure 4.18. The decrease in absorbance of methylene blue (at 668 nm) in the presence of the ammonolysis doped TiO_2 thin films and an AM 1.5 solar simulator.

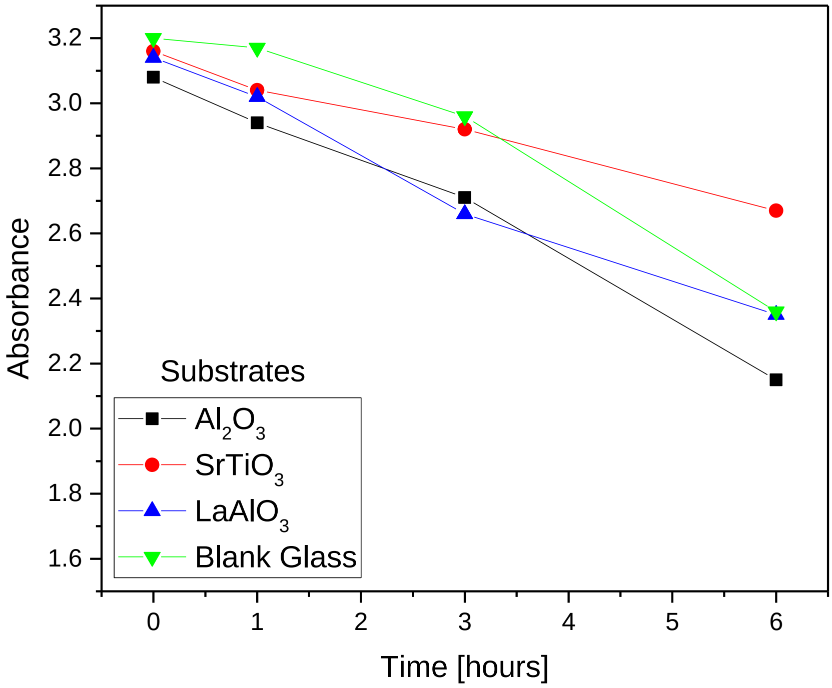

Figure 4.19. The decrease in absorbance of methylene blue (at 668 nm) in the presence of the TMEDA doped TiO_2 thin films and an AM 1.5 solar simulator.

4.4 Conclusions

This chapter studied a series of highly oriented TiO_2 films grown by solution phase methods on perovskite and c-cut sapphire substrates. In accordance with literature precedent, the perovskite substrates templated anatase (001) growth, while the Al_2O_3(0001) templated rutile. Nitrogen doping through two routes has been achieved: firstly doping through ammonolysis of the TiO_2 highly oriented films. Secondly, incorporation of a nitrogen precursor into the wet chemical deposition. It was revealed that ammonolysis causes a reverse rutile-to-anatase phase transition in films deposited on Al_2O_3(0001), and this is confirmed by XRD and valence band XPS, which is used here to distinguish anatase and rutile TiO_2 phases through their differing spectra shapes. Doping with TMEDA also stabilised anatase, and such films showed anatase phase even on the Al_2O_3(0001) substrate. Depth profiling showed a significant migration of nitrogen from bulk to surface on annealing of TMEDA doped TiO_2 films. These results shed light on previously unknown aspects of the N doping process in TiO_2. The rutile to anatase transition seen here may help explain the enhanced photocatalytic performance of nitrogen doped TiO_2, as rutile–anatase heterojunctions are known to be highly effective at promoting photocatalysis. However our photocatalytic studies were limited by sample size.

Chapter 5: Non-Crystalline TiO_2

5.1 Introduction

The following chapter outlines a novel synthesis of non-crystalline TiO_2 thin films with high photocatalytic activity. Less crystalline, more amorphous phases of titania have often been disregarded for catalytic roles, as the pure amorphous phase of titania (am-TiO_2) is said to have negligible photocatalytic ability due its disordered structure and large band gap.[167] However, more recently this simple preconception has become challenged and there have been many reports of pure and composite, non-crystalline materials behaving as highly effective catalysts.[168-172]

Non-crystalline oxides can be classified (in terms of increasing nearest-neighbour atomic order) as amorphous or vitreous.[173] A film can be described as amorphous if it has no short-range order (SRO) i.e., where its nearest-neighbour coordination differs throughout. A vitreous oxide film has SRO i.e., continuous atomic coordination throughout the film, and may contain ordered domains beyond its nearest-neighbour, but has no long-range order (LRO).

This emergence of effective amorphous phase photocatalysts is because crystallinity is one of several factors in TiO_2 photocatalysis. There are other attributes to take into account such as: particle size[174], surface hydroxyls[175], and surface area[176]. While high crystallinity is advantageous for the prevention of electron and hole recombination, far larger surface areas can be achieved with amorphous phases, which provides far more adsorption sites. A thin film grown at approximately room temperature is likely to have a degree of complexity due to a lack of LRO.

5.2 Method

10x10x1 mm^3 glass substrates were washed with acidic (3:1 H_2SO_4 to H_2O_2) piranha solution and DI water before deposition. The backside was fully covered with a piece of thermal tape. They were suspended face down in a freshly prepared solution of 0.1 M ammonium hexafluorotitanate (AHFT) and 0.3 M boric acid. The container was then sealed and placed in a convection oven at 40 °C for 2 hours. The films were then washed with DI water and blown dry. After synthesis the films were handled and stored in air.

A qualitative method for comparing the films' porosity was performed using an acidified (1 M HCl) aqueous solution of methylene blue (0.1 mM) and a same sized sample of Pilkington Activ glass. The samples were submerged in the methlylene blue solution overnight, removed, and dried. The adsorbed dye on the films was then redissolved in 1M hydrochloric acid. The relative concentrations of each were determined by comparing the absorbance spectra with a calibration curve of methylene blue concentrations ranging from 0.05-0.8 × 10^{-7} M.

To test the photocatalytic activity of the films, dye degradation studies were performed. The films, along with blank and Pilkington Activ^{TM} glass samples of the same size, were placed in 5 cm^3 of aqueous, 45 µM solutions of methylene blue. Fresh films were also spin-coated with a solution of hydroxyethyl cellulose (HEC) (1.5% aqueous solution; 3g), glycerol (0.3g), and Resazurin (4mg). The films and the controls were then irradiated with an AM1.5 solar simulator.

5.3 Results

5.3.1 Characterisation

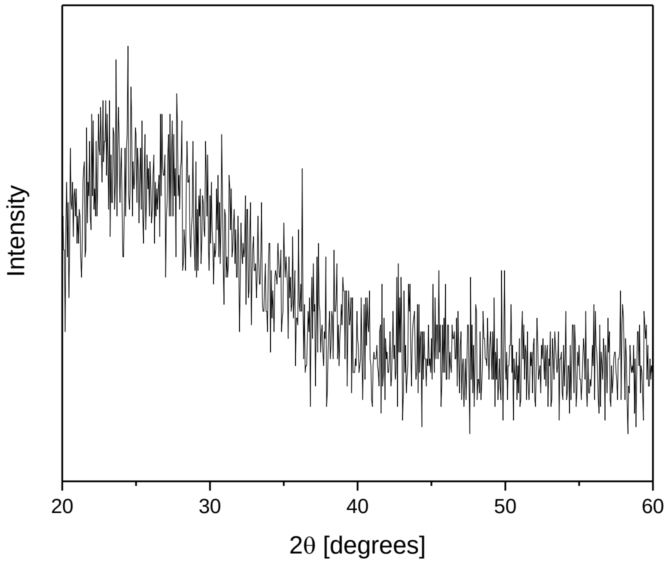

Figure 5.1. XRD of the LPD synthesised TiO_2 film. The broad peak at 2θ=25-35° can be attributed to the glass substrate. No crystalline peaks are present.

Figure 5.1 shows the X-ray diffraction from the films. No crystalline peaks are visible in the diffraction pattern and the broad peak ranging from 2θ=25-35° is due to the glass substrate. The lack of peaks present indicates a non-crystalline film with no LRO. This is justifiable due to the films being synthesised at low temperature (40 °C) with no subsequent annealing stage to promote crystallinity.

This non-crystallinity was further confirmed with scanning electron microscopy (SEM). Figure 5.2 shows the films to have an unaligned surface morphology and the cross-sectional SEM reveals a thickness of approximately 100 nm.

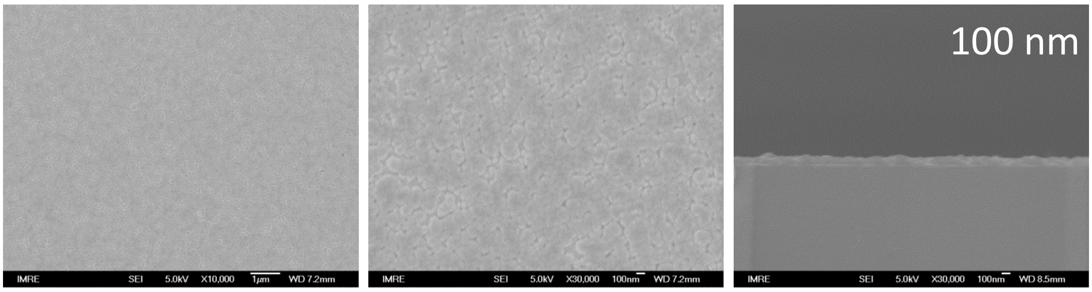

Figure 5.2. SEM images of the amorphous TiO_2 film. Cross-sectional SEM shows a thickness of approximately 100 nm.

Previously, it has been found that the optical properties of TiO_2 films are unchanging with crystallisation.[177] Here the films were effectively transparent, and figure 5.3 shows the spectrum of the film is identical to the substrate. Therefore the band gap of the film must be greater than the direct Tauc plot for allowed transitions in figure 5.4, approximately 3.7 eV; considerably higher than anatase 3.20 eV and rutile 3.03 eV[178]. The work function of the films was determined to be 5.54 eV via a photoelectron spectrometer (figure 5.5). Much higher than reports of crystalline TiO_2 which is approximately 4.13 eV[179] for rutile, and ranges from 4.23 to 5.23 eV for anatase.[180]

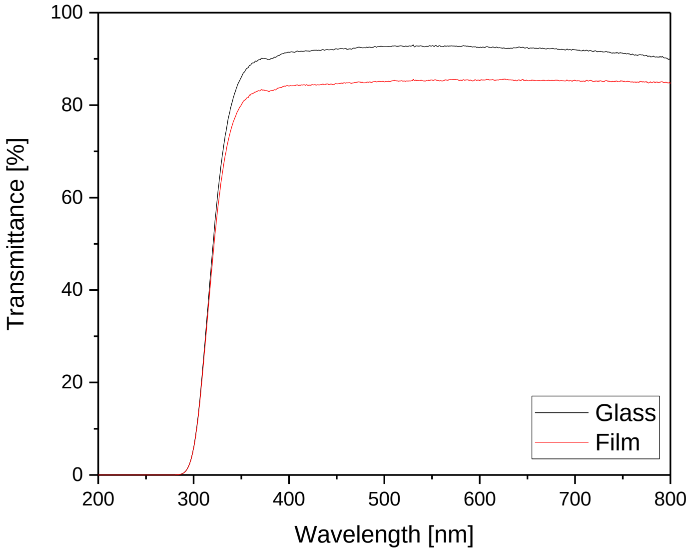

Figure 5.3. Transmittance spectrum of the non-crystalline film. The film is effectively transparent throughout the visible light spectrum.

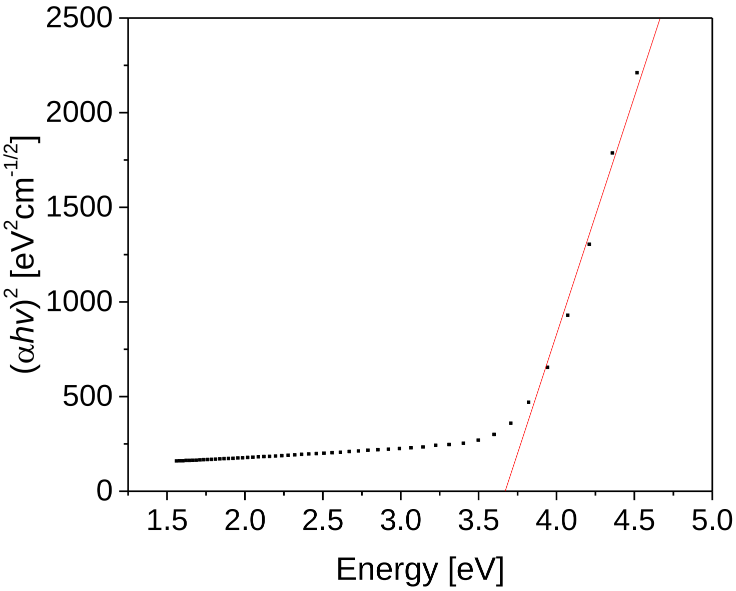

Figure 5.4. A Tauc plot for allowed direct transitions of the film. α = 1/d*ln(1/T) where d is the film thickness and T is the transmittance.[181]

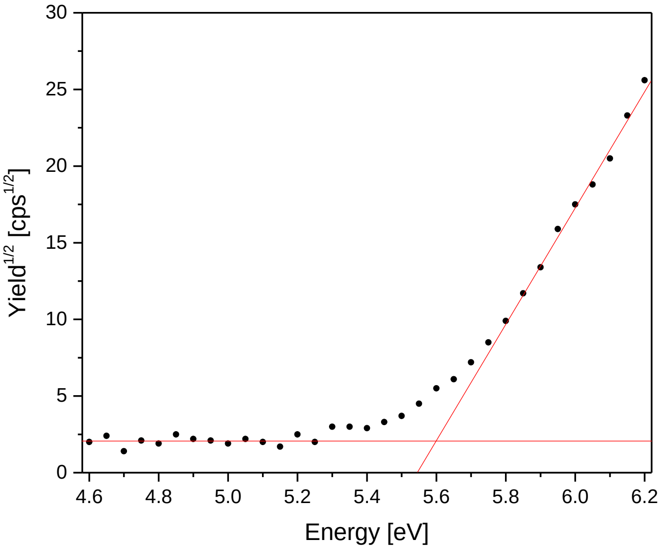

Figure 5.5. Work function of the film determined by photoelectron spectroscopy in air (PESA) at atmospheric pressure.

The composition of the films was revealed by X-ray photoelectron spectroscopy and figure 5.6 shows a large proportion of fluorine 1s on the surface and a binding energy of approximately 685 eV. This fluorine is residual from the ammonium hexafluorotitanate (AHFTi) precursor and depth profiling showed that it was present throughout the films. The atomic percentages for Ti, O, and F were shown to be 23.4%, 68.7%, and 8.1% respectively. The O 1s spectrum exhibits a large, narrow peak 530.5 eV which is typical of O-Ti (fig.5b). There is also broader shoulder at a higher binding energy of a 532.6 eV. This is indicative of hydroxyl groups on the surface of the film. These OH groups account for 7.6% of the surface scan composition.

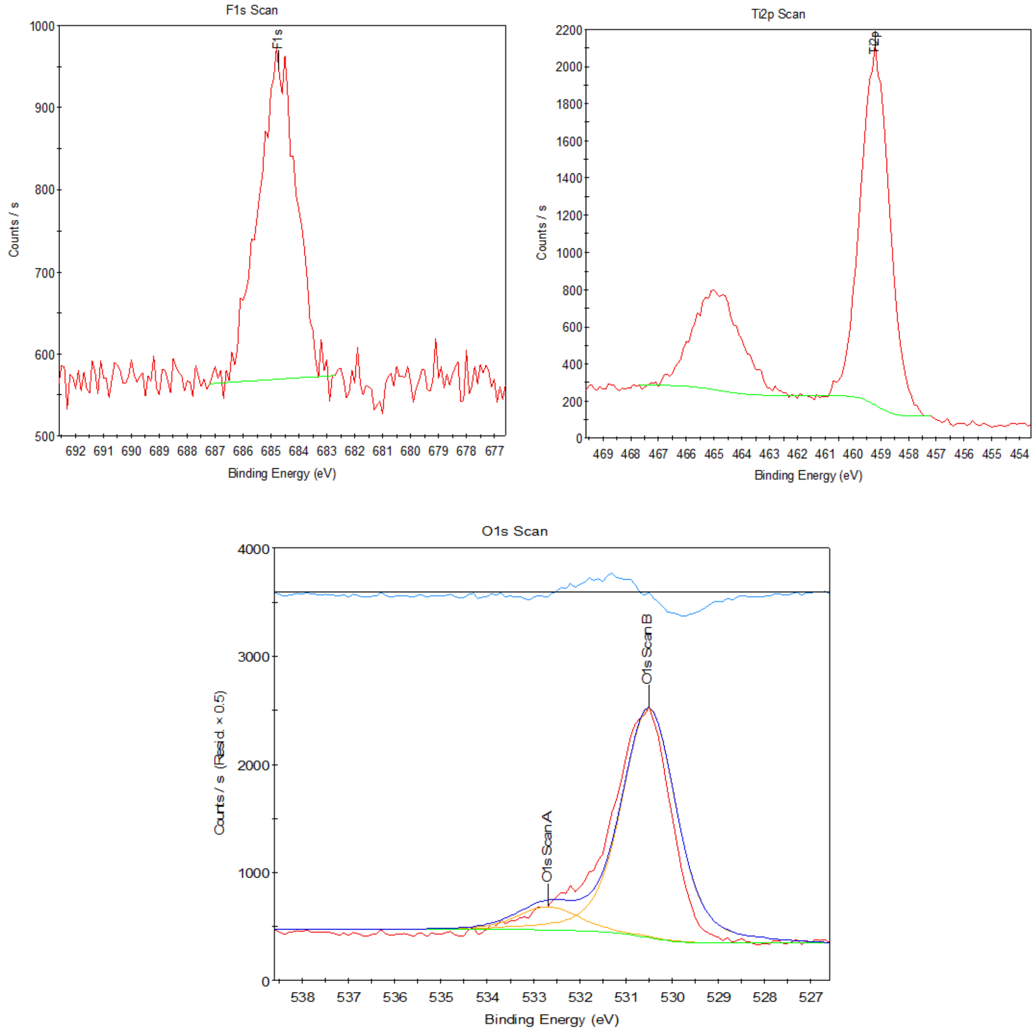

Figure 5.6. X-ray photoelectron spectra of Ti 2p, O 1s, and F 1s in the films. Peaks were fit with a Shirley background.

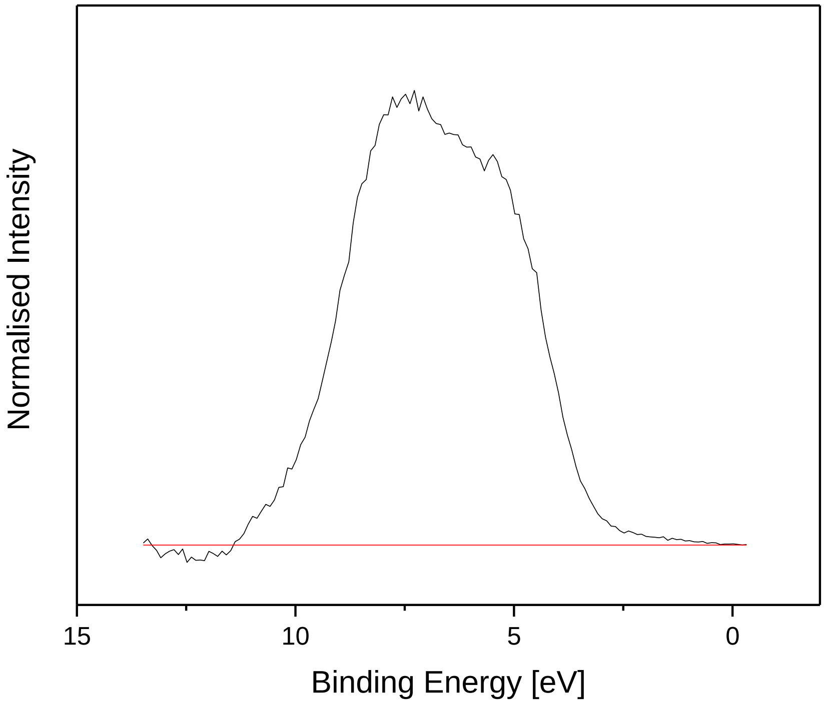

Figure 5.7. Valence band X-ray photoelectron spectrum of the film.

Figure 5.7 shows the valence band XPS of the film. An accurate fit of the valence band shape was attempted using the previously modelled anatase and rutile standards (chapter 3 and 4), but was not possible. The distinctive shape of the VB could be due to the residual reactants in the film, or could be due to the non-crystallinity of the film, or a combination of both of these factors. However, any attempt to remove the residual reactants by annealing the films (>300 °C) resulted in anatase crystallisation visible by XRD. Of the two standards, the VB had a more accurate fit with anatase. This, in conjunction with its ready crystallisation to anatase under temperatures above 300 °C, implies that the film has anatase SRO and could be nano-crystalline.

5.3.2 Determination of Porosity

Transmission electron microscopy again confirmed that the film was amorphous or vitreous in nature, but also revealed a degree of porosity (figure 5.8). High porosity is common in films without LRO and may contribute to increased photoactivity due to an increased surface area.

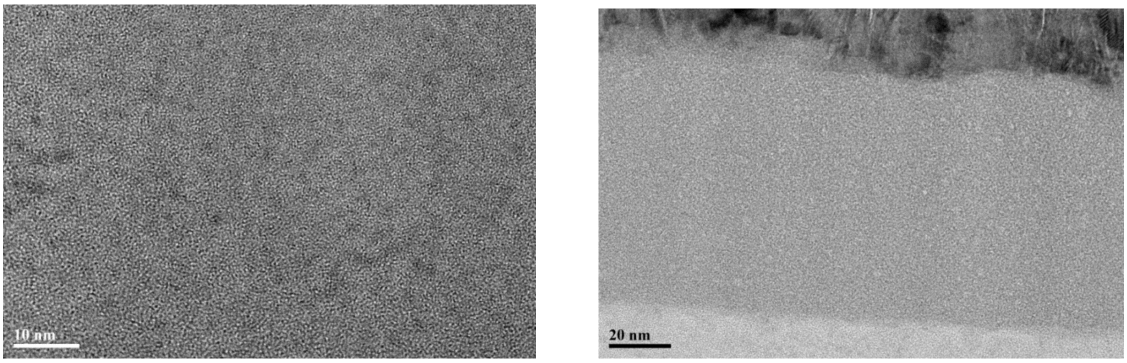

Figure 5.8. Transmission electron microscopy images of the amorphous film revealing porosity.

Figure 5.9 shows the films exhibiting superhydrophilicity, with the water contact angle of the coated glass substrate being < 5° without the use of UV irradiation. This again confirms the porous nature of the films, as traditional TiO_2 superhydrophilicity requires the presence of UV light.[182] In this case, the capillary action of the pores in the film is creating a superhydrophilic effect.

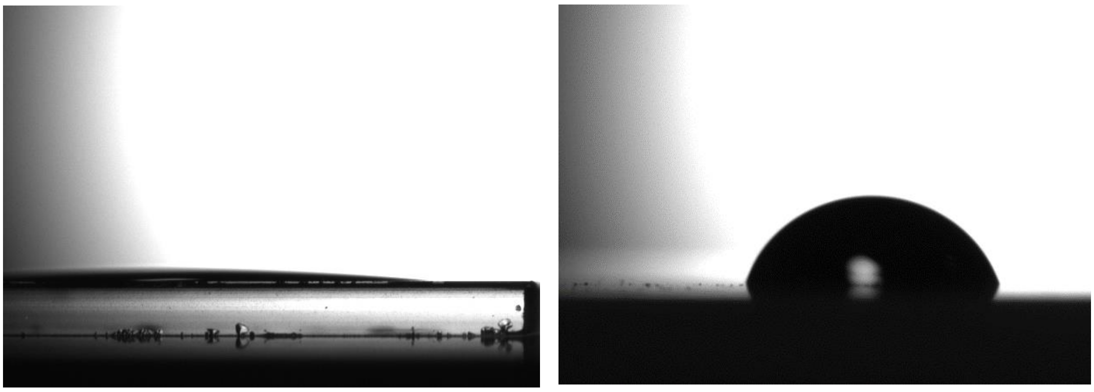

Figure 5.9. Water contact angle measurements of the amorphous TiO_2 film (left) and uncoated glass (right).

This porosity was determined relative to the industry standard for self-cleaning glass: Pilkington Activ^{TM} (figure 5.10). The calibration curve showed that the amorphous TiO_2 films had adsorbed over 4 times the amount of methylene blue compared with Activ^{TM} glass. This porosity discrepancy will not only affect the hydrophilicity of the film, but will have dramatic effects on its photocatalytic abilities as well.

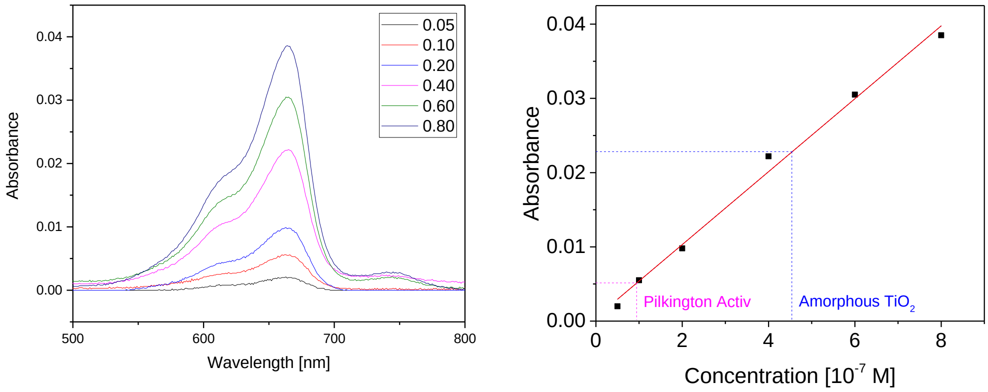

Figure 5.10. The absorbance spectra taken from solutions of methylene blue in concentrations ranging from 0.05-0.8 × 10^{-7} M (left) and the subsequent calibration curve plotted with the Pilkington Activ^{TM} glass and the amorphous TiO_2 film comparisons (right).

5.3.3 Synchrotron Analysis

To further investigate the SRO of the films, analysis at the X-ray Absorption Fine structure for Catalysis (XAFCA) beamline in the Singapore Synchrotron Light Source (SSLS) was performed. Figure 5.11 shows the results of data gathered from the Ti k-edge of the amorphous film on glass stacked with the standards used. The tetrahedral titania standard used was the molecular compound $Ti(OSiPh_3)_4$.[183]

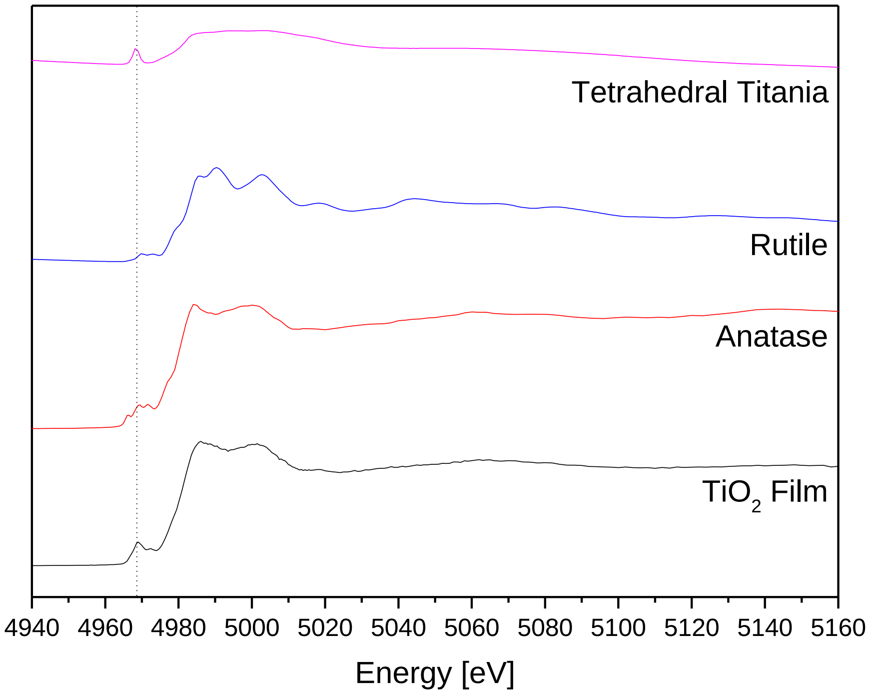

Figure 5.11. The X-ray absorption near edge structure (XANES) of the Ti k-edge in the amorphous TiO_2 films compared with anatase, rutile, and tetrahedral standards.

The XANES of the film is reminiscent of anatase TiO_2, but there is a large peak present in the pre-absorption edge at approximately 4970 eV that can be attributed to tetrahedral Ti.[183] A linear combination fit (LCF) indicated that the overall structure was 85.5% anatase, 10.3% tetrahedral, and 4.2% rutile with a χ^2 of 0.0006 (figure 5.12). The fact that the XANES shows the films to be mostly anatase means that they are not truly amorphous, but can be described as vitreous or nano-crystalline anatase with SRO.

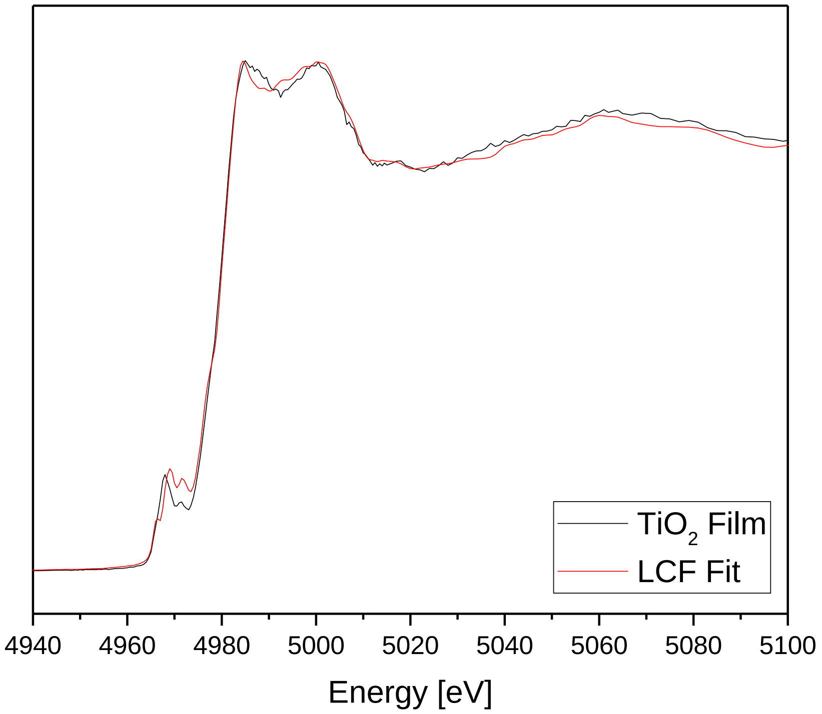

Figure 5.12. A linear combination fit of the Ti k-edge in the amorphous TiO$_2$ films, with standards of anatase, rutile, and tetrahedral titania compound: Ti(OSiPh$_3$)$_4$.

5.3.4 Photocatalysis

The photocatalytic ability of the film was compared again to the industry standard, Pilkington Activ^{TM} glass. Figure 5.13 shows the degradation of methylene blue dye under an AM1.5 solar simulator. A glass substrate was used as a control and can be seen to degrade somewhat (due to UV wavelengths in the solar spectrum), but both the amorphous and the Activ^{TM} glass degrade the dye at a higher rate than the control (figure 5.14).

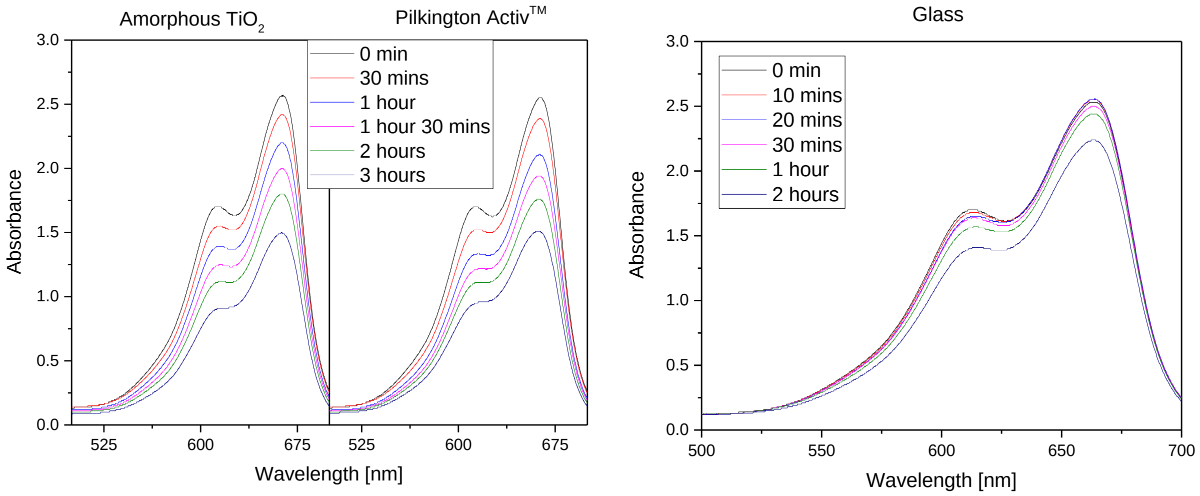

Figure 5.13. Methylene blue dye degradation spectra using the amorphous TiO_2 film in comparison to a same sized sample of Pilkington Activ^{TM} glass and an uncoated glass sample as a control.

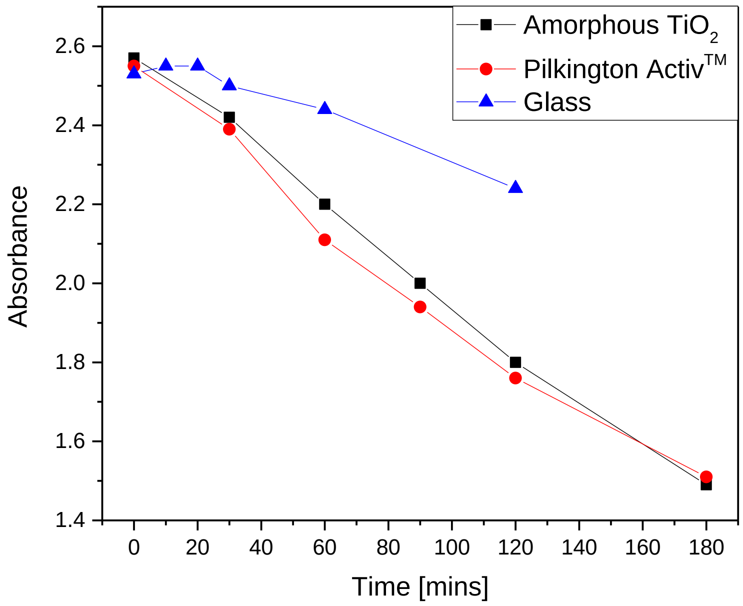

Figure 5.14. Decrease in absorbance for the methylene blue peak (663-4 nm) after exposure to the solar simulator.

The photocatalytic ability of the film was further established by spin-coating a Resazurin dye onto the film and irradiating with an AM1.5 solar simulator. The absorbance spectra of the samples can be seen vary drastically in their degradation (figure 5.15).

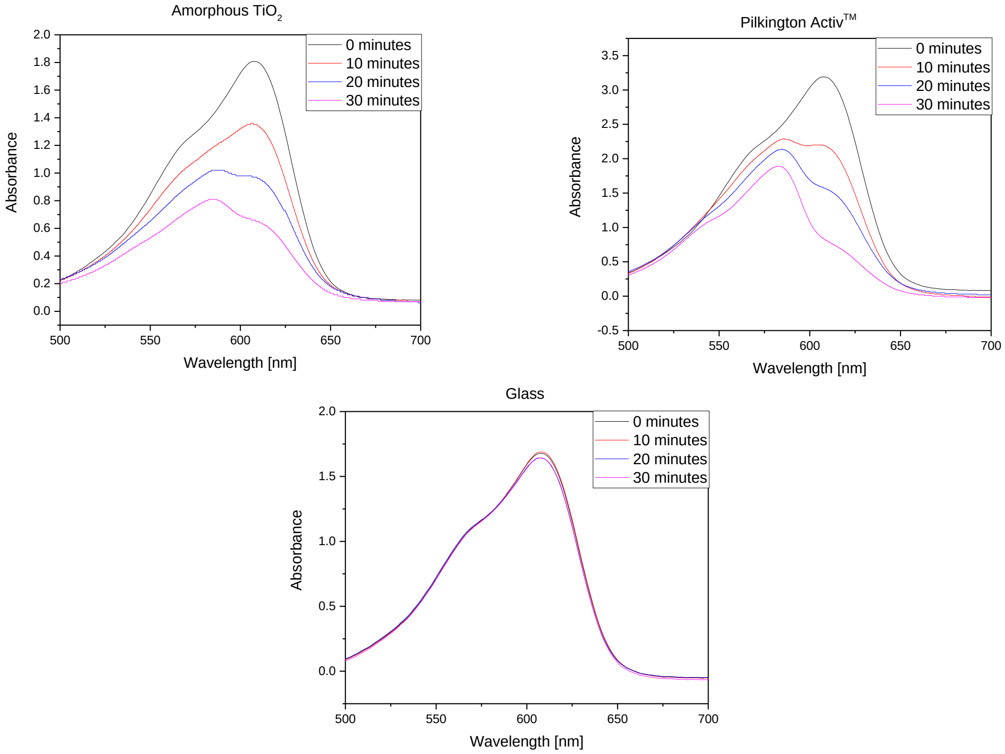

Figure 5.15. Resazurin dye degradation spectra using the amorphous TiO_2 film in comparison to a same-sized sample of Pilkington Activ™ glass and an uncoated glass sample as a control.

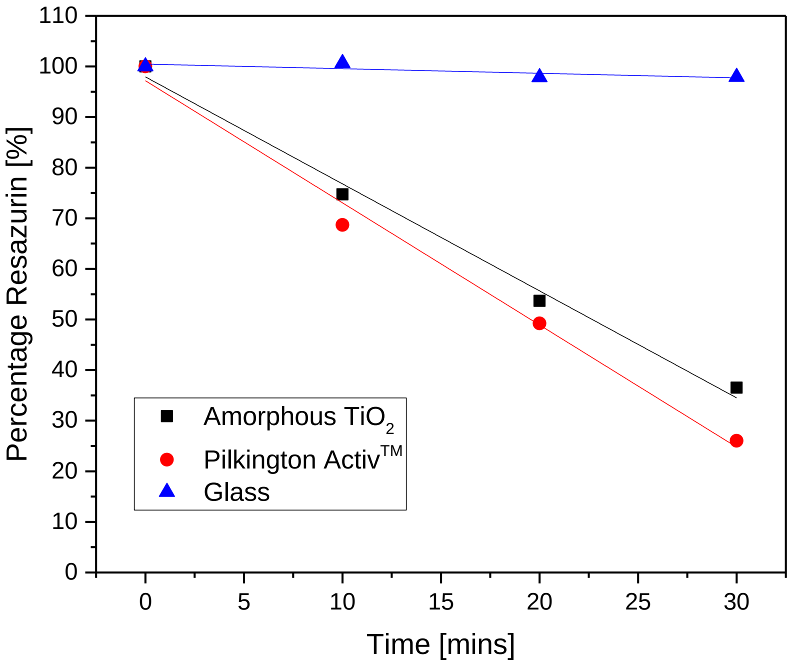

Figure 5.16. The Resazurin absorbance peak at 608 nm, normalised as a percentage of the total peak height for all substrates.

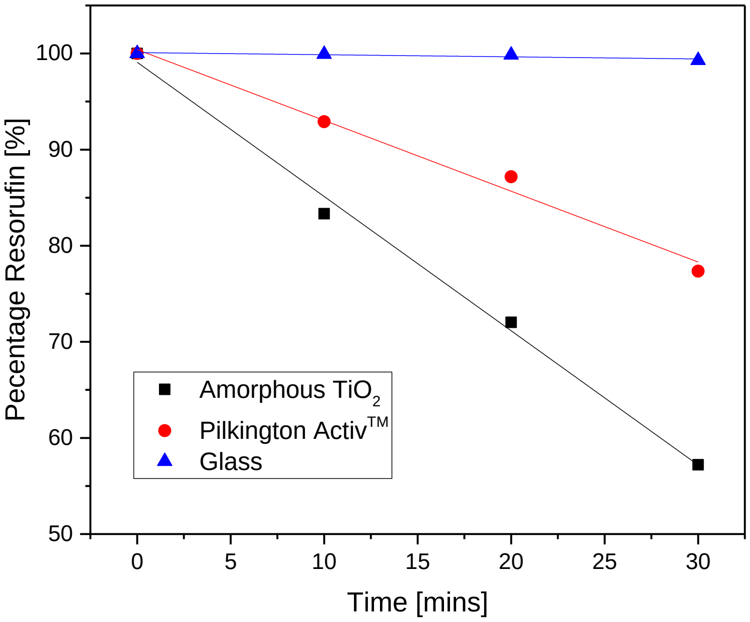

Figure 5.17. The Resorufin absorbance peak at 580 nm, normalised as a percentage of the total peak height for all substrates.

Figure 5.15 shows that the absolute values of the absorbance spectra vary between the substrates, and so to accurately compare the degradation rate of Resazurin, it was plotted as a percentage of the initial peak height. In figure 5.16, for both the amorphous film and Pilkington Activ^{TM}, the photocatalytic activity is comparable. However, figure 5.17 shows a comparison of the Resorufin degradation rate and the difference is stark. In other photocatalytic studies, Resorufin is slow to degrade, if at all,[123,184,185] however the amorphous films can be seen to degrade the Resoruifn at a rate twice that of Pilkington Activ^{TM}. This further confirms the potent photocatalytic activity of the films.

5.4 Conclusion

Non-crystalline, mesoporous TiO_2 films were produced on glass via an LPD method. These films proved to be highly photocatalytic, degrading dyes under solar conditions with greater or equal efficiency than Pilkington Activ^{TM}. The high photoactivity can be attributed to the mesoporosity of the films increasing the surface area (to 4 times that of Pilkington Activ^{TM}) in combination with the highly photocatalytic nano-anatase SRO of the films. The results of this chapter are in agreement with other research that describes non-crystalline TiO_2 as having anatase-like qualities.[31] Synchrotron X-ray absorption analysis of the films showed a considerable amount of tetrahedral Ti present. This tetrahedral character of the Ti can be attributed to uncoordinated structural units [TiO_4] on the films surface and to a lesser extent within the bulk.

The lack of long range order and metastable thermodynamics mean that the amorphous TiO_2 films exhibit novel properties and have potential applications as visible light photocatalysts[186,187], or in self-cleaning applications due to its superhydrophilicity.[188,189]

Chapter 6: Conclusion

6.1 Summary of Results

A novel method of quantitative phase analysis using valence band X-ray photoelectron spectra is presented and applied to the analysis of TiO_2 anatase-rutile mixtures. The valence band spectra of pure TiO_2 polymorphs were measured, and these spectral shapes used to fit mixed phase samples. This yields a surface phase fraction, which represents the percentage of each phase at the surface of the material, and contrasts with traditional X-ray diffraction methods, which are bulk sensitive. Mixed phase samples were prepared from high and low surface area anatase and rutile powders. In the samples studied here, the surface phase fraction of anatase was found to be linearly correlated with photocatalytic activity of the mixed phase samples, even for samples with very different anatase and rutile surface areas.

Highly oriented TiO_2 thin films were deposited onto Al_2O_3(0001), $SrTiO_3$(001), and $LaAlO_3$(001) substrates by spin coating a titanium alkoxide precursor solution followed by annealing. The films were nitrogen doped by two different routes: either adding by tetramethylethylenediamine (TMEDA) to the precursor solution or alternatively by high temperature ammonolysis. Undoped TiO_2 films were highly oriented and the phase was dependent on the substrate. N doping by ammonolysis led to transformation of rutile films to anatase, confirmed by XRD and by XPS valence band spectroscopy. Significant differences were observed in the spatial distribution of the nitrogen dopant depending upon which synthesis method was used. These two factors may shed light on the increased photocatalytic efficiencies reported in N doped TiO_2.

TiO_2 thin films were deposited onto glass substrates at 40 °C via a liquid phase deposition method. The films were shown to be amorphous via X-ray diffraction techniques and porous via transmission electron microscopy. The films exhibited superhydrophilicity without the use of UV irradiation. Further XANES analysis showed the films to have anatase-like short range order along with a significant tetrahedral titania component. The films proved to be photocatalytic by the degradation of methylene blue and Resazurin (Rz) dyes. The photocatalytic activity of the films was shown to be comparable to Pilkington Activ^{TM}.

6.2 Further Investigations

The valence band XPS technique for phase identification developed during this thesis can be extended to many other areas. Theoretically any compound that displays polymorphic behaviour can be investigated. *In situ* studies of the surface structure crystallisation would be especially worthwhile in conjunction with traditional XRD analysis. Crystallisation studies of the amorphous TiO_2 films could also be performed (comparing XPS, XRD, and XAS results) with accompanying dye degradation studies to elucidate the trend in photocatalytic activities.

References

1. Fujishima, A., and Honda, K., *Nature* (1972) **238** (5358), 37
2. *U.S. Geological Survey* (2016), 170
3. Braun, J. H.*, et al.*, *Progress in Organic Coatings* (1992) **20** (2), 105
4. Sadrieh, N.*, et al.*, *Toxicological Sciences* (2010) **115** (1), 156
5. Goodeve, C. F., *Transactions of the Faraday Society* (1937) **33** (0), 340
6. Holladay, J. D.*, et al.*, *Catalysis Today* (2009) **139** (4), 244
7. Kawai, T., and Sakata, T., *Nature* (1980) **286** (5772), 474
8. Frank, S. N., and Bard, A. J., *J Phys Chem-Us* (1977) **81** (15), 1484
9. Fox, M. A., and Dulay, M. T., *Chemical Reviews* (1993) **93** (1), 341
10. Heller, A., *Accounts of Chemical Research* (1995) **28** (12), 503
11. Honda, H.*, et al.*, *Journal of the Illuminating Engineering Society* (1998) **27** (1), 42
12. Sunada, K.*, et al.*, *Environmental Science & Technology* (1998) **32** (5), 726
13. Wang, R.*, et al.*, *Nature* (1997) **388** (6641), 431
14. Wang, R.*, et al.*, *Advanced Materials* (1998) **10** (2), 135
15. Mills, A.*, et al.*, *Journal of Applied Electrochemistry* (2005) **35** (7-8), 641
16. Dunnill, C. W. H.*, et al.*, *Journal of Photochemistry and Photobiology A: Chemistry* (2009) **207** (2–3), 244
17. Page, K.*, et al.*, *Journal of Materials Chemistry* (2007) **17** (1), 95
18. Foster, H. A.*, et al.*, *Applied Microbiology and Biotechnology* (2011) **90** (6), 1847
19. Linsebigler, A. L.*, et al.*, *Chemical Reviews* (1995) **95** (3), 735
20. Piechocki, J. T., and Thoma, K., *Pharmaceutical Photostability and Stabilization Technology*. CRC Press: 2006
21. Gerward, L., and Olsen, J. S., High-pressure behaviour of titanium dioxide. In *European Powder Diffraction: Epdic Iv, Pts 1 and 2*, Cernik, R. J.*, et al.*, (eds.) (1996), Vol. 228, pp 383
22. Levchenko, A. A.*, et al.*, *Chemistry of Materials* (2006) **18** (26), 6324
23. Mills, A., and LeHunte, S., *Journal of Photochemistry and Photobiology a-Chemistry* (1997) **108** (1), 1
24. Diebold, U., *Surface Science Reports* (2003) **48** (5-8), 53
25. Zhang, H. Z., and Banfield, J. F., *J Phys Chem B* (2000) **104** (15), 3481
26. Brittain, H. G., *J Am Chem Soc* (1983) **105** (8), 2514
27. Joo, J. B.*, et al.*, *Energy & Environmental Science* (2012) **5** (4), 6321
28. Hurum, D. C.*, et al.*, *Journal of Physical Chemistry B* (2003) **107** (19), 4545
29. Chen, L. X.*, et al.*, *The Journal of Physical Chemistry B* (1997) **101** (50), 10688
30. Yeung, K. L.*, et al.*, *The Journal of Physical Chemistry B* (2002) **106** (18), 4608
31. Zhang, H.*, et al.*, *Physical Review B* (2008) **78** (21), 214106
32. Mott, N. F., and Allgaier, R. S., *physica status solidi (b)* (1967) **21** (1), 343
33. Yu, J. C.*, et al.*, *Chemistry of Materials* (2002) **14** (9), 3808
34. Hoffmann, M. R.*, et al.*, *Chemical Reviews* (1995) **95** (1), 69
35. Kafizas, A.*, et al.*, *The Journal of Physical Chemistry A* (2016) **120** (5), 715
36. Hoang, V. V.*, et al.*, *The European Physical Journal D* (2007) **44** (3), 515
37. Jiang, D. L.*, et al.*, *Environmental Science & Technology* (2007) **41** (1), 303
38. Kho, Y. K.*, et al.*, *Journal of Physical Chemistry C* (2010) **114** (6), 2821
39. Li, G. H.*, et al.*, *Journal of Catalysis* (2008) **253** (1), 105
40. Ohno, T.*, et al.*, *Applied Catalysis a-General* (2003) **244** (2), 383
41. Yan, M. C.*, et al.*, *Journal of Physical Chemistry B* (2005) **109** (18), 8673
42. Zachariah, A.*, et al.*, *Journal of Physical Chemistry C* (2008) **112** (30), 11345

43. Sclafani, A., and Herrmann, J. M., *The Journal of Physical Chemistry* (1996) **100** (32), 13655
44. Spurr, R. A., and Myers, H., *Analytical Chemistry* (1957) **29** (5), 760
45. Zhang, J.*, et al.*, *Angewandte Chemie International Edition* (2008) **47** (9), 1766
46. Asahi, R.*, et al.*, *Science* (2001) **293** (5528), 269
47. Nakamura, I.*, et al.*, *Journal of Molecular Catalysis a-Chemical* (2000) **161** (1-2), 205
48. Dunnill, C. W., and Parkin, I. P., *Dalton Transactions* (2011) **40** (8), 1635
49. Beranek, R., and Kisch, H., *Electrochemistry Communications* (2007) **9** (4), 761
50. Zhao, L.*, et al.*, *Applied Surface Science* (2008) **254** (15), 4620
51. Prabakar, K.*, et al.*, *Journal of Vacuum Science & Technology A* (2007) **25** (4), 1188
52. Di Valentin, C.*, et al.*, *Journal of Physical Chemistry B* (2005) **109** (23), 11414
53. Zongyan, Z., and Qingju, L., *Journal of Physics D: Applied Physics* (2008) **41** (8), 085417
54. Kowalska, E.*, et al.*, *Physical Chemistry Chemical Physics* (2010) **12** (10), 2344
55. Penn, R. L., and Banfield, J. F., *American Mineralogist* (1999) **84** (5-6), 871
56. Rothschild, A.*, et al.*, *Surface Science* (2003) **532–535**, 456
57. Ghosh, T. B.*, et al.*, *Journal of Applied Physics* (2003) **94** (7), 4577
58. Hirano, M.*, et al.*, *Journal of Solid State Chemistry* (2003) **170** (1), 39
59. Li, G.*, et al.*, *Journal of the American Chemical Society* (2005) **127** (24), 8659
60. Carp, O.*, et al.*, *Progress in Solid State Chemistry* (2004) **32** (1–2), 33
61. Kim, J.*, et al.*, *Journal of the European Ceramic Society* (2001) **21** (16), 2863
62. Batzill, M.*, et al.*, *Physical Review Letters* (2006) **96** (2), 026103
63. Hanaor, D. A. H., and Sorrell, C. C., *Journal of Materials Science* (2011) **46** (4), 855
64. Fang, C.-S., and Chen, Y.-W., *Materials Chemistry and Physics* (2003) **78** (3), 739
65. Park, H. K.*, et al.*, *Journal of the American Ceramic Society* (1997) **80** (3), 743
66. Yang, J., and Ferreira, J. M. F., *Materials Research Bulletin* (1998) **33** (3), 389
67. Sharma, S. D.*, et al.*, *Applied Catalysis A: General* (2006) **314** (1), 40
68. Smirnova, N.*, et al.*, *Journal of Sol-Gel Science and Technology* (2004) **32** (1), 357
69. Takahashi, Y., and Matsuoka, Y., *Journal of Materials Science* (1988) **23** (6), 2259
70. Teleki, A.*, et al.*, *Sensors and Actuators B: Chemical* (2006) **119** (2), 683
71. Wu, M.*, et al.*, *Chemistry of Materials* (2002) **14** (5), 1974
72. Wang, C.-C., and Ying, J. Y., *Chemistry of Materials* (1999) **11** (11), 3113
73. Cheng, H.*, et al.*, *Chemistry of Materials* (1995) **7** (4), 663
74. Ovenstone, J., and Yanagisawa, K., *Chemistry of Materials* (1999) **11** (10), 2770
75. Mills, A.*, et al.*, *Journal of Photochemistry and Photobiology A: Chemistry* (2002) **151** (1–3), 171
76. Goossens, A.*, et al.*, *Chemical Vapor Deposition* (1998) **4** (3), 109
77. Mardare, D.*, et al.*, *Applied Surface Science* (2000) **156** (1–4), 200
78. Meyer, S.*, et al.*, *Thin Solid Films* (2004) **450** (2), 276
79. Dvoranova, D.*, et al.*, *Applied Catalysis B-Environmental* (2002) **37** (2), 91
80. Serpone, N., *J Phys Chem B* (2006) **110** (48), 24287
81. Spanhel, L.*, et al.*, *J Am Chem Soc* (1987) **109** (22), 6632
82. Kamat, P. V., *Chemical Reviews* (1993) **93** (1), 267
83. Yu, J. C.*, et al.*, *Applied Catalysis B-Environmental* (2002) **36** (1), 31
84. Dunnill, C. W.*, et al.*, *Chemical Vapor Deposition* (2012) **18** (4-6), 89
85. Yang, J.*, et al.*, *Thin Solid Films* (2008) **516** (8), 1736
86. Okato, T.*, et al.*, *Physical Review B* (2005) **72** (11)
87. Diwald, O.*, et al.*, *J Phys Chem B* (2004) **108** (1), 52
88. Maeda, M., and Watanabe, T., *J Electrochem Soc* (2006) **153** (3), C186
89. Fujihara, K.*, et al.*, *Nanotechnology* (2007) **18** (36)
90. Smestad, G. P.*, et al.*, *Solar Energy Materials and Solar Cells* (2003) **76** (1), 85

91. Eranna, G., *et al.*, *Critical Reviews in Solid State and Materials Sciences* (2004) **29** (3-4), 111
92. Li, Z. X., *et al.*, *Chemical Society Reviews* (2012) **41** (7), 2590
93. Mano, J. F., *Advanced Engineering Materials* (2008) **10** (6), 515
94. Paital, S. R., and Dahotre, N. B., *Materials Science & Engineering R-Reports* (2009) **66** (1-3), 1
95. Enami, Y., *et al.*, *Nature Photonics* (2007) **1** (3), 180
96. Orignac, X., *et al.*, *Optical Materials* (1999) **12** (1), 1
97. Yi, G. H., *et al.*, *Journal of Applied Physics* (1988) **64** (5), 2717
98. Khan, S. U. M., *et al.*, *Science* (2002) **297** (5590), 2243
99. Ni, M., *et al.*, *Renewable & Sustainable Energy Reviews* (2007) **11** (3), 401
100. Campbell, W. M., *et al.*, *Coordination Chemistry Reviews* (2004) **248** (13-14), 1363
101. Liu, B., and Aydil, E. S., *Journal of the American Chemical Society* (2009) **131** (11), 3985
102. Chong, M. N., *et al.*, *Water Research* (2010) **44** (10), 2997
103. Herrmann, J. M., *Catalysis Today* (1999) **53** (1), 115
104. Pelaez, M., *et al.*, *Appl. Catal. B-Environ.* (2012) **125**, 331
105. Li, D., *et al.*, *Chemistry of Materials* (2005) **17** (10), 2596
106. Zhao, J., and Yang, X. D., *Building and Environment* (2003) **38** (5), 645
107. Parkin, I. P., and Palgrave, R. G., *Journal of Materials Chemistry* (2005) **15** (17), 1689
108. Paz, Y., *et al.*, *Journal of Materials Research* (1995) **10** (11), 2842
109. Watanabe, T., *et al.*, *Thin Solid Films* (1999) **351** (1-2), 260
110. Evans, P., and Sheel, D. W., *Surface & Coatings Technology* (2007) **201** (22-23), 9319
111. Kim, B., *et al.*, *Chemosphere* (2003) **52** (1), 277
112. Nishimoto, S., and Bhushan, B., *Rsc Advances* (2013) **3** (3), 671
113. Lai, Y. K., *et al.*, *Journal of Materials Chemistry* (2012) **22** (15), 7420
114. Kostecki, R., *et al.*, *Thin Solid Films* (2001) **396** (1-2), 36
115. Park, M., *et al.*, *Science* (1997) **276** (5317), 1401
116. H. Kawahara, H. H., Japanese patent 59141441 A (Nippon Sheet Glass). (1984)
117. Schmitt, R. H., *et al.*, *Journal of the American Chemical Society* (1960) **82** (20), 5292
118. Briggs, D., and Seah, M. P., *D. Briggs, & M. P. Seah,(Editors), John Wiley & Sons, Chichester 1983, xiv+ 533* (1983)
119. Tenderholt, A. L., *et al.*, *Inorganic Chemistry* (2008) **47** (14), 6382
120. Qayyum, M. F., *et al.*, *Journal of the American Chemical Society* (2013) **135** (46), 17417
121. Houas, A., *et al.*, *Applied Catalysis B: Environmental* (2001) **31** (2), 145
122. Du, L., *et al.*, *Water Science and Technology* (2011) **63** (7), 1539
123. Mills, A., and McGrady, M., *Journal of Photochemistry and Photobiology a-Chemistry* (2008) **193** (2-3), 228
124. Barr, T. L., *Journal of Vacuum Science & Technology A: Vacuum, Surfaces, and Films* (1991) **9** (3), 1793
125. Fadley, C. S., *Journal of Electron Spectroscopy and Related Phenomena* (2010) **178–179**, 2
126. Kahk, J. M., *et al.*, *Physical Review Letters* (2014) **112** (11), 117601
127. Hüfner, S., *et al.*, *Solid State Communications* (1975) **17** (4), 417
128. Tsui, H. C. L., *et al.*, *Journal of Physics D: Applied Physics* (2016) **49** (26), 265110
129. King, P. D. C., *et al.*, *Physical Review B* (2008) **78** (3), 033308
130. Wan, C., *et al.*, *Angewandte Chemie* (2014) **126** (25), 6525
131. Díaz, J., *et al.*, *Physical Review B* (1996) **54** (11), 8064
132. Jackson, S. T., and Nuzzo, R. G., *Applied Surface Science* (1995) **90** (2), 195

133. Lascovich, J. C., *et al.*, *Applied Surface Science* (1991) **47** (1), 17
134. Cong, Y., *et al.*, *The Journal of Physical Chemistry C* (2007) **111** (28), 10618
135. Etacheri, V., *et al.*, *Advanced Functional Materials* (2011) **21** (19), 3744
136. Takahashi, I., *et al.*, *Chemical Physics Letters* (2008) **454** (4–6), 314
137. Glover, E. N. K., *et al.*, *Journal of Materials Chemistry A* (2016) **4** (18), 6946
138. Åsbrink, L., *et al.*, *Chemical Physics Letters* (1977) **52** (1), 69
139. Godinho, K. G., *et al.*, *Journal of Materials Chemistry* (2008) **18** (24), 2798
140. Knight, J. B., *et al.*, *Phys Rev Lett* (1993) **70** (24), 3728
141. Breeson, A. C., *et al.*, *Physical Chemistry Chemical Physics* (2016) **18** (35), 24722
142. Tobaldi, D. M., *et al.*, *Materials Letters* (2014) **122**, 345
143. Ding, Z., *et al.*, *Journal of Physical Chemistry B* (2000) **104** (19), 4815
144. Li, G., *et al.*, *Journal of Molecular Catalysis A: Chemical* (2007) **275** (1–2), 30
145. Wu, C., *et al.*, *Catalysis Today* (2004) **93–95**, 863
146. Powell, M. J., *et al.*, *Journal of Photochemistry and Photobiology a-Chemistry* (2014) **281**, 27
147. Wang, W.-L., *et al.*, *Thin Solid Films* (2010) **518** (11), 2967
148. Yu, Z. Q., *et al.*, *Nanotechnology* (2007) **18** (11), 115601
149. Lim, S.-W., *et al.*, *Solid State Communications* (2003) **125** (5), 231
150. Herman, G. S., and Gao, Y., *Thin Solid Films* (2001) **397** (1-2), 157
151. Ito, A., *et al.*, *Thin Solid Films* (2014) **551**, 37
152. Murakami, M., *et al.*, *Applied Physics Letters* (2001) **78** (18), 2664
153. Ong, C. K., and Wang, S. J., *Applied Surface Science* (2001) **185** (1–2), 47
154. Sbaï, N., *et al.*, *Surf Sci* (2007) **601** (23), 5649
155. Kitazawa, S.-i., *et al.*, *Thin Solid Films* (2006) **515** (4), 1901
156. Roch, T., *et al.*, *Journal of Crystal Growth* (2012) **338** (1), 118
157. Yamamoto, S., *et al.*, *Thin Solid Films* (2001) **401** (1-2), 88
158. Ruzybayev, I., and Shah, S. I., *Surface and Coatings Technology* (2014) **241**, 148
159. Lindgren, T., *et al.*, *The Journal of Physical Chemistry B* (2003) **107** (24), 5709
160. Kazunori, F., and Isao, Y., *Japanese Journal of Applied Physics* (1996) **35** (11R), 5790
161. Cong, Y., *et al.*, *Journal of Physical Chemistry C* (2007) **111** (19), 6976
162. Livraghi, S., *et al.*, *Journal of the American Chemical Society* (2006) **128** (49), 15666
163. Sakthivel, S., *et al.*, *Journal of Physical Chemistry B* (2004) **108** (50), 19384
164. Sathish, M., *et al.*, *Chemistry of Materials* (2005) **17** (25), 6349
165. Khan, M., *et al.*, *Journal of Physics and Chemistry of Solids* (2017) **110**, 241
166. Ren, D. H., *et al.*, *Journal of Solid State Chemistry* (2016) **238**, 83
167. Kim, D. S., and Kwak, S.-Y., *Applied Catalysis A: General* (2007) **323**, 110
168. Lebedev, V. A., *et al.*, *Appl. Catal. B-Environ.* (2016) **195**, 39
169. Huang, J., *et al.*, *Research on Chemical Intermediates* (2012) **38** (2), 487
170. Wang, X.-j., *et al.*, *Journal of Hazardous Materials* (2015) **292**, 126
171. Wang, Q., *et al.*, *Journal of Hazardous Materials* (2013) **246–247**, 135
172. Zou, J., *et al.*, *Journal of Alloys and Compounds* (2010) **497** (1–2), 420
173. Scarel, G., *et al.*, *Journal of Applied Physics* (2002) **91** (3), 1118
174. Sakata, T., *et al.*, *Chemical Physics Letters* (1982) **88** (1), 50
175. Oosawa, Y., and Gratzel, M., *Journal of the Chemical Society, Chemical Communications* (1984) (24), 1629
176. Ohtani, B., *et al.*, *Journal of Photochemistry and Photobiology A: Chemistry* (1992) **64** (2), 223
177. Bel Hadj, F., *et al.*, *Journal of Non-Crystalline Solids* (1986) **82** (1), 417
178. Scanlon, D. O., *et al.*, *Nature materials* (2013) **12** (9), 798
179. Imanishi, A., *et al.*, *The Journal of Physical Chemistry C* (2007) **111** (5), 2128
180. Gutmann, S., *et al.*, *Journal of Applied Physics* (2010) **107** (10), 103705

181. Hassanien, A. S., and Akl, A. A., *Journal of Alloys and Compounds* (2015) **648**, 280
182. Takeuchi, M.*, et al.*, *Journal of Physical Chemistry B* (2005) **109** (32), 15422
183. Attfield, M. P.*, et al.*, *Catalysis Letters* (2000) **70** (3), 155
184. Banerjee, S.*, et al.*, *Appl. Catal. B-Environ.* (2015) **176**, 396
185. Mills, A.*, et al.*, *Journal of Physical Chemistry B* (2006) **110** (37), 18324
186. Randorn, C.*, et al.*, *International Journal of Photoenergy* (2008) **2008**
187. Omurzak, E.*, et al.*, *Journal of nanoscience and nanotechnology* (2009) **9** (11), 6372
188. Gao, Y.*, et al.*, *Langmuir* (2004) **20** (8), 3188
189. Sabbah, H., *Materials Express* (2013) **3** (2), 171